Investigating Lyman continuum escape fractions of high redshift galaxies during the era of reionization

Ivan Kostyuk

München 2023

Investigating Lyman continuum escape fractions of high redshift galaxies during the era of reionization

Ivan Kostyuk

Dissertation
an der Physik
der Ludwig–Maximilians–Universität
München

vorgelegt von
Ivan Kostyuk
aus Kyiv, Ukraine

München, den 31.03.2023

Erstgutachter: PD Dr. Torsten Enßlin
Zweitgutachter: Dr. Klaus Dolag
Tag der mündlichen Prüfung: 25.05.2023

Zusammenfassung/Abstract

Während der ersten Milliarde Jahre des Bestehens unseres Universums durchlief das intergalaktische Medium (IGM) den bedeutenden Phasenübergang der Reionisation. Dieses transformative Ereignis wurde hauptsächlich durch die Emission von Lyman-Kontinuum (LyC) Photonen ausgelöst, die von den ersten entstandenen Galaxien stammen. Die Reionisation des IGM markierte im Wesentlichen einen entscheidenden Meilenstein und führte zum finalen großen Phasenübergang in der Geschichte des Universums.

Um ein umfassendes Verständnis des Reionisationsprozesses zu erlangen, ist es wichtig, die Propagation der LyC-Photonen zu verstehen, während sie aus ihren stellaren Quellen entweichen und die äußeren Grenzen des galaktischen Halos durchdringen. Obwohl neue Observatorien wie ALMA und JWST unvergleichliche Einblicke in stark rotverschobene Galaxien und und die Folgen ihres LyC-Austritt bieten, ist es wichtig zu beachten, dass eine direkte Beobachtung von LyC-Flucht bei diesen hohen Rotverschiebungen nicht möglich ist. Aus diesem Grund ist die theoretische Modellierung notwendig, um zuverlässige quantitative Vorhersagen bezüglich LyC-Flucht zu machen, die dann anhand von Beobachtungen getestet und verifiziert werden können.

Die theoretische Modellierung von LyC-Flucht erfordert die Integration eines breiten Spektrums an Skalen, die von den stellaren Quellen bis zum IGM reichen. In dieser Dissertation präsentiere ich zwei unterschiedliche Ansätze zur Modellierung von LyC-Flucht, die jeweils dazu konzipiert sind, diesen großen dynamischen Bereich zu berücksichtigen. Darüber hinaus stelle ich einen Super-Resolution-Algorithmus für kosmologische Simulationen vor, der die Modellierung dieses breiten Spektrums an Skalen auf höchst effiziente Weise erleichtert.

Der erste Ansatz, den ich präsentiere, umfasst eine simulationsbasierte Methode zur Modellierung von LyC-Flucht. Konkret bearbeite ich Galaxien aus der TNG50 Kosmologiesimulation mithilfe des Multi-Frequency-Monte-Carlo-Strahlungstransfercodes CRASH, um ihren Ionisationszustand zu modellieren und den Anteil der emittierten Photonen zu schätzen, der in das IGM entweicht. Durch diesen Ansatz analysiere ich die Korrelation zwischen LyC-Flucht und einer Reihe galaktischer Eigenschaften. Zudem zeige ich die nicht-linearen Effekte der Subgrid-Modellierung auf den Fluchtanteil auf. Abschließend schätze ich die globale Menge an verfügbaren Photonen, die das Universum reionisieren können, basierend auf den Vorhersagen, die mit dieser Methode erzielt wurden.

Der zweite Ansatz, den ich in dieser Arbeit diskutiere, beinhaltet eine semi-analytische Methode zur Modellierung der Lyman-Kontinuum-Photonen-Flucht. Dabei wird die Galaxie

als dünne Scheibe modelliert, in der ionisierende Photonen von dem Gas und Staub absorbiert werden, das die galaktische Scheibe umgibt. Durch diesen Ansatz zeige ich, dass es zwei unterschiedliche Arten von Lyman-Kontinuum-Photonen-Flucht gibt: eine, bei der die Sternentstehung in einem breiten Bereich stattfindet und die Lyman-Kontinuum-Photonen aus den weniger dichten äußeren Regionen der Galaxie entweichen, und eine andere, bei der sowohl die Sternentstehung als auch die Lyman-Kontinuum-Photonen-Flucht stark auf die zentrale Region der Galaxie konzentriert sind.

Als drittes präsentiere ich den Einsatz von Neural-Netzwerk-Methoden zur Super-Auflösung kosmologischer Simulationen. Um dies zu erreichen, verwende ich Konvoluzionäre-Neuronale-Netzwerke zur Verarbeitung von auf einem regulären Gitter verteilten Dunkle-Materie-Simulationen. Durch diesen Ansatz zeige ich die Bedeutung unterschiedlicher Netzwerkverlustansätze und deren Auswirkungen auf die Ergebnisse. Ich führe sowohl qualitative als auch quantitative Analysen der Ergebnisse durch und betrachte deren statistische Eigenschaften, um die Effektivität dieser Methode besser zu verstehen.

During the initial billion years of our Universe's existence, the Intergalactic Medium (IGM) underwent the significant phase transition of reionization. This transformative event was primarily triggered by the emission of Lyman Continuum (LyC) photons, which originated from the first galaxies that formed. In essence, the reionization of the IGM marked a crucial milestone, culminating in the final major phase transition that occurred in the Universe's history.

To gain a comprehensive understanding of the reionization process, it is essential to comprehend the journey of LyC photons as they escape from their stellar sources and penetrate the outer boundaries of the galactic halo. While new observatories like ALMA and JWST offer unparalleled insights into high-redshift galaxies and their LyC leakage, it is important to note that direct observation of LyC escape at these high redshifts is not feasible. As a result, theoretical modeling is necessary to make reliable quantitative predictions concerning LyC leakage, which can then be tested and verified using observations.

The theoretical modeling of LyC escape necessitates the integration of an extensive range of scales, spanning from the stellar sources to the IGM. In this thesis, I present two distinct approaches for modeling LyC escape, each of which is designed to account for this vast dynamic range. Moreover, I present a super-resolution algorithm for cosmological simulations, which serves to facilitate the modeling of this broad range of scales in a highly efficient manner.

The first approach that I present involves a simulation-based method for modeling LyC escape. Specifically, I post-process galaxies from the TNG50 large-scale cosmological simulation using the multi-frequency Monte Carlo radiative transfer code CRASH, to model their ionization state and estimate the fraction of emitted photons which escapes into the IGM. Through this approach, I analyze the correlation between LyC escape and a range of galactic properties. Additionally, I demonstrate the non-linear effects of subgrid modeling on the escape fraction. Finally, I estimate the global amount of photons which are available to reionize the Universe, based on the predictions obtained from this method.

The second procedure I discuss in this thesis involves a semi-analytic method for modeling LyC escape. This method involves modeling the galaxy as a thin slab, where ionizing photons are absorbed by the gas and dust enveloping the galactic disc. Through this approach, I demonstrate that there are two distinct modes of LyC escape: one in which star formation occurs over a broad area and LyC photons escape from the less dense outer regions of the galaxy, and another in which both star formation and LyC leakage are highly concentrated in the central region of the galaxy.

Thirdly, I present the use of neural-network methods to super-resolve cosmological simulations. To achieve this, I employ convolutional neural networks to process gridded dark-matter-only simulations. Through this approach, I demonstrate the significance of different network loss approaches and their impact on the final results. I perform both qualitative and quantitative analyses of the outcomes, looking at the statistical properties to better understand the effectiveness of this method.

Contents

List of Figures

List of Tables

"In the beginning the Universe was created. This has made a lot of people very angry and been widely regarded as a bad move." Douglas Adams

Chapter 1

Introduction

1.1 Motivation

The field of cosmology strives to gain insight into the unfolding of our Universe. Starting from a hot, nearly uniform state, minuscule density fluctuations gradually grew into a vast distribution of highly overdense galactic filaments and clusters. Over the course of approximately 13.8 billion years, the matter in the Universe underwent multiple transitions, beginning with the high-energy inflaton field, followed by particle formation and subsequent evolution in a hot plasma state. Roughly 400,000 years after the big bang, the matter recombined into a neutral state. However, overdensities in the Universe continued to grow due to gravitational attraction, eventually leading to the formation of the very first stars and galaxies. These stars emitted photons, with the most energetic among them able to ionize hydrogen gas in and around the galaxies, marking the commencement of the final phase transition in the Universe, reionization.

During this phase transition, ionized bubbles continued to expand around galaxies, eventually merging with the bubbles surrounding neighboring galaxies until approximately 1 billion years after the big bang, when the entire intergalactic medium became fully ionized. This event had a profound impact on the future evolution of galaxies, as the process of reionization heated the intergalactic medium and hindered the cooling process necessary for smaller galaxies to obtain gas and form new stars, leading to their quenching (e.g. [171, 20, 20]). Simultaneously, the intergalactic medium underwent a significant shift towards transparency to hydrogen lines, resulting in the emergence of cosmological probes such as the Lyman-α line as a viable means of gathering information about the structures present in the Universe.

To further the understanding of the process of reionization is one of the main goals of current cosmological research. One key question that needs to be answered for this purpose is: What characterized the main sources of reionization?

Originally, two sources of ionization were identified to be potential drivers of reionization, namely active galactic nuclei (AGN) and early galaxies. However, although AGN have

a hard ionizing spectrum, their density was deemed to be insufficient (e.g. [44, 36, 154]) to contribute a majority of the ionizing photons required to reionize the IGM. Therefore, it was concluded that early galaxies must be the sources of most ionizing radiation.

However, this leads to a different question: what were the specific characteristics of the galaxies that facilitated reionization? In order to answer this, we must gain a better understanding of the star-formation efficiency and initial mass function (IMF) of different galaxies, which played a crucial role in determining the production of ionizing radiation (also known as Lyman Continuum or LyC radiation). Additionally, we must determine how much of this radiation was actually able to escape into the intergalactic medium.

The LyC production and escape are coupled over a large range of scales. On the one hand star-formation efficiency affects LyC escape as new young stars can ionize channels in the galactic gas through which radiation can escape. Additionally, star-formation efficiency and the IMF determines the frequency and strength of supernovae, the feedback of which further drives LyC escape (e.g. [219, 201]). On the other hand, as mentioned earlier, the escaping LyC photons heat the IGM thus potentially inhibiting future star formation.

Therefore, a comprehensive understanding of reionization depends heavily on the precise modelling of physical processes across a vast range of scales. However, all numerical models of reionization must make a trade-off between accurately modelling the large-scale reionization and sacrificing accuracy on smaller scales, or vice versa. As a result, both the qualitative and quantitative behavior of LyC photon production and escape remain highly uncertain, and often vary considerably between different studies, with differences spanning several orders of magnitude.

On the observational front, the development of new telescopes, particularly the JWST, has enabled us to peer deep into the high redshift Universe during the era of reionization. Nevertheless, even these state-of-the-art tools will not be able to capture the faintest high redshift galaxies, which may in fact produce a significant amount of LyC radiation and therefore drive the reionization process (e.g. [212, 7]).

The primary objective of the first two projects outlined in this work is to focus on a specific factor in the reionization process, the galactic LyC escape fraction $f_{\rm esc}$. The first project tackles this issue through simulations, with a particular emphasis on radiation-transfer post-processing. On the other hand, the second project builds upon an analytical approach to examine the production and escape of LyC radiation. This method is then applied to study simulations in post-processing.

Lastly, the third project presented in this work aims to expand the dynamic range of future numerical studies of reionization. The concept behind this approach is to utilize a super-resolution algorithm, which generates small-scale structures into a coarser sampled and thus less computationally demanding simulation.

1.2 Structure of this work

This thesis commences with two introductory chapters that establish the broader context of our work within the realm of astrophysical and cosmological research.

Chapter 2 introduces the reader to the current model of our Universe on large scales. We discuss the ideas that underlie the process under which initial minuscule quantum fluctuation in the first moments of the Universe existence evolved into the cosmic web of galaxies and voids that we observe today. We also introduce the topic of cosmological reionization the last cosmological phase transition.

Chapter 3 introduces the topic of Lyman Continuum (LyC) production and escape into the intergalactic medium (IGM) which is the main research subject of this work. This process connects small scale astrophysical processes within galaxies to the large scale study of reionization. We present how LyC escape is modelled at various scales of resolution as well as how it is studied with observations.

Chapter 4 presents our work on LyC escape in TNG50 galaxies using the Monte-Carlo radiation-transfer (MCRT) code CRASH. Therein, we investigate a sample of 10,000 halos distributed over the redshifts 6, 8 and 10. We discuss the distribution of the LyC escape fraction of these galaxies. We further investigate the various physical characteristics of the halo that are correlated with LyC escape. Finally, we discuss how sub-grid models of LyC escape affect the global escape fraction and the resulting LyC photon density in the IGM.

Chapter 5 approaches the problem of LyC escape from a different perspective. Here, we post process TNG50 galaxies with a physically motivated semi-analytic model. In this model galaxies are assumed to be thin slates with their star forming region emitting LyC photons. The escape fraction of these photons is regulated by the absorption in the gas and dust surrounding that disc.

Chapter 6 focuses on the development of a super-resolution algorithm for cosmological simulations which could help bridge the large dynamical range involved in the study of reionization. We approach this topic using machine learning tools in particular artificial neural networks (ANNs). We first introduce the different types of networks used in our study before discussing the qualitative and quantitative properties of the super-resolved simulation boxes obtained using these methods.

Finally, in chapter 7 we summarize our three projects and their main results. We also discuss the next steps that are needed for the further development of our research.

Chapter 2

Cosmological context

Before diving into the details of the research presented in this work it is necessary to establish the broader picture of the cosmological model that forms the framework from which structures in the Universe emerge.

The goal of this chapter is to introduce the reader to the ΛCDM cosmological model which is to this day most successful at describing the current state of the Universe. Based on that framework we discuss how the first galaxies emerged and how the hydrogen that became neutral as the Universe cooled down adiabatically was reionized through the radiation of the first astrophysical sources of ionizing radiation.

2.1 The ΛCDM cosmological model

Our current model of the Universe stands on three axioms

1. **Isotropy**: The cosmological structure an observer perceives is independent from the direction they are looking at.

2. **Homogeneity**: The first axiom is true for all points in the Universe.

3. **General relativity**: The evolution of the Universe is governed by the Einstein equations [46].

Note that the first two axioms are valid in a statistical sense and over large scales, i.e. locally in our galaxy structures do not appear either isotropic nor homogeneous. However, if we look at large scales the filamentary distributions of matter in the Universe do not depend on the direction we are looking at. While the first and the third axioms can be tested directly, the second axiom is based on the Coperican principle which states that our planet does not occupy a special place in the Universe.

In order to describe the evolution of the Universe, the first two axioms need to be

inserted into the Einstein equations resulting in the Friedmann equations [58]

$$\left(\frac{\dot{a}}{a}\right)^2 = \frac{8\pi G}{3}\rho - \frac{Kc^2}{a^2} + \frac{\Lambda c^2}{3} \tag{2.1}$$

$$\frac{\ddot{a}}{a} = -\frac{4\pi G}{3}\left(\rho + \frac{3P}{c^2}\right) + \frac{\Lambda c^2}{3}. \tag{2.2}$$

Hereby G is the gravitational constant, c is the speed of light, K is the spatial curvature, ρ is the average mass density in the Universe, P the pressure and Λ is the cosmological constant. The first Friedmann equation describes at what rate the Universe expands this rate is commonly called the Hubble constant $H := \dot{a}/a$ after Edwin Hubble who first attempted to measure it [91]. The second equation describes the de- or acceleration of the the rate.

By introducing the critical density which corresponds to the density of a spatially flat Universe given by

$$\rho_{\mathrm{cr}} := \frac{3H^2}{8\pi G}, \tag{2.3}$$

we can introduce the dimensionless density parameters

$$\Omega_{\mathrm{m}}(t) := \frac{\rho_m(t)}{\rho_{\mathrm{cr}}(t)} \tag{2.4}$$

$$\Omega_{\mathrm{r}}(t) := \frac{\rho_r(t)}{\rho_{\mathrm{cr}}(t)} \tag{2.5}$$

$$\Omega_{\Lambda}(t) := \frac{\Lambda c^2}{3H^2(t)} \tag{2.6}$$

$$\Omega_K(t) := -\frac{Kc^2}{a^2(t)H^2(t)}. \tag{2.7}$$

These parameters always sum up to unity hence the fourth parameter can be determined from knowing the other three. With this the first Friedmann equation simplifies to

$$H^2(a) = H_0^2[\Omega_{m_0}a^{-3} + \Omega_{r_0}a^{-4} + \Omega_{\Lambda_0} + \Omega_{K_0}a^{-2}], \tag{2.8}$$

whereby the index 0 indicates the values of the parameters at the present moment. Measurements of the curvature parameter K_0 point towards a spatially flat Universe [6].

These equations imply that the Universe originated from an initial singularity. According to the current model it first expanded at a fast exponential rate for the first $\sim 10^{-32}$s [78]. According to the slow roll inflation model in the Universe's first moments of existence the fundamental forces were unified and the energy density was given by a scalar quantum field. Due to the uncertainty principle this field had slight variations in its energy density. Normally, energy variations in a quantum field spring into existence as pairs of particles and antiparticles and annihilate on very short timescales. However, during the process of inflation these quantum mechanical fluctuations in the energy density were pulled apart at such a fast rate that they ceased to be in causal contact with the counterpart and were

hence 'frozen' into the energy density distribution. These fluctuations then became the seeds for the structures we see today in the Universe.

After inflation the Universe continued to expand adiabatically. As matter almost completely outbalanced antimatter most of the matter content annihilated into photons such that the ratio of photon to matter particles is on the order of 10^{10}. This means that early on the expansion of the Universe was dominated by radiation. During this radiation dominated era structures which came into causal contact were washed out by free streaming photons. Also during this time the fundamental forces decoupled and particles stared forming. The first step was Baryongenesis in which quark-gluon plasma condensed into the first baryons [178] and later some baryons, approximately 25% fused into Helium nuclei with a very small fraction fusing into Lithium nuclei [4]. However, due to the adiabatic cooling, this fusion process was interrupted such that all heavier elements were not created up to the time when the first stars ignited.

As space expanded the energy density of photons and any other ultra relativistic matter declined more rapidly than non-relativistic matter as in addition the the decrease of number density with increasing volume, the wavelength of photons increased resulting in an additional factor of a in eq. 2.8. As a result, eventually the matter energy density became larger than the radiation density and the Universe entered its matter dominated era.

A useful to trace the history of the Universe is the redshift z which states by how much a photon emitted at a certain point in time would be streched with the expansion of the Universe before arriving here. It is given by

$$z = \frac{1}{a} - 1. \tag{2.9}$$

Given that the Hubble function is strictly monotonous in time, the redshift can be used as a time coordinate when tracing events in the Universe. E.g. the point at which the Universe transitioned from matter to radiation domination was at $z \approx 3600$.

During the matter radiation phase, structures in the Universe which were in causal contact were able to grow again as over densities created gravitational wells into which matter could fall. Radiation during that time was tightly coupled to baryonic matter though frequent Thomson scattering events. This caused an additional pressure force inhibiting the growth of baryonic over densities and resulted in the creation of baryon-acoustic oscillations [156, 196].

During the earlier part of the matter dominated era, electrons and protons could not combine to form atoms as these were immediately ionized by photons. Eventually however, the Universe cooled far enough for electrons an protons to form hydrogen atoms. This happened at a redshift of $z \approx 1100$. At this point, the photon temperature was around 3000K, far below what is usually required for hydrogen ionization. However, due to there being 10^{10} photons per hydrogen atom the high energy tail of the Boltzmann distribution resulted in this additional delay.

As hydrogen formed, photons and baryons decoupled and photons were able to stream freely forming the cosmic microwave background (CMB). It was first predicted by Alpher

and Herman in 1948 [4] and accidentally detected by Penzias and Wilson in 1965 [157]. The CMB is of crucial importance for our cosmological understating as the structure of its anisotropies strongly dependent on the values of the parameters in the Universe. These anisotropies were first detected by the COBE satellite [186]. Later more accurate measurements were conducted by, among other experiments, WMAP [109] and the Planck satellites [6]. With the later providing the most accurate measurements of the cosmological parameters to date.

These measurements also found that the size of the baryon-acoustic oscillations was to small for all matter to interact with photons. This and several other experiments e.g. galaxy rotation curve measurements suggest that about 84% of matter in the Universe does not interact noticeably in any other way than gravitationally. It was coined the cold dark matter (CDM) first proposed in [221]. Furthermore it was found that the value of $\Omega_{m,0}$ is approximately 0.3 and given that measurements of the angular size of baryon acoustic oscillations suggest a specially flat Universe, leads to the conclusion of a non-zero dark energy component of the Universe $\Omega_{\Lambda,0} \approx 0.7$. This means that today the Universe is transitioning from a matter dominated phase to a dark energy dominated phase leading to an exponentially accelerating expansion. This exponential expansion was first measured in 1998 [173]. These measurements together confirmed the ΛCDM cosmological model which summarizes our current understanding of the Universe.

However, one problem that remains is that the measurements of the expansion rate of the Universe derived from CMB observations do not agree with the supernovae measurements performed in our local environment. This so called Hubble tension puts into question the validity of ΛCDM cosmology and calls for a better understanding of the cosmological evolution between CMB decoupling and today.

2.2 Growth of structures and halo formation

After the CMB decoupled the Universe entered the so called dark ages. During that time no photons were emitted. However, gravitational wells continued to attract matter and to grow. Initially the density contrast defined as

$$\delta := \frac{\rho}{\bar{\rho}} - 1, \tag{2.10}$$

with ρ being the matter density and $\bar{\rho}$ the average density in the Universe, grows linearly as long as $\delta \ll 1$. During the time of linear density perturbations the probability of finding a given density contrast averaged over a sphere with radius R is given by a Gaussian random field

$$p(\bar{\delta}, a) = \frac{1}{\sqrt{2\pi\sigma_R^2(a)}} \exp\left(-\frac{\bar{\delta}^2}{2\sigma_R^2(a)}\right), \tag{2.11}$$

where $\sigma_R(a)$ is the expansion factor dependent variance of the density. It can be separated into

$$\sigma_R(a) = \sigma_{R,0} D_+(a). \tag{2.12}$$

Here $\sigma_{R,0}$ is the variance in density fluctuations today and $D_+(a)$ the linear growth factor. The variance can be obtained from the primodial power-spectrum evolved through the early stages of the Universe up to CMB decoupling using the Boltzmann equations [47]. It is connected to the power spectrum through

$$\sigma_R^2 = 4\pi \int \frac{k^2 \mathrm{d}k}{(2\pi)^3} P(k) \tilde{W}_R(k)^2. \tag{2.13}$$

Here $P(k)$ is the power spectrum and $\tilde{W}_R(k)$ is the Fourier transformed window function corresponding to the radius R. The second part of 2.12 $D_+(a)$ is the linear growth factor which can be derived from linear perturbation theory and is proportional to a during the matter dominated era.

Over densities grow against an expanding space time. Hence, we would expect that a future halo would start out as a small overdensity which at first grows with the expansion of space-time. Eventually it reaches a critical radius at which point the gravitational pull is stronger than the expansion of space time and the overdensity collapses. Assuming such a spherical collapse model one can derive for a matter dominated Universe that the critical overdensity at which an overdensity should be collapsed is $\delta_c \approx 1.68$ [77]. However, matter does not collapse into a singularity, rather the directional in fall of particles is transformed into random thermal motion of the particles with the gravitational and kinetic energy being distributed according to the virial theorem

$$E_{\mathrm{kin}} = -\frac{1}{2} E_{\mathrm{pot}}, \tag{2.14}$$

with E_{kin} and E_{pot} being the total kinetic and potential energies of all matter contained in the sphere of the overdensity. This process is called violent relaxation [122]. These virialized halos then become the host of galaxies and galaxy clusters. From the gravitational potential energy contained in the sphere before collapse one can derive the resulting overdensity after collapse which is $\delta_{\mathrm{vir}} \approx 178$. This value which can be crudely approximated to 200 can be used to define the extend of the halo as will be later done in this work.

Given the model of spherical collapse as well as the initial overdensity distribution one can derive the number density of halos with different masses. These calculations were performed in [163] resulting in the Press-Schechter Mass function

$$n(M,a) = \sqrt{\frac{2}{\pi}} \frac{\bar{\rho}}{M} \frac{\delta_c}{\sigma_R D_+(a)} \frac{\mathrm{d}\ln\sigma_R}{\mathrm{d}M} \exp\left(-\frac{\delta_c^2}{2\sigma_R^2 D_+^2(a)}\right) \frac{\mathrm{d}M}{M}, \tag{2.15}$$

where M is the mass of the halo. The derivative $\mathrm{d}\ln\sigma_R/\mathrm{d}M$ can be calculated from the linear powerspectrum taking into account that a radius can be associated with a mass given the average density through

$$R(M) = \left(\frac{3M}{4\pi\bar{\rho}}\right)^{\frac{1}{3}}. \tag{2.16}$$

The The Press-Schechter model agrees well with the statistics obtained by cosmological simulations (e.g. [192]), especially once it is expanded to include elliptical collapse and halo merger statistics [182]. The main discrepancy between simulations and analytic models today lies in the Press-Schechter model overpredict the abundance of low-mass halos while underpredicting the amount of high-mass halos.

2.3 Formation of the first stars and galaxies

During the formation of the first halos both baryonic and dark matter collapsed to form gravitationally bound objects. However, the collapse caused the baryonic matter to heat up as gravitational potential energy transformed into kinetic energy in accordance with the virial theorem. Hence, as the halo formed baryonic matter heated up. This made further collapse of matter and the formation of first stars difficult as the temperature of the gas generated pressure forces opposing the gravitational pull. The critical length below which matter is stable against gravitational collapse is given by the Jeans length [98]

$$\lambda_J = \left(\frac{15 k_\mathrm{B} T}{4\pi G m_P \mu \rho} \right)^{\frac{1}{2}}. \tag{2.17}$$

Here k_B is the Boltzmann's constant, T the temperature of the gas, m_P the proton mass, μ the mean molecular mass and ρ the density of the gas enclosed in the sphere.

Therefore, in order to form smaller structures that were able to collapse into stars the gas needed to cool first. Galactic cooling today is facilitated through the presence of metals the line emissions of which are efficient channels for dissipating energy. However, when the frist galaxies formed the gas was not metal enriched yet thus cooling had to be driven by gas only. At higher temperatures ($T \gtrsim 10^4$K) energy could be transported away through collisional excitation of atoms, i.e. highly energetic hydrogen atoms collided with free electrons and the collisional energy excited the atoms into higher energy states and got shortly after emitted as radiation. Once the gas has cooled to lower temperatures but still above 10^4K it can further dissipate energy through Lyman α line emissions and finally for smaller halos with virial temperatures below 10^4K through molecular gas once its temperature is low enough to form H_2 molecules. However, in the early Universe further cooling and fragmentation is not possible due to a lack of metals. These would normally facilitate the dispersion of energy through the their line transitions.

Hence the first molecular gas clouds (GMC) that form in early proto-galaxies do not fragment into smaller, cooler clouds as they do at later times. However, once the gas has collapsed into a proto-planetary disc, simulations show that these discs tend to fragment and form multiple stars in one system. As a result, the first stars formed through the collapse of these clouds coined Population III stars tend to be massive and hence very short lived [38].

Population III stars with masses on the order of 10s of $M_\odot$ in multi-star system explode into highly energetic Pair Instability Supernovae (PISN) a few million years after their formation. In that process they on the one hand shock heat and push out the gas around

them quenching the formation of additional stars. On the other hand they enrich the gas with the metals produced during the nuclear fusion processes in their core as during PISN events roughly half of the stars mass gets converted into metals. This means that future gas clouds can cool down and fragment into smaller structures allowing them to form less heavy population II stars. The masses of the stars formed hereby follows an initial mass function (IMF) of which several models are available [179, 111, 25]. Despite uncertainties in the exact form of the IMF, all of these models predict that only a very small fraction of the collapsing gas gets converted into very massive O and B type stars. These few stars are however of crucial importance for the further evolution of the galaxy as these were the only stars that produced ionizing radiation. The ionizing photons first of all heated the surrounding interstellar medium if it was not dense enough to self shield against the radiation. This caused the ISM two contain two states of gas: cold self shielding gas containing most of the gas mass and responsible for the production of new stars and hot gas filling out most of the volume but containing a smaller fraction of the gas mass.

2.4 Reionization

For the history of the Universe the production of ionizing photons by massive stars plays a crucial role as some of this radiation is able to escape into the IGM and ionize the surrounding gas thus commencing the era of reionization [1]. This process began at $z \approx 30$ [121] and was completed by $z \approx 6$ with the IGM being completely ionized and was the last phase transition of the Universe.

Although we know that the process of reionization had to occur at high redshift the details of its history are far from understood. One open question is "What were the main drivers of reionization?". I.e. were a majority of the photons ionizing the IGM escaping from a few large or many smaller mass galaxies? Or was there perhaps a transition between the two? These details greatly affect the topology of reionization, which in turn affects how galaxies formed and evolved during this time. To gain a better insight, we need to understand the history of star formation in distant galaxies, as well as how much of the ionizing radiation could escape into the IGM rather than being trapped in the ISM. The latter process is summarized by the ionizing photon escape fraction $f_{\rm esc}$ the investigation of which is the main goal of this work and we will discuss it in far more detail in the following chapters.

Independently of what the source is, ionizing radiation forms an ionized bubble around the origin of radiation. This bubble can be further deformed through density variation in the IGM as more dense environments, e.g. along the directions of density filaments, have a higher recombination rate making them more difficult to ionize. In the expanding Universe

[1] An additional driver of reionization are quasars, i.e. high luminosity black hole accretion discs in the center of galaxies. Due to their relatively low abundance however, they only contribute a minor fraction of the photons required to ionize the IGM.

the growth of these bubbles can be approximated by [135]

$$4\pi r_I^2 n_H \left(\frac{\mathrm{d}r_I}{\mathrm{d}t} - H r_I\right) = \dot{N}_{\mathrm{ion}} - \frac{4}{3}\pi r_I^3 n_H^2 C(z)\alpha_B(T). \tag{2.18}$$

Here, r_I is the physical radius of the ionized bubble, n_H the hydrogen density, H the Hubble function, $\dot{N}_{\mathrm{ion}}$ the emission rate of ionizing photons from the galaxy, $C(z)$ the clumping factor and $\alpha_B(T)$ the temperature dependent case B recombination parameter. The left-hand side of eq.2.18 expresses the change in the ionized radius due to ionizing radiation, i.e. subtracting it's expansion due to the expansion of the Universe and given the amount of neutral hydrogen at the boundary of the sphere (assuming a thin ionization front). The right-hand side expresses the amount of ionizing photons that is able to reach the surface of the sphere. For that we need to subtract the total value of the escaping ionizing radiation by the number of photons needed to balance recombination. Since recombination is a two particle process this quantity evolves with the square of the hydrogen density. Furthermore, the rate is amplified if the density field is not perfectly homogeneous but contains denser clumps which is described by the clumping parameter defined as [94]

$$C = \frac{\langle n^2 \rangle}{\langle n \rangle^2}, \tag{2.19}$$

with n being the density of the gas. Finally, the case B recombination parameter accounts for the fact that only recombination where the electron initially ends up in the second hydrogen orbital reduces the budget of ionizing photons, as recombination directly into the ground state would emit another ionizing photon thus leaving the ionizing photon budget unchanged. These bubbles continue to grow as more halos are formed and more ionizing photons are produced and eventually neighboring bubbles begin to overlap.

To describe the fraction of the IGM that is ionized we introduce the porosity parameter Q_{HII}. It is defined as

$$Q_{HII} := \frac{V_{\mathrm{ion}}}{V} \approx \frac{\frac{4}{3}\pi \sum_j r_{I,j}^3}{V}. \tag{2.20}$$

Here V_{ion} is the volume occupied by the ionized bubbles, which can be approximated by the sum of the volumes of all ionized bubbles[2]. The evolution of the porosity parameter is given by [128]

$$\frac{\mathrm{d}Q_{HII}}{\mathrm{d}t} = \frac{\dot{n}_{\mathrm{ion}}(z)}{n_H} - C(z) n_H \alpha_B(T) Q_{HII}. \tag{2.21}$$

Here $\dot{n}_{\mathrm{ion}}$ is the escape density rate of ionizing photons. The growth of the porosity is hence driven by the density of ionizing photons escaping into the IGM and suppressed by the recombination of already ionized gas analogously to the the process of bubble growth we considered earlier. Reionization can be considered completed once $Q_{HII} = 1$.

[2]This approximation breaks down once the bubbles overlap.

Chapter 3

The Lyman continuum escape fraction

The focus of this chapter is to introduce the Lyman continuum (LyC) escape fraction in the galactic environment. We then explore the astrophysical production mechanisms of LyC photons. Next we need to understand the medium the photons escape from namely the ISM before finally discuss how it the ISM interacts with LyC photon. In the end we discuss how the LyC escape can be modelled theoretically and directly and indirectly observed.

3.1 The process of ionization

In a neutral hydrogen atom its electron is in the 1s orbital i.e. its probability wave function is isotropically distributed around it positively charged nucleus. In this state the hydrogen atom has a binding energy of approximately $E = 13.6\text{eV}$. In order for the atom to become ionized the system needs to absorb more energy than this binding energy. However, due to the discrete nature of the energy states in the bound atom, only photons with certain frequencies can be absorbed by the atom. If that energy is below the binding energy of the atom the electron can transitions into a higher energy state. However, this state is usually short lived and the atom soon after reverts back to its ground state emitting a photon with the same energy as the one that was absorbed [1]. When the atom interacts with a photon carrying an energy higher than the atoms binding energy the electron has a probability to absorb that photon and become unbound from the proton. The probability of this happening can be calculated using Fermi's golden rule

$$\Gamma_{\mathrm{i}\to\mathrm{f}} = \frac{2\pi}{\hbar}|\langle f|H'|i\rangle|^2\rho(E). \tag{3.1}$$

Here, $\Gamma_{\mathrm{i}\to\mathrm{f}}$ is the transition rate (probability per unit time), $\langle f|$ is bra vector of the final state and $|i\rangle$ the ket vector of the final state, H' is the perturbation to the Hamiltonian

[1] The energy is not exactly the some energy could be converted into the atoms kinetic energy or vise versa. This slight shift in the photons energy will become important later on.

of the system created by the interaction of the atom with the photon. Finally$\rho(E)$ is the density of free states with the energy E. The ionization rate can be related to the cross section through

$$\sigma_{\mathrm{H}}(E) = \frac{E_\gamma \Gamma_{\mathrm{i}\to\mathrm{f}}}{I(E_\gamma)}. \tag{3.2}$$

Where E_γ is the photon energy and $I(E_\gamma)$ is the intensity of the photon. The evaluation of this term is quite complex and can be either solved numerically or it can be approximated using e.g. the Born method. The result is that the cross section scales as

$$\sigma_H(E) \propto (E_\gamma - E_0)^{-\frac{7}{2}}, \tag{3.3}$$

with $E_0 = 13.6\mathrm{eV}$ being the binding energy of the hydrogen atom. This means that the cross section steeply decreases as the photon energy becomes much larger than the binding energy of the atom. This means that on average a high energy photon can travel much further through a gas cloud which explains why x-ray photons emitted from high energy sources such as x-ray binaries and quasars can affect the IGM to far larger distances than stellar photons.

However once a fraction of hydrogen atoms is ionized. There is also a probability that an ion encounters a free electron and recombines. The probability for this to happen is given by

$$R_{\mathrm{H}} = x_{\mathrm{HII}}^2 n_{\mathrm{H}}^2 \alpha. \tag{3.4}$$

Here R_{H} is the recombination rate of hydrogen usually measured in $\mathrm{cm}^{-3}\mathrm{s}^{-1}$, x_{HII} the fraction of hydrogen that is ionized and n_{H} the density of hydrogen. Finally, *alpha* is the temperature dependent recombination parameter. Just as the cross section it can be derived with Fermi's golden rule, however the calculations are more complex such that is is usually either obtained through simulations or experimental measurements. Since recombination occurs in a two particle encounter in scales with the square of the ionized photons. This also means that dense molecular clouds are particularly resistant to ionization. This drastically limits the escape of ionizing radiation from star formation clouds as these are particularly dense. Given, as we will later see, that most ionizing radiation is produced by relatively short lived stars which do not have much time to dissolve their birth clouds through ionization and radiation pressure, this greatly limits the potential escape of ionizing radiation.

Finally, in a large fraction of recombination events the electron recombines with the ion into the ground state of the hydrogen atom. This however, releases a photon with an energy equal to the binding energy of the hydrogen atom and the free energy of the electron. Hence, the released photon is able to ionize another atom. Therefore, if the gas is sufficiently dense, recombination events into the ground state do not affect the total ionization state of the gas. As a result, most simulations and analytical models use the case B recombination parameter α_B. This parameter only accounts for the probability that the electron recombines into a higher state orbital before falling back into the ground state. Hence it releases two photons one when it recombines and another one when it falls into the ground state. The later photons is non-ionizing, and the first photon is unlikely

to be as electrons with the free energy needed for the photon to be ionizing are unlikely to recombine.

3.2 Astrophysical production of LyC photons

Where does ionizing radiation during the era of reionization come from? As we have discussed in the previous chapter the first generation of stars tend to be heavy population III stars. These stars likely produce a large amount of ionizing radiation. However, they are short lived and quickly enrich their host galaxy with metals. The next generation of stars (Pop II) are formed in GMCs as they collapse and fragment into denser clouds which themselves collapse into protoplanetary discs. Eventually, these disc accumulate enough gas that their cores become sufficiently dense and hot to ignite nuclear fusion. Nuclear fusion heats up the core of the star and keeps it stable against further gravitational collapse.

As the star reaches pressure equilibrium, it will have a temperature gradient from its core to its surface. Given its surface temperature T, it will emit radiation in accordance to the the Stefan-Boltzmann law

$$P = 4\pi r^2 \sigma_{\mathrm{SB}} T^4, \tag{3.5}$$

with P being the output power, r the radius of the star and σ_{SB} the Stefan-Boltzmann constant. Here we approximate the star as a black body which in terms of the total power output is reasonable. The very steep scaling with temperature implies that hot stars emit radiation at a far greater rate than cooler stars, rapidly loosing the energy produced in the fusion processes. Eventually, these stars run out of fuel and the stars collapses igniting the rapid fusion of heavier elements and exploding into a supernova. The energy distribution of the photons emitted from a black body is given by Planck's law

$$B(E_\gamma, T) = \frac{2E_\gamma}{h^2 c^2} \frac{1}{\exp\left(\frac{E_\gamma}{k_B T}\right)}, \tag{3.6}$$

depicted in fig. 3.1. Here E_γ is the photon energy, $B(E_\gamma, T)$, is the spectral emissive power per unit area and per unit solid angle, h is Planck's constant, c the speed of light and k_B the Boltzmann constant. This law emerges as the maximum entropy solution of bosonic particles, in this case photons. The maximum of this function is given by the Wien displacement law

$$E_{\gamma,\max} = 2.431 \times 10^{-4} \mathrm{eV/K} \cdot T. \tag{3.7}$$

This implies that in order for this maximum to be located within the ionizing range the temperature has to be $T \gtrsim 5.5 \times 10^4 \mathrm{K}$.

Such temperatures can only be reached by O class stars with solar masses of $\gtrsim 16 M_\odot$ which only make up $\sim 0.00003\%$ [114] of stars at the current point in time. There are very rare, because these stars have a very short lifetime and producing ionizing photons for only ~ 3 million years [177]. However, it should also be noted that their luminosities

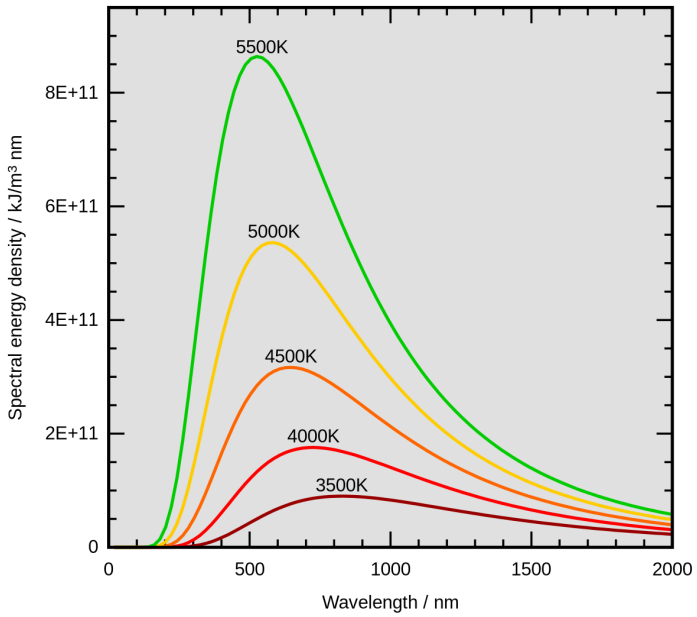

Figure 3.1: Examples of Planck spectral distributions for various temperatures. [2]

is several orders of magnitude higher than of e.g. our sun. Furthermore, it should be taken into account that the high temperature requirement is needed for the the peak of the Planck distribution to be in the ionizing energy range, but a seen in fig. 3.1 there is a significant contribution of radiation to the left of the peak. Hence, even slightly cooler B type stars with temperature $\sim 10^4 - 3 \times 10^4$K contribute significantly to the ionizing photon production. Additionally, these slightly cooler stars have a longer lifetime such that the can produce ionizing radiation after their birth cloud is dissociated which will be important for the discussion of the LyC escape fraction.

Another important property of many heavier stars is that they form in binary systems. This has profound effects on the production of ionizing photon production through the interaction and mass exchange between the two stars. The interactions can remove the cooler outer layer of hydrogen revealing the significantly hotter helium layer, exchange mass and thus provide fuel for continued fusion processes and finally merge into a brighter hotter star [49]. Thus the presence of binary systems can increase both the rate of LyC photon production of stars with a given mass as well as the duration during which stars are producing ionizing photons.

Another specific class of binary systems is the x-ray binary. This system usually consists of a star and a compact object such as a black hole or neutron star. If the star fills its Roche lobe mass begins to be transferred to the compact object forming an accretion disc and releasing a part of its gravitational energy as X-ray radiation [197]. This particularly hard radiation is unlikely to significantly contribute to the process of hydrogen reionization but could effect the reionization of helium [126]. Additionally, active galactic nuclei (AGN) contribute significantly to the heating of the IGM (e.g. [64]).

Another source of ionizing radiation are accretion disc of massive black holes at galactic centers, so called quasars. Here, similarly to the X-ray binaries, radiation is produces by gas falling into a black hole and forming an accretion disc around it. These source produce large amounts of X-ray photons. However, the abundance of quasars is relatively low such that the total density of photons emitted from quasars is unlikely to be sufficient to significantly contribute to hydrogen reionization [166, 81, 45, 36, 154]. However, their contribution is of fundamental importance for the second ionization of helium which requires $E_\gamma \gtrsim 54\text{eV}$ [126], as well as the heating of the IGM.

3.3 Propagation of ionizing photons through the ISM

In order to escape into the IGM, LyC photons have to propagate through the gas within the galaxy. The gas however, is present in multiple states of temperature and density and is further affected by radiational and hydrodynamic feedback caused by star-formation and subsequent supernova explosions.

After a star forms it is initially surrounded by the GMC it was formed in. The gas in a GMC is usually cold with a temperature of $10 - 20\text{K}$ and relatively dense with a particle density of $n = 10^2 - 10^6\text{cm}^{-3}$[56]. GMCs have usually a size of 10s of pc, however their large density makes recombination very efficient due to the quadratic scaling with the density (see eq. 3.4). This means that at first all the ionizing radiation emitted from young stars is absorbed in their vicinity.

The radiation from young stars however dissociates hydrogen molecules through photodissociation and heats up the hydrogen gas. This creates thermal pressure outwards, eventually destroying the GMC. In addition to photodissociation, the first supernovae that explode create hydrodynamic feedback, as shock waves from the explosions push the gas of the GMC outward. As a result GMCs are usually destroyed only $\approx 10\text{Myr}$ after their formation [50]. Nonetheless, this would surpass the lifetimes of many O class stars and greatly reduce the amount of LyC photons which is able to escape. Several additional processes were proposed that could increase the amount of photons escaping at these smaller scales. One being the binary systems discussed above where the lifetime and luminosity of stars is extended through mass exchange. Additionally, the presence of two hot stars at one location greatly increases the local LyC output which increases the rate at which the GMC is photodissociated around these systems. Another process is the creation of runaway stars. These are stars moving at a speed of $\sim 30\text{kms}^{-1}$ which allows them to leave their birth cloud on timescales shorter than the lifetimes of massive stars facilitating their LyC escape. Two methods have been proposed for the creation of runaway stars [158]. One is the ejection of a star through the shock wave of a supernova created by the explosion of its companion in a binary system. The other process, is through many-body gravitational interactions in star clusters. It has been suggested [34] that $\sim 30\%$ of massive stars are runaway stars.

The ISM itself is composed of multiple states of matter. Most of the mass of the galaxy tends to be located in a relatively cool gas clumps with a temperatures of $50 - 100\text{K}$ and a

density of $n = 20 - 50\text{cm}^{-3}$. However, given their large density, even though they contain most of the gas, these clumps only fill $1 - 5\%$ of the volume of the ISM. The size of the clumps is usually of the order of several hundreds of pc.

Surrounding these cold gas clumps is diffuse hot gas with a density $\lesssim 0.1\text{cm}^{-3}$ and a temperature of several thousands of Kelvin. Additionaly, some of the particularly low density gas in the interstellar and circumgalactic medium can be further heated to very high temperature of $10^6 - 10^7\text{K}$ by stellar winds emerging from supernovae explosions.

While the cold state of the ISM is a very efficient ionizing photon absorber. The hot gas in the ISM is either ionized or can be quickly ionized by photons due to its large recombination timescale and low density. The fact that the gas in the ISM consists of a mixture of the two states makes it difficult to predict how well LyC radiation can propagate through it. On the one hand the clumping of the gas into dense regions blocks ionizing radiation and shades the medium behind it. Hence, if all photons encountered clumps of cold gas, none of the radiation would be able to escape. On the other hand, if a significant fraction of the ionization radiation has lines of sight that do not encounter cold state gas due to its small filling factor, LyC radiation could escape more easily than in a scenario where the density is in a homogeneous state [40].

It should be additionally noted that most galaxies, especially young star forming galaxies have a disc form. They acquire this form through the exchange of momentum between the gas particles when they collapse into the gravitational well of the halo. This has the effect that most of the ionizing radiation can only escape perpendicular to the disc as the gas column density is smaller in that direction. Additionally, heavier discgalaxies tend to have accreting black holes at their centers. As mentioned previously the accretion discs of these black holes emit large amounts of ionizing radiation but also mechanical feedback which extends mostly perpendicular to the disc, further evacuating the medium below and above the galaxy and thus facilitating the escape of LyC radiation in these directions. This contribution is particularly important in a scenario where reionization is dominated by heavy galaxies, so called oligarchs [141].

The escape of LyC radiation is further influenced by metal enrichment. Hereby, metals created in stars and dispersed by supernovae form dust grains. Since, the formation of dust grains strongly depends on the metallicity of the gas in which they form, as more metals facilitate the formation of grains, the effect of dust on the escape of LyC photons is lower during the era of reionization than it is today, given that at early times less metals have formed. However, high redshift surveys (e.g. [19]) have shown that dust absorption is already detectable at the redshifts of reionization. A particular feature of dust absorption is that its cross section does not decline as rapidly with photon energy as the ionization cross sections of hydrogen and helium (eq. 3.3). This means that its contribution becomes particularly significant for the absorption of higher energy photons.

Finally, past star formation and the past interactions with radiation has a significant effect on the propagation of LyC photons at a later point in time. On the one hand, mechanical feedback from supernovae and past LyC production can evacuate and ionize channels within a galaxy through which photons can escape more easily thus increasing the escape fraction. On the other hand however, gas in the galaxy is heated by these processes

and pushed out of the galaxy. This reduces the amount of star formation within the galaxy thus quenching it. This is particular significant for smaller galaxies where the gas resides in shallower potential wells, such that less feedback is needed to drive the gas out.

3.4 Modelling LyC escape

As mentioned in the previous chapter reionization is mainly driven by stellar LyC photons escaping into the IGM. Therefore, our understanding of reionization is directly linked to our model of LyC escape from galaxies. Many studies have been conducted that model LyC escape either in isolated halos and galaxies or in larger cosmological volumes. Nonetheless, all of these models encounter the issue of the considerable dynamic range between LyC propagation through the interstellar medium (ISM) and the large-scale process of IGM reionization. This section showcases a selection of studies that utilize a range of methods, either directly or indirectly, to model LyC escape and its effects on reionization. The aim is to provide an overview of the diversity in methodology and outcomes, thus contextualizing our studies within the wider literature.

As [93] show, in order to have a convergent reionization history a simulation box of at least 100cMpc is required. The required box size becomes even larger for studies of the 21cm line signature of reionization. Numerical and semi-analytic studies tend to follow a general trend, whereby either a simplified model for LyC escape is utilized, but a large volume is modelled, or conversely, a more complex model is employed for LyC escape, but at the cost of modelling a smaller volume. Additionally, a major challenge in constraining the escape fraction is its degeneracy with several other parameters, such as star-formation efficiency or the ratio of the UV continuum to ionizing flux, which are weakly constrained at high redshifts. This leads to a wide range of predictions for escape fractions across different studies, varying over several orders of magnitude, while remaining consistent with observational constraints.

Semianalytic models such as the ones presented in [12], [29] and [167] do not study a fixed cosmic volume but model the halo density function and the resulting emissivity density directly. In these studies, relatively simple models for LyC escape are used usually calibrated to be in agreement with observational constraints such as the CMB optical depth to reionization and Ly-α forest observations.

In [12] the authors used a galaxy independent $f_{\rm esc} = 0.3$ in their prediction of the 21cm signal. A constant $f_{\rm esc} = 0.2$ is assumed in [167] which however resulted in a very early reionization redshift of $z = 10$. However, [174] also assume $f_{\rm esc} = 0.2$ but obtain a reionization time consistent with constraints from the Hubble and Planck telescope observations. On the other hand [29] studied separately the contributions of population III and II stars assuming different but constant escape fractions of $f_{\rm esc,II} = 0.01$ and $f_{\rm esc,III} = 0.68$. A similar approach is used in the semi-analytic model presented in [205] where the interac-

tion between stellar population II and III is studied and the escape fractions are set to $f_{\rm esc,II} = 0.1$ and $f_{\rm esc,III} = 0.5$.

In large scale simulations of reionization, similarly simple models are often assumed for LyC escape as the resolution does not permit more detailed modelling. In [33] Monte Carlo radiative transfer post-processing was applied to a $20h^{-1}$cMpc box and found a constant $f_{\rm esc} = 0.05$ to be consistent with optical depth constraints of WMAP [187]. Using a similar radiation transfer post-processing [30] found that a constant $f_{\rm esc} = 0.5$ is required to match the UV luminosity function of [17] whereby a similarly sized simulation box of $35.12h^{-1}$cMpc was used.

Another approach to model LyC escape is to assume a redshift dependent escape fraction. It is based on the idea that LyC escape found at lower redshifts is insufficient to account for the LyC budget needed for reionization (e.g. [5, 164].

In the minimal reinization model of [79] the escape fraction is found to steeply increase with redshift:

$$f_{\rm esc} = 1.8 \times 10^{-4}(1+z)^{3.4}. \tag{3.8}$$

This approach results in an optical depth which is consistent with WMAP constraints.

In [112] on the other hand the degeneracy between the escape fraction and the ratio between the LyC and the 1500Å UV flux is directly taken into account by modelling only the product $\zeta_{\rm ion} f_{\rm esc}(z)$. Here, a power-law growth of this product with redshift was assumed.

In the Simulations and Constructions of the Reionization of Cosmic Hydrogen (SCORCH) the authors examined different exponents for power-law ($f_{\rm esc} \propto z^a$) scalings varying the exponent in the range $a = 0-2$. They found that all values for a provide results consistent with WMAP. However, an increase in the power a increases the duration of reionization.

The Technicolor Dawn simulation [57] models the evolution of galaxies and metals in the circumgalactic medium in an inhomogeneous UV background. It also assumes a power-law scaling of the galactic escape fraction with the exponent a being a free parameter calibrated such that the emitted photon budget is sufficient to complete reionization by $z = 6$, finding $a \approx 2 - 3.5$. Finally, the UV background modelling of [165] assumes the same form of the escape fraction as in eq. 3.8 but with a power of $a = 3.98$ and a different prefactor. Additionally, the minimal escape fraction is fixed at $f_{\rm esc,min} = 0.18$.

Alternatively, if galaxies and halos in a cosmological simulation are sufficiently well resolved, the escape of LyC photons can be modelled explicitly if radiation transfer is implemented. In [211, 212] the N-body particle mesh solver ENZO is used. It utilizes adaptive mesh refinement (AMR) to resolve particularly dense regions such as galaxies. For radiation transfer the code MORAY is used [210] which utilizes spatially adaptive ray tracing. A relative small box of 1cMpc is simulated, limiting the maximum halo mass to $M \approx 10^{8.5} M_\odot$. The authors find that LyC escape strongly decreases with halo mass

from 0.5 to 0.05 in the halo mass interval $M = 10^7 - 10^{8.5} M_\odot$ resulting in small halos contributing the majority of the ionizing photon budget to reionization.

A similar approach is used in the Cosmic Dawn (CoDa) I [150] and II simulations [149, 118]. The the difference between I and II mainly being the utilization of a different star-formation model as well as better resolution. CoDa II simulates a 94cMpc box with the hydro-RT code RAMSES-CUDATON. It is built on the RAMSES [198] AMR hydrodynamic code. However, the accurate treatment of radiation at full speed of light in the CUDATON code requires the use of a regular grid without refinement. In order to account for the LyC absorption taking place at unresolved scales a subgrid escape fraction of $f_{\mathrm{esc,loc}} = 0.42$ is assumed. The authors find that the majority of ionizing photons is emitted by halos in the mass range $6 \times 10^8 M_\odot < M_{\mathrm{halo}} < 3 \times 10^{10} M_\odot$. They argue that small halos have large escape fractions but too low SFR to contribute significantly while on the other hand very large halos have smaller escape fractions and a low abundance and therefore do not significantly contribute either.

The SPHINX simulation [177, 176] uses the RAMSES-RT code [175] to simulate 10 and 20cMpc cosmological volumes. The RAMSES-RT code utilizes AMR to resolve small scales and an M1 closure technique for the Eddington tensor [117] to model radiation transfer. However, the escape fractions are calculated in post-processing with Monte-Carlo RT to increase accuracy [176]. The study confirms the increase of the escape fraction with increasing redshift. It further found that the escape fraction is largest for halos with stellar masses of $M_\star \approx 10^7 M_\odot$ where it reaches $f_{\mathrm{esc,max}} \approx 0.1$ for $z \gtrsim 8$ and decreases to ≈ 0.05 at $z = 6$.

Finally, the THESAN simulation [100, 63] uses the hydro-RT code AREPO-RT [101] to simulate a large 95.5cMpc box using the IllustrisTNG galaxy formation model later discussed in this thesis. Given the large box size this work also utilizes a subgrid escape fraction of $f_{\mathrm{esc,loc}} = 0.37$ to account for the unresolved LyC absorption. The large volume of this project allows to model the high mass end of the galactic population. Nonetheless, the authors find that the majority of escaping LyC photons is emitted from relatively small halos with stellar masses $M_\star \lesssim 10^7 M_\odot$ for larger redshifts $\gtrsim 7$. However, at lower redshift this trend reverses with a majority of LyC photons escaping from halos with $M_\star \gtrsim 10^8 M_\odot$. They also find an on average increasing escape fraction with stellar mass as well as with redshift.

Another approach to study LyC escape is through the detailed simulation of individual halos. Here, a much better resolution can be achieved at the expense of having limited information about large scale feedback of neighboring galaxies as well as having relatively low statistical sampling. However, these simulations allow for a more detailed study of smaller scale ISM physics affecting LyC escape. They have thus provided some of the valuable insights into LyC escape through the ISM that we have discussed in the previous section.

A study of a large galaxy hosting a faint AGN [200] utilizing the previously mentioned

RAMSES-RT simulation code has shown that faint AGN do not significantly increase the LyC emissivity of their host galaxy which is dominated by its stellar population resulting in an average escape fraction of $f_{\rm esc} = 0.05$. This is in agreement with a similar previous study [201] of a $M_{\rm vir} \approx 5 \times 10^9 M_\odot$ halo hosting an AGN.

Similar RAMSES-RT studies of 3 dwarf galaxies with stellar masses in the range of $M_\star \sim 10^8 - 10^9 M_\odot$ [201] have shown that the LyC escape fraction can very significantly (of several orders of magnitude) within timescales of 10Myr. This is driven by variations in the star formation rate in the galaxy. However, there is a delay between increase in star formation and the subsequent increase in the escape fraction as the formation of escape channels is mainly driven by supernovae. This study further finds that the circumgalactic medium has significant influence on the quantitative value of the escape fraction.

The study presented in [219] investigated how metallicity and gas mass affects LyC escape. Studying a galaxy embedded in a $M_{\rm vir} = 10^{11} M_\odot$ they found that the escape fraction is strongly anti-correlated with galactic metallicity. The study determined that an increase in metallicity from $Z = 0.002$ to $Z = 0.02$ decreases the LyC escape fraction tenfold from $f_{\rm esc} \approx 0.1$ to $f_{\rm esc} \approx 0.01$. The authors attribute this to the fact that at higher metallicities stars are embedded in their dense birth clouds for a longer duration. However, they found that increasing the gas mass of a galaxy has little effect on the escape fraction showing that a five-fold increase in $M_{\rm gas}$ only reduced the escape fraction from $f_{\rm esc} = 0.1$ to $f_{\rm esc} = 0.05$.

The final approach to investigating LyC escape is through post processing galaxies retrieved from large scale hydrodynamic simulation with radiation transfer. This will be the method utilized in [110] which we will present later in this work.

Such an approach was used in [124] and [125] for the Feedback in Realistic Environments (FIRE) [88] and FIRE II [89] simulations respectively. In these studies, a large sample of individual halos were post-processed with Monte Carlo RT until radiation equilibrium was reached. There, [124] have found that the inclusion of binary stellar systems significantly enhances LyC escape by a factor of $\sim 4 - 10$ thus ensuring a sufficient ionizing photon budget for reionization. The LyC escape enhancement from binary system is explained by the longer lifetime of LyC emitting stars that we have discussed in the previous section. However, [125] find that this enhancement due to binaries is significantly lower increasing LyC leakage by a factor of ($\sim 1.6 - 1.8$). Rather the escape of LyC photons happens trough efficient star-formation close to the surface of stellar feedback shells. These feedbacks clear out gas thus facilitating the LyC escape of newly formed stars. This results in average LyC escape fractions of $\approx 0.05 - 0.25$ whereby the maximum is reached at stellar masses of $M_\star \sim 10^8 M_\odot$

Post-processing of the First Billion Years (FiBY) simulation [203], the study in [152] found a decrease in the escape fraction with halo mass. This is attributed to the denser gas at the center of massive halos due to deeper potential wells. However, large variation in the escape fraction were found at a fixed mass due to varying gas distribution within

the halo.

The RAMSES-RT zoom-in simulations studied in [106] of halos with masses $10^8 - 10^{10.5} M_\odot$ emphasizes the importance of run-away stars to LyC escape, showing that the average escape fraction of these halos increases from $\langle f_{\rm esc} \rangle = 0.11$ to $\langle f_{\rm esc} \rangle = 0.14$ when run-away stars are taken into account. However, the authors also point out the supernovae of run-away stars are more efficient at reducing star-formation through their feedback on galactic gas.

3.5 Measuring the LyC escape fraction

In order to validate theoretical models for LyC radiation escape and obtain an accurate understanding of the history of LyC escape during reionization, observations are crucial. However, direct observations of LyC escape at high redshifts are not possible due to the absorption of LyC photons by the IGM during the era of reionization. Therefore, the methodology for determining LyC escape at high redshifts usually involves finding galaxies at lower redshifts with similar properties to the galaxies expected during reionization, measuring their LyC escape, and correlating it with observable emission lines at high redshifts to estimate the LyC escape of high-redshift galaxies.

One method to infer $f_{\rm esc}$ at lower redshifts ($z < 6$) is through the ratio between the flux of photons with $E_\gamma > 13.6$eV ($\lambda < 912$Å) and the flux at $\lambda = 1500$Å which is not absorbed by Lyman Limit systems between the source and the observer [38]. The observed ratio can be related to the intrinsic i.e. emitted flux through (e.g. [95, 183, 134])

$$\left(\frac{F_{1500}}{F_{\rm LyC}}\right)_{\rm obs} = \left(\frac{F_{1500}}{F_{\rm LyC}}\right)_{\rm int} \times 10^{-0.4(A_{1500}-A_{\rm LyC})} e^{\tau_{\rm HI,IGM}} e^{\tau_{\rm HI,ISM}}. \tag{3.9}$$

Here F_{1500} and $F_{\rm LyC}$ are the fluxes from a galaxy at 1500Å and in the LyC range respectively, $A_{1500} - A_{\rm LyC}$ is the differential dust extinction, $\tau_{\rm HI,ISM}$ and $\tau_{\rm HI,IGM}$ are the optical depths of neutral hydrogen in the ISM of the galaxy and the IGM between the galaxy and the observer respectively. Using this the escape fraction can be calculated as

$$f_{\rm esc} = 10^{-0.4A(1500\text{Å})} \frac{(F_{1500}/F_{\rm LyC})_{\rm int}}{(F_{1500}/F_{\rm LyC})_{\rm obs}} e^{\tau_{\rm HI,IGM}}, \tag{3.10}$$

with $A(1500\text{Å})$ dust attenuation of the 1500Å flux, which can be derived from the relative flux excess in the B filter relative to the V filter, $E(B-V)$:

$$A(1500\text{Å}) = 10.33 E(B-V). \tag{3.11}$$

The relation is based on the empirical Calzetti law [23]. Note that this law is based on dust redenning observations in local starbursts and might change with redshift. This method of determining the escape fraction, however, relies on certain assumptions. Specifically, the intrinsic ratio $(F_{1500}/F_{\rm LyC})_{\rm int}$ must be determined by assuming the age of the observed stellar population. Additionally, assumptions must be made about the relative flux excess

$E(B-V)$ and the fraction of binary systems. Using this methodology, [95] find that $f_{\rm esc}$ rapidly increases with redshift between $f_{\rm esc} \approx 1\%$ at $z = 1$ to $f_{\rm esc} \approx 10\%$ at $z = 4$.

The problem becomes more complex when trying to determine escape fractions at $z > 6$. A method for indirect estimation of the escape fraction at high redshifts is through the measurement of the Lyman α (Lyα) line (e.g. [41]). The idea behind this approach is that in most case B recombination events of ionized hydrogen the electron first ends up in the $n = 2$ orbital before transitioning to the ground state. This last transition emits a Lyα photon with the length of $\lambda = 1215$Å. Gas dense enough to have a large number of recombination events and thus a sufficient luminosity in Lyα is mostly located in galaxies which contain large HII regions. Since the Lyα luminosity reflects the amount of recombination event its value reflect how many LyC photons are needed to keep the gas ionized. Hence, it reflects how many LyC photons are not able to escape from the galaxy

$$L_{\rm Ly\alpha} \propto (1 - f_{\rm esc})\dot{N}_{\rm ion}. \tag{3.12}$$

Here $L_{\rm Ly\alpha}$ is the Lyα luminosity, and $\dot{N}_{\rm ion}$ the ionizing emissivity of the galaxy. Note that given that Lyα photons are also scattered by neutral IGM, this method can only extend to relatively late stages of reionization during which ionized bubbles around galaxies are sufficiently large such that Lyα photons are redshifted out of resonance before encountering neutral hydrogen. The problem with this method is that while the correlation of $f_{\rm esc}$ and Lyα luminosity is relatively simple, the question remains how much of the Lyα luminosity can actually be observed, given that some of it is either absorbed by dust or scattered away by neutral ISM and IGM. Thus the modelling of another unknown, the Lyα escape fraction $f_{\rm esc,Ly\alpha}$ is required. Models of Lyα escape indicate that it is correlated with LyC escape [41]. This results in the observed Lyα luminosity being positively correlated with the LyC escape fraction for small values of $f_{\rm esc}$. However, when $f_{\rm esc}$ becomes sufficiently large this relation turns around as the amount of produced Lyα luminosity becomes the decisive factor [41].

Another approach to predict $f_{\rm esc}$ at high redshift is the ratio between the OIII ($\lambda = 5007$Å) and OII ($\lambda = 3727$Å) lines [144, 143]. The idea behind this method is that the first ionization energy of oxygen is approximately $E_{\rm O+} = 13.6$ eV and thus very close to the ionization energy of hydrogen making the HII and OII regions approximately equal in size. Further, the HII and thus OII regions of a gas cloud can either be density-bounded or ionization-bounded. In the case of an ionization-bounded HII region (as shown in fig. 3.2 left), the size of the region is limited by the ionization front boundary. When in radiation equilibrium, this means that no radiation can escape from the gas cloud. However, in a density-bounded HII region (as shown in fig. 3.2 right), the sources can fully ionize the cloud, allowing LyC radiation to escape. In practice, most gas clouds are a combination of the two modes due to the typical anisotropic density distribution. On the other hand, the second ionization energy of oxygen ($E_{\rm O2+} = 35.1$ eV) is much larger, resulting in very few photons produced by stellar sources with such energies. This causes the OIII region to be much smaller than the OII region and insensitive to whether the HII region is density or ionization-bounded. However, in a density-bounded HII region, the Strömgren sphere is

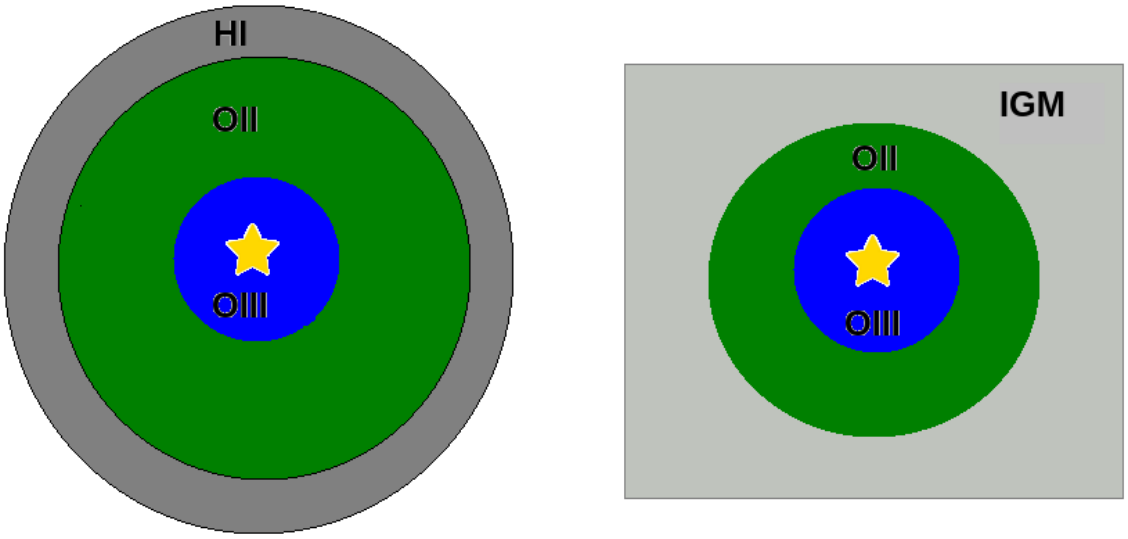

Figure 3.2: Schematic diagrams of a ionization (left) and density (right) bounded regions. In the green (OII) and blue (OIII) regions hydrogen is ionized. Note that in both cases the OIII region has the same size while the OII region in the density bounded case is significantly smaller.

not reached within the gas cloud, causing the HII cloud to be smaller than the gas cloud that could be ionized by the source. Thus, in an ionization-bounded (i.e., LyC leaking) cloud, the ratio between the OIII and the OII line is larger. Observing this ratio, which can be done down to high redshifts ($z > 6$), can provide evidence of whether a given galaxy is LyC leaking or not. Using this approach to infer escape fraction of 29 high redshift ($4.5 \leq z \leq 8$) galaxies observed with JWST, [130] find an average escape fraction $\langle f_{\rm esc} \rangle = 0.12$ with 80% of galaxies having $f_{\rm esc} > 0.05$.

Emissions from Magnesium ions have additionally be proposed as tracers of LyC escape. The MgII $F_{\lambda 2796}/F_{\lambda 2803}$ doublet ratio, which was initially discovered to be correlated with Lyα escape [87], has been identified as a valuable indicator of LyC escape, as suggested by recent studies [27, 215]. The idea behind this method is that the MgII ionization energy is 15eV and thus close to the HI ionization energy. Therefore, it is a tracer of neutral hydrogen. In an optically thin regime, the doublet ratio is given by collisional excitation and is equal to 2. Meanwhile in a optically thick regime it is dominated by photo excitation and is close to 1. Thus a large ratio between the lines is an indicator of low MgII and HI abundance and therefore of a large LyC escape.

Another indicator of LyC escape is the CII λ1036, which was first introduced in [86] and further developed in [85] and [116]. The former also identified the CII λ1334.5 line as an additional indicator. This method is based on a similar idea as the previous methods, namely that the ionization energy of CII is 11.3eV, and thus CII traces HII regions. To estimate the escape fraction quantitatively, the flux at these lines is divided by the con-

tinuum emission. The concept is that a strong CII absorption line correlates with regions that have a low HI content within the galaxy, indicating the presence of ionized channels. Using this method [116] found an $f_{\mathrm{esc}} < 2.4\%$ for the compact blue galaxy Haro 11 from the FUSE spectrograph [139]. Analyzing a larger set of galaxies [85] find only upper bounds for escape fractions of galaxies observed with FUSE the highest upper bound being $f_{\mathrm{esc}} < 18\%$ but find significant escape fractions of up to $f_{\mathrm{esc}} = 40\%$ for galaxies observed with the COS spectrograph [59].

Chapter 4

Ionizing photon production and escape fractions during cosmic reionization in the TNG50 simulation

The content of this chapter has been published as Kostyuk et al. [110].

Abstract

In this work we investigate the dependence of the escape fraction of ionizing photons, $f_{\rm esc}$, on various galaxy and host halo properties during the epoch of reionization. We post-process the TNG50 magneto-hydrodynamical simulation from the IllustrisTNG project using the 3D multi-frequency radiative transfer code CRASH. Our work covers the stellar mass range $10^6 \lesssim M_\star/\mathrm{M}_\odot \lesssim 10^8$ at redshifts $6 < z < 10$. Adopting an unresolved, cloud-scale escape fraction parameter of unity, the average halo escape fraction $f_{\rm esc}$ increases with mass from ~ 0.3 at $M_\star = 10^6\,\mathrm{M}_\odot$ to ~ 0.6 at $M_\star = 10^{7.5}\,\mathrm{M}_\odot$, after which we find hints of a turnover and decreasing escape fractions for even more massive galaxies. However, we demonstrate a strong and non-linear dependence of $f_{\rm esc}$ on the adopted sub-grid escape fraction, resulting in uncertainties for the absolute value of the escape fraction. In addition, $f_{\rm esc}$ has significant scatter at fixed mass, driven by diversity in the ionizing photon rate together with a complex relationship between (stellar) source positions and the underling density distribution. The global emissivity is consistent with observations for reasonable cloud-scale absorption values, and halos with a stellar mass $\lesssim 10^{7.5}\,\mathrm{M}_\odot$ contribute the majority of escaping ionizing photons at all redshifts. Incorporating dust reduces $f_{\rm esc}$ by a few percent at $M_\star \lesssim 10^{6.5}\,\mathrm{M}_\odot$, and up to 10% for larger halos. Our multi-frequency approach shows that $f_{\rm esc}$ depends on photon energy, and is reduced substantially at $E > 54.4$eV versus lower energies. This suggests that the impact of high energy photons from binary stars is reduced when accounting for an energy dependent escape fraction.

4.1 Introduction

The last major phase transition in the Universe, the reionization of the intergalactic medium (IGM), took place during its first billion years. During this era matter collapsed into bound objects and the first stars and galaxies formed, at redshifts as high as $z \approx 30$ [121]. The radiation produced by these first luminous sources was able to eventually ionize the gas of the diffuse IGM.

The Planck measurements of the Thomson scattering optical depth, of CMB photons scattered by the free electrons released during reionization, give a value of $\tau_e = 0.056 \pm 0.007$ [6]. Given the scenario of an instantaneous reionization process, this corresponds to a redshift $z_{\rm ion} = 7.68 \pm 0.79$ for complete reionization. However, the reionization history of the Universe is much more complex and depends, at a minimum, on the detailed distribution, timing, and properties of the sources of ionizing radiation.

Both active galactive nuclei (AGN; e.g. [127]) and star forming galaxies (e.g. [174]) have been suggested as the main drivers of reionization. However, recent semi-analytic (e.g. [166]) and semi-numeric (e.g. [81]) models, hydrodynamic plus radiation transfer (RT) simulations (e.g. [44]), as well as measurements of AGN at $z \approx 6$ [36, 154, 99] indicate that the abundance of these sources at high z is likely too low to dominate the ionizing photon budget. This leaves galaxies as the most likely drivers of reionization. Nevertheless, it is not well understood which galaxies contribute the most, and how the diversity of physical properties of galaxies control their relative efficiency of ionizing photon emission.

So far, the reionization process has been modelled with different methods. Semi-analytic models (e.g. [11, 62, 29, 167, 166]) have been generally applied to describe the evolution of the mean properties of the IGM, and are particularly useful when investigating parameter dependencies due to their speed and flexibility. In semi-numeric models (e.g. [180, 136, 61]) the density distribution is derived based on e.g. an excursion set formalism (but see e.g. also the N-body simulation based [92]), and used in combination with assumptions on source properties and the formation of ionized bubbles, in order to model the reionization process.

Finally, there are a number of approaches that combine N-body/hydrodynamical simulations and RT calculations. In this context a trade off is made between large scales, needed to properly capture the evolution of large ionized regions – which, towards the end of the reionization process, can measure tens of cMpc (see e.g. [21]) – and small scales, needed to model the properties of the stars and interstellar medium gas within galaxies themselves. The inclusion of RT adds further computational complexity and can be treated either in post-processing or directly on-the-fly with coupled radiation-hydrodynamical (RHD) simulations [199, 65]. Post-processing enables large scale ($\gtrsim 100h^{-1}$cMpc) simulations, and the inclusion of more expensive, multi-frequency treatments [93, 44]. On the other hand, smaller scale simulations in which the RT equation is solved together with the hydrodynamics offer a self-consistent coupling with the underlying gas dynamics and astrophysical models [68, 10, 69, 155, 177, 151, 100].

A crucial quantity controlling the reionization process is the 'escape fraction' $f_{\rm esc}$, the

ratio of ionizing photons which escape into the IGM relative to the total produced. The escape fraction is sensitive to the small scale production and propagation of ionizing Lyman continuum (LyC) photons in the galaxy. Simultaneously, the escape fraction also controls the large scale ionization of the IGM.

Observationally, it is not currently possible to directly identify high redshift leakers of LyC photons, and measurements of $f_{\rm esc}$ can only be performed at lower redshifts with relatively small samples of galaxies (see e.g. [97, 14, 28, 137, 140]). Therefore, it has been suggested that other properties of LyC emitters may correlate with a high transmission of ionizing photons, and that these observables could be used as proxies for $f_{\rm esc}$. Possible properties of this type include the strength and details of the Lyman-α line of hydrogen ([41, 202, 26]), the [O III]/[O II] optical line ratio ([51, 26, 102, 13]), as well as emission from the Mg II doublet at 2796Å and 2803Å [216]. However, these proxies are not perfect: the ratio between the Lyα and ionizing luminosity is not precisely determined [96, 75], a large [O III]/[O II] ratio is only a necessary but not sufficient condition for strong LyC leakage (see [143]), and the Mg II doublet emission tends to correlate with the dust content rather than with neutral hydrogen, limiting its use to only finding LyC leakers in the optically thin regime [103]. Additionally, $f_{\rm esc}$ values measured at low redshift are not directly applicable to higher redshifts, as the physical properties of galaxies and their source populations evolve ([217, 168, 54, 41, 212, 181, 164]).

It is also possible to directly estimate the escape fraction of ionizing radiation from numerical simulations, and numerous cosmological RHD simulations have been used for this purpose. These include the CoDa [150] and CoDa-II [149, 118] simulations, which use the RAMSES code and are run in a 95cMpc box with a dark matter (DM) particle mass of $m_{\rm dm} = 4.07 \times 10^5 {\rm M}_\odot$ and a grid resolution of 23ckpc. Other RHD simulations employing various physical models within RAMSES include those by [106] and [151], which have box sizes of $25h^{-1}$cMpc and $8h^{-1}$cMpc, respectively, with a particle mass of $m_{\rm dm} = 1.6 \times 10^5 {\rm M}_\odot$ and $m_{\rm dm} = 5 \times 10^4 {\rm M}_\odot$. The SPHINX simulations have realized boxes with side lengths of 5, 10 and 20cMpc, with a mass resolution of $m_{\rm dm} = 3.1 \times 10^4 {\rm M}_\odot$ and $2.5 \times 10^5 {\rm M}_\odot$ respectively [177, 176] and a minimum cell width of 76cpc. These are slightly smaller volumes, with higher resolution, than the CROC [69] and Aurora [155] simulations for which detailed analyses of the escape fraction are unavailable. Most recently, the THESAN simulation couples the IllustrisTNG galaxy formation model to a RT solver, running a 95.5cMpc box with a gas mass resolution of $m_{\rm gas} = 5.8 \times 10^5 \, {\rm M}_\odot$ and a simplified ISM model at scales < 300pc. [100, 63, 185, 218].

Broadly speaking, most studies of halos in the mass range $\approx 10^6 - 10^{11} {\rm M}_\odot$ find that $f_{\rm esc}$ decreases with increasing halo mass (e.g. [172, 213, 107, 168, 106]) and decreasing redshift (e.g. [60, 168, 106]). The physics behind the scaling of escape fraction with galaxy mass, and galaxy properties, are complex. The giant molecular clouds in which stars form are dense and therefore effective at absorbing radiation. At the same time, they host most of the short lived O and B stars that produce the bulk of ionizing radiation. For this reason, runaway OB stars which leave their formation sites early and therefore emit LyC radiation in a less opaque environment are thought to be a major contributor to LyC escape (e.g. [34, 106]). Similarly, because binary systems emit ionizing photons on timescales longer

than single stars, they continue to produce ionizing radiation also after the dissolution of their birth clouds, providing a major contributing factor to the escape of LyC photons [124, 177, 125]. Finally, the rapidly expanding super-bubbles produced by young stars (e.g. [42, 125]) are also crucial in aiding the escape of LyC photons from such environments.

In order to explore the escape of ionizing radiation through the epoch of reionization, we turn to the TNG50 magneto-hydrodynamic (MHD) simulation [160, 146]. We post-process halos at $6 < z < 10$ with the Monte Carlo RT code CRASH (e.g. [32, 73, 67], thereby incorporating the impact of ionizing radiation on the surrounding hydrogen and helium.

While simulations which directly couple radiation to hydrodynamics are able to capture the radiation-gas back-reaction self-consistently, the Monte Carlo approach we adopt here has complementary strengths. It allows for a more accurate solution of the radiative transfer equation, capturing better effects such as shadowing, as well as a much better sampling of the source spectral energy distributions. Our approach in this respect is similar to that adopted by [152] for the First Billion Year project and by [125] for the FIRE-II simulations. These studies necessarily neglect e.g. the evacuation of gas through radiation pressure, or RT-driven escape channels, which might lead to an underestimation of the escape fraction of more massive halos. It might also lead to underestimation of the effect past star formation had on the formation of escape channels [176]. Ideally, an accurate RT transfer method can be coupled on-the-fly to hydrodynamical simulations. However, due to the high computational requirements, all currently coupled RHD simulations have to reduce the accuracy of the RT treatment in some manner, as well as the simulation volume and/or resolution. Our trade-off is to adopt a more accurate MCRT method. In doing so, we give up on the dynamic coupling to the hydrodynamical gas evolution.

The paper is structured as follows. In Section 4.2 we describe the simulations and our analysis methodology. We present our main results, including the inferred escape fraction from galaxies, in Section 4.3. In Section 4.4 we summarize our main conclusions, their implications, and discuss future steps.

4.2 Method

4.2.1 The IllustrisTNG simulations

The IllustrisTNG project [159, 191, 142, 145, 129] consists of three different cosmological large-scale simulations, TNG300, TNG100 and TNG50 [146, 160], covering volumes of $(302.6\text{Mpc})^3$, $(110.7\text{Mpc})^3$ and $(51.7\text{Mpc})^3$, respectively. The simulations were run from a redshift of $z = 127$ to the present day, and tested in this stringent low redshift regime. This provides some confidence that the higher redshift halos we post-process are realistic progenitors. The initial conditions were generated using the N-GenIC code [192] and cosmological parameters consistent with values from the [162], namely $\Omega_\mathrm{m} = 0.3089$, $\Omega_\mathrm{b} = 0.0486$, $\Omega_\Lambda = 0.6911$, $h = 0.6774$, $\sigma_8 = 0.8159$ and $n_s = 0.9667$.

The TNG simulations were run with the AREPO code [189], which is used to solve

the equations of ideal MHD [153] describing the non-gravitational interactions of baryonic matter, as well as the gravitational interaction of all matter. All use the same TNG galaxy formation model [207, 161]. Star formation occurs by stochastically converting gas cells into star particles above a density threshold of $n_{\rm H} \approx 0.1\,{\rm cm}^{-3}$ following the Kennicutt-Schmidt relation [190]. For these stars a Chabrier initial mass function (IMF) [25] is assumed. Star formation and pressurization of gas in the ISM follows the [190] model, where sub-grid physical processes provide pressure support for the star forming gas, thereby accounting for feedback below the resolution limit. The TNG simulations track chemical enrichment of the gas, following H, He, C, N, O, Ne, Mg, Si, Fe and Europium, as well as the total gas metallicity. Stellar feedback from supernovae is included with a decoupled kinetic galactic wind model [161]. In addition, supermassive black holes (SMBHs) are treated as sink particles which form with a seed mass of $8 \times 10^5 h^{-1} M_\odot$at the center of halos which surpass a total mass threshold of $10^{10.8} M_\odot$. Subsequently they grow via gas accretion following the Bondi formalism, limited to the Eddington rate, as well as via SMBH-SMBH mergers. Feedback from SMBHs is modeled via a multi-mode scheme, including thermal heating and radiative influences (at high accretion rates), as well as a kinetic wind (at low accretion rates), all depositing energy into the surrounding gas [207].

While the simulations do not include on-the-fly RT and radiation from local ionizing sources, the time-variable though spatially uniform UV-background (UVB) radiation field of [53] (FG11 version) is turned on at $z < 6$ [161]. Note that this differs from the gradual build up at redshift $6 < z < 9$ as prescribed by [53]. Recent updates and many alternative models for the evolving UVB exist [52, 165], with implications for low-density gas heating.

In this work we exclusively use the highest resolution simulation, TNG50 [160, 146], with a dark matter particle mass resolution of $4.5 \times 10^5 M_\odot$. The initial mass of gas cells is $8.5 \times 10^4 M_\odot$, and during the simulation this value evolves within a factor of two due to the refinement and de-refinement of Voronoi cells. Stellar particles inherit the mass of the baryonic gas cell they are formed in, and then lose mass due to stellar evolution processes. For reference, at $z = 6$ the star-forming gas cells reach a minimum of 2.7 physical parsecs in size, while the mean (median) size of star-forming gas is 144 pc (154 pc) with 16-84th percentiles from 96 to 184 pc.

Halos are obtained with the SubFind algorithm [193], which runs on friends-of-friends (FoF) identified structures [37]. Subhalos and halos require a minimum of 20 and 32 particles, respectively, such that halos with a total mass down to $\sim 10^{6-7} M_\odot$are identified. In this work we consider only central galaxies above a minimum stellar mass of $M_\star \geq 10^6 M_\odot$to ensure they are reasonably resolved, with at least 20 stellar particles which typically have $\gtrsim 500$ gas cells. At $z = 6, 8$ and 10 there are 36,000, 14,000, and 5,000 galaxies sufficiently massive, respectively. From these large samples we select smaller random subsets in bins of log stellar mass for further processing.

4.2.2 Radiation transfer with CRASH

The cosmological radiative transfer scheme for hydrodynamics (CRASH) is a Monte Carlo algorithm for modeling radiation transfer on a Cartesian grid [32]. It captures the interac-

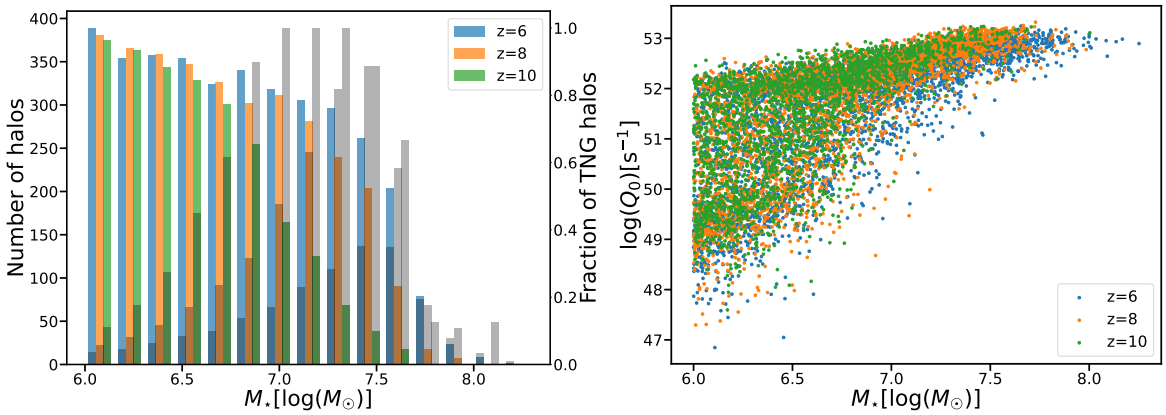

Figure 4.1: *Left panel*: Number of halos post-processed with CRASH RT in a given mass bin for the fiducial configuration (see Table 4.1). Over plotted in grey is the fraction of halos in a given TNG50 snapshot that we post-processed: right-hand y-axis. *Right panel*: Intrinsic emissivity, in ionizing photons per second, of each halo. Our complete sample at redshifts $z = 6, 8, 10$ is shown by the blue, orange, and green symbols, respectively. At all redshifts we restrict to a galaxy stellar mass range of $10^6 < M_\star/\mathrm{M}_\odot \lesssim 10^8$.

tion of ionizing radiation with hydrogen and helium gas [132, 131], as well as atomic metals [74]. Spectral distributions of sources are accounted for through frequency-binned photon packets. Recently, absorption due to dust grains has also been incorporated [66, 67].

Each CRASH simulation requires as input the total gas number density, n_{gas}, in each grid cell, as well as the initial physical properties of the gas, i.e. its temperature, T, and the fraction, x_i, of each considered ionization state i. Finally, a list of the position, spectral energy distribution (SED) and emission rate of ionizing photons, $\dot{N}_j$, of all point sources is needed as well[1].

When the RT simulation is run, each source emits N_p photon packets, at regularly spaced time intervals. Each packet contains

$$N_j = \frac{\dot{N}_j t_s}{N_p} \tag{4.1}$$

individual photons distributed over a given number of frequency bins, with the distribution being determined by the SEDs of the sources. Here t_s is the total time of the RT simulation. As a photon packet crosses a given grid cell, the optical depth is calculated as

$$\tau_{i,\nu} = n_i \sigma_{i,\nu} l, \tag{4.2}$$

where ν is the frequency bin, l is the length of the path through that grid cell, n_i is the local density of species i and $\sigma_{i,\nu}$ its cross section in that frequency bin. The number of

[1]Note that each quantity should be written also as an explicit function of the grid cells, e.g. T^c, but for the sake of clarity we omit such additional index.

Run	Photon packets	$f_{\rm esc,loc}$	Dust
fiducial	$\mathbf{10^8}$	**1.0**	**no**
dust	$\mathbf{10^8}$	**1.0**	yes
fesc_0.1	$\mathbf{10^8}$	0.1	**no**
fesc_0.3	$\mathbf{10^8}$	0.3	**no**
fesc_0.5	$\mathbf{10^8}$	0.5	**no**
fesc_0.7	$\mathbf{10^8}$	0.7	**no**
conv_5e6	5×10^6	**1.0**	**no**
conv_8e6	8×10^6	**1.0**	**no**
conv_1e7	10^7	**1.0**	**no**
conv_5e7	5×10^7	**1.0**	**no**
conv_1e9	10^9	**1.0**	**no**

Table 4.1: Characteristics of our RT simulation runs. From left to right: name; number of photon packets emitted from each stellar particle in the RT simulation; local (i.e. subgrid) escape fraction; inclusion of dust as an additional absorber of ionizing radiation. Bold entries refer to the fiducial configuration.

absorbed photons in a grid cell and frequency bin is then given by:

$$\Delta N_\nu = N_\nu(1 - \mathrm{e}^{-\tau_\nu}) \quad \text{with} \quad \tau_\nu = \sum_i \tau_{i,\nu}, \tag{4.3}$$

where N_ν is the number of photons in the frequency bin ν. Each time a photon packet crosses a gas cell the physical state of the gas in that cell is updated in terms of its temperature and ionization state (we refer the reader to the original papers for more details). This process is repeated until the photon packet leaves the simulated volume or, in the case of periodic boundary conditions, until the number of photons left in the packet drops below some threshold.

When taking into account dust absorption, the optical depth is further modified by the contribution of dust to the absorption cross section in the same fashion as for all other gas species. The crucial difference here however is that there is no tracking of the ionization state of the dust, i.e. the photons are simply absorbed by the dust without changing its physical properties.

4.2.3 Running CRASH on TNG50 galaxies

We first map the gas distribution of a given TNG50 halo onto a uniform grid. To do so, we derive an adaptive smoothing length for each Voronoi gas cell in the TNG50 simulation, equal to the radius of the sphere enclosing its 64 nearest neighbors.[2] We then distribute

[2]This neighbor choice is arbitrary and represents a reasonable compromise: a larger smoothing kernel would overall reduce gas clumping/inhomogeneities, while a smaller smoothing kernel would approach the discretness of natural Voronoi neighbors ($\sim 20 - 25$ on average), before introducing unwanted noise with even lower neighbor numbers.

the physical properties of each gas cell onto a regular Cartesian grid, where the deposition weighting uses the usual SPH cubic-spline kernel. The physical size of the grid is chosen such that each side has a length of twice the virial radius of the halo ($R_{\rm vir}$). The required size of the grid cells is determined by the minimum smoothing length of the particles to ensure that the resolution of our CRASH runs matches the resolution of TNG50. As the values for $x_{\rm HeII}$ and $x_{\rm HeIII}$ are not directly provided by the TNG snapshots, we calculate them for each cell based on collisional ionization equilibrium for a given gas temperature and density.

Note that we set star-forming gas cells from TNG to be initially neutral and to have a temperature of 1000K. This choice is consistent with the two-phase ISM model of the hydrodynamical simulations, where the dominant fraction (> 0.9) of gas mass is contained in the cold phase [190]. We discuss the change in the temperature state by the RT simulation in Appendix 4.4. Note that while the star forming cells in TNG are set to 1000K, during the gridding process the temperature of the voxels is usually given by a superposition of star-forming and non star-forming cells, which explains the range of temperatures seen in high density voxels after the gridding process (see fig. 4.16).

For the sources of radiation in the RT simulation we use the stellar particles from the TNG50 simulation, which are representations of stellar populations. To obtain the spectra and emissivites of these particles we use version 2.2.1 of the BPASS library [194, 48], based on the age, metallicity and initial mass of each stellar particle. There is no significant contribution of ionizing radiation emitted from AGN for galaxies within our examined mass range, and we omit any AGN contribution in our RT calculations.

The left panel of Figure 4.1 shows the number of halos selected for our analysis in each stellar mass bin, as well as the fraction of all TNG50 halos that we post-process. Thanks to the large parent volume, our sample provides ample statistics over the range of low-mass galaxies that are thought to be the primary drivers of cosmic hydrogen reionization.

The right panel of Figure 4.1 depicts the total ionizing emissivity of the halos post processed with the CRASH RT simulation as a function of their stellar mass. We find that the emissivities at a given stellar mass are similar for halos at all redshifts. There is however a slight increase in the average ionizing emissivity with increasing redshift. At a stellar mass of $\approx 10^7 M_\odot$ the average emissivity of halos at $z = 10$ is ~ 1.7 times higher than at $z = 6$. The reason is that, at a fixed galaxy mass, more star formation occurs at higher redshifts, with the average SFR being approximately twice as large at $z = 10$ than at $z = 6$ for halos in the same stellar mass bin.

We also see that the variation in the emissivities decreases with increasing stellar mass. The large variation and bimodality observed in the emissivity of lower mass halos is caused by low number statistics and stochasticity for stellar population particles (see also [22]). In addition, the ionizing emissivity is highly sensitive to the age of a stellar population, as most of this radiation is produced by short-lived O and B stars. This means that only very few stellar populations contribute significantly to the ionizing photon budget of small halos.

With the gas of the halo distributed on a regular grid, together with the radiation sources and their spectra, we then run the CRASH simulation. Our fiducial configuration

is shown in Table 4.1, together with several variations on both physical and numerical parameters which we also explore in this work. Each CRASH run extends for 5 Myr, a time span which guarantees that by the end of the simulation ionization equilibrium is achieved, although typically this is reached even earlier, within $\lesssim 1$ Myr. We use $N_p = 10^8$ for our studies to guarantee convergence (see Appendix 4.4 for a convergence analysis). Each packet is subdivided into 64 frequency bins sampling photon frequencies in the range $(13.6 - 161.9)$ eV, where the upper energy limit is chosen to capture helium ionization and explore the impact of higher energy photons emitted mainly by binary stars.

The full sample of halos summarized in Figure 4.1 is processed in our fiducial model in which we set the 'local' (i.e. unresolved) escape fraction $f_{\rm esc,loc}$ to unity, and do not include the absorption effects of dust. This choice for the local escape fraction was adopted as the simplest choice for a largely unconstrained parameter, and we discuss this value further in Section 4.3.3.

4.2.4 Photon Escape Fraction

Once the CRASH simulation is finished, we calculate the halo escape fraction of the halos. This is done by casting photon rays from each source in random directions and tracing them until they reach the virial radius, $R_{\rm vir}$, of the halo. The number of escaped photons in the frequency bin ν of one photon packet is given by

$$N_{\nu,\rm esc} = N_{\nu,\rm em} \times {\rm e}^{-\tau_{\nu,\rm tot}}, \tag{4.4}$$

where $N_{\nu,\rm em}$ is the number of emitted photons in a ray with frequency bin ν, and $\tau_{\nu,\rm tot}$ is the optical depth along the path of the ray, sampling each intersected gas cell using eqn. (4.2). For each stellar particle we initially cast 1000 rays. The total escape fraction from the halo is then be calculated as

$$f_{\rm esc} = \frac{\sum_{\rm source} \sum_{\rm packet} \sum_{\nu} N_{\nu,\rm esc}({\rm source, packet})}{\sum_{\rm source} \sum_{\rm packet} \sum_{\nu} N_{\nu,\rm em}({\rm source, packet})}. \tag{4.5}$$

We repeat the calculation of $f_{\rm esc}$ until we reach convergence to better than an relative tolerance of 0.01 [3].

4.3 Results

4.3.1 Halo Escape Fraction

We begin with our main result. Figure 4.2 shows the escape fraction of ionizing photons as a function stellar mass (left) and total halo mass (right). This is the halo-scale escape fraction, and overall we observe a large scatter at all redshifts and masses, with the variation

[3] We verified the accuracy of the algorithm by calculating the escape fraction using different random seeds for the Monte Carlo sampling of the rays.

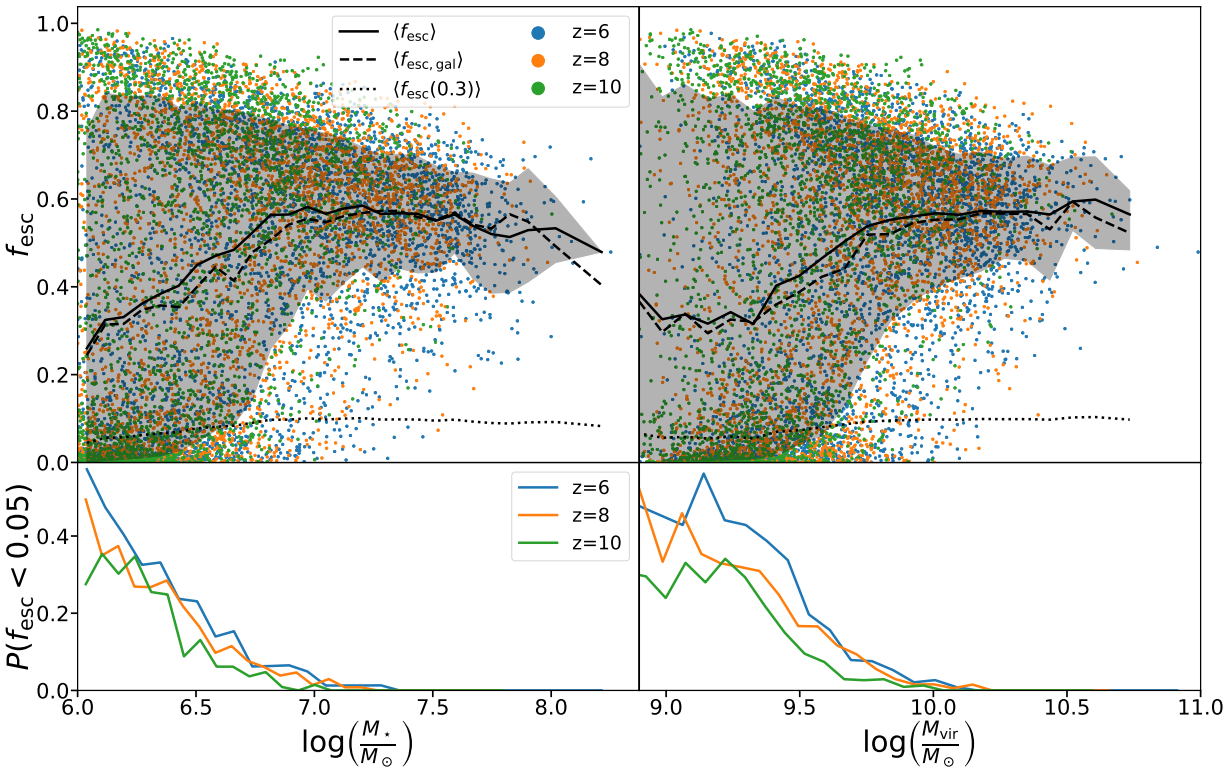

Figure 4.2: *Top panels:* The escape fraction of ionizing radiation as a function of galaxy stellar mass (left panels) and total halo mass (right panels) at redshifts $z = 6$ (blue), $z = 8$ (orange) and $z = 10$ (green), as predicted by our TNG50 post processing with CRASH. The solid and dashed lines refer to the average halo ($R_{\rm vir}$) and galactic ($0.2R_{\rm vir}$) escape fractions, which increase with mass from $\sim$ 0.3 at $M_\star \sim 10^6\,{\rm M}_\odot$ to a maximum of $\sim$ 0.6 at $M_\star \sim 10^8\,{\rm M}_\odot$, after which there is a hint of a turnover and a decrease of escape fractions for even more massive galaxies. The dotted line shows our results rescaled to $f_{\rm esc,loc} = 0.3$, instead of our fiducial choice of unity, resulting in significantly lower escape fractions (see text). Shaded areas represent the interval containing 68% of all halos. *Bottom panels*: The fraction of halos with an negligible escape fraction (below 10^{-2}), as a function of mass. The abundance of such non-contributing galaxies rises rapidly towards the lowest masses considered in our study, due to the significant stochasticity in the stellar populations of low-mass galaxies.

increasing for lower mass galaxies. This scatter is largely driven by the stochasticity of small stellar populations within the lower mass halos. In such halos, in fact, $f_{\rm esc}$ can be dominated by the escape fraction of a handful of star particles, which in turn strongly depends on the age of the population. Indeed, young stellar populations produce significant amounts of ionizing radiation, and as the cores of smaller halos are less dense, a young stellar population is usually able to ionize its surrounding.

In larger halos, instead, the escape fraction is more strongly dominated by the global properties of the halos, as random fluctuations in the escape fraction of individual stellar particles are averaged out by having a sufficiently large sample. As a result, the distribution of the escape fraction becomes bimodal at small masses, where a large number of halos have high escape fractions, while a significant fraction also have $f_{\rm esc} < 1\%$ and therefore do not contribute significantly to the ionizing photon budget escaping into the IGM. As these halos are difficult to distinguish in the top panel, we plot the fraction of halos with $f_{\rm esc} < 1\%$ in the lower panel. Indeed, the fraction of halos with $f_{\rm esc} < 1\%$ is $\approx 30\%$ for small mass halos, while it becomes negligible for halos with stellar masses $\gtrsim 10^{6.5} M_{\odot}$.

The average escape fraction, $\langle f_{\rm esc} \rangle$, calculated by combining all redshifts, initially increases with increasing mass. It then flattens at $M_{\star} = 10^{7} M_{\odot}$and for $M_{\star} \gtrsim 10^{8} M_{\odot}$there is an indication that the escape fraction begins again to decrease, although here our sample of RT-processed halos is small. The same trend is observed at each individual redshift, where the average escape fraction slightly decreases with decreasing redshift (see Figure 4.3).

In contrast to the total escape fraction (solid lines), the galactic escape fraction $\langle f_{\rm esc,gal} \rangle$ (dashed lines) is defined as the relative amount of photons that escapes a sphere of radius $R_{\rm gal} = 0.2 R_{\rm vir}$, representing an approximate boundary between the galaxy and its circumgalactic medium [147]. Although the evolution of $\langle f_{\rm esc,gal} \rangle$ is similar to that of $\langle f_{\rm esc} \rangle$, its value is on average slightly lower. This occurs because stellar particles located outside $R_{\rm gal}$ are embedded in a less dense environment, which in turn facilitates the escape of ionizing photons.

In addition to this fiducial result, we have also included the escape fraction we would have obtained with a sub-grid local escape fraction of $f_{\rm esc,loc} = 0.3$ (dotted lines), as this value leads to results which are in better agreement with observational constraints on global emissivities. The range between these lines represents an element of systematic uncertainty on the emergent escape fractions from the cosmological simulation, and this range is significant. We further discuss the important role of $f_{\rm esc,loc}$ in Section 4.3.3.

In Figure 4.3 we compare our results against other simulation-based inferences. We show escape fraction as a function of stellar mass (left) and halo mass (right), across the redshift range of reionization (as indicated by the colors). The previous studies with published results we compare against are: the FIRE-II simulation [125], the CoDa-II simulation [118], the RAMSES simulations by [106], the THESAN simulation [218], and the SPHINX simulation [176]. Note that most simulations adopt different values for the subgrid escape fraction. Furthermore, some show the average value, while others the median. These can explain some, but certainly not all of the variation observed.

Broadly speaking, predictions for the escape fraction of ionizing radiation during reion-

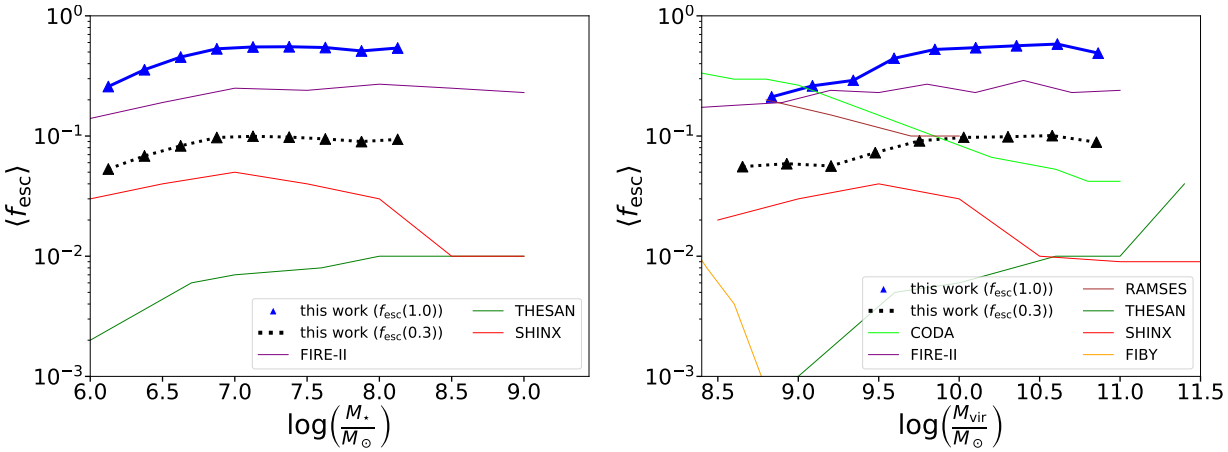

Figure 4.3: Comparison of escape fractions at redshift 6 between different simulations, as a function of galaxy stellar mass (left) and halo mass (right). We contrast our TNG50+CRASH RT simulations (this work, $f_{\rm esc} = 1.0$, thick line with large triangles), as well as our result rescaled to $f_{\rm esc,loc} = 0.3$ (dotted black line with large black triangles), with results from FIRE-II with halos across $z = 5 - 12$ [125], the Cosmic Dawn II simulation [118], the THESAN simulation [218], the RAMSES simulation by [106], as well as the SPHINX simulation of [176]. Note that different calculations have adopted different sub-grid escape fractions. The THESAN simulations assume a value of $f_{\rm esc,loc} = 0.37$, the CoDa-II uses $f_{\rm esc,loc} = 0.42$, while the others all assume $f_{\rm esc,loc} = 1$. Furthermore, the THESAN and RAMSES lines represent the median values of the escape fraction, the other lines the mean. For the SPHINX simulation the mean is luminosity weighted. There is significant diversity in the results, and predictions for the escape fraction of ionizing radiation vary by at least an order of magnitude, at any given mass, between different simulations.

ization span an enormous range. Between different simulations, $f_{\rm esc}$ easily varies by an order of magnitude, at fixed mass. There is clearly no theoretical consensus on the average value of this parameter, nor its detailed relationship with galaxy mass, halo mass, or redshift.

The qualitative trends of our $f_{\rm esc}$ (discussed above) agree well with those from the FIRE-II simulations (black crosses), which adopt the same approach to the problem, i.e. the radiative transfer is based on Monte Carlo post-processing. On the other hand, the normalization of our fiducial results is higher possibly due to the different resolution of the simulations. Furthermore, TNG and FIRE-II use a different ISM models, which affects the resulting gas distribution in the galaxy, and thus the escape fraction. Finally, unlikely our approach, the RT post-processing of the FIRE-II galaxies does not change the thermal state of the gas, which might result in differences in the recombination rates.

A more realistic value of $f_{\rm esc,loc}$ results in a reduction of $f_{\rm esc}$ (see Figure 4.7), as can be seen from the dotted line in the figure, which shows the average escape fraction rescaled to the value it would have with a sub-grid local escape fraction of $f_{\rm esc,loc} = 0.3$.

The CoDa-II RHD simulations [118] show a stronger dependence on the halo mass (squares), where the trend at the high-mass end is sensitive to redshift. The direction of the correlation with mass is qualitatively inconsistent with our results in the overlapping mass range, although the actual magnitude of $f_{\rm esc}$ is similar. The SPHINX results [176] exhibit qualitatively similar trends as our TNG50 results, albeit at a normalization slightly below our $f_{\rm esc,loc} = 0.3$ case. The [106] simulations (stars) have qualitatively similar results as this work, bracketed by the two cases shown, albeit over a limited mass range.

The most compelling comparison is with the escape fractions predicted by THESAN [218], which are by and large much lower than ours, with typical values of order $\sim$ 1%, with mass trends which are either flat, slightly increasing, or slightly decreasing, depending on redshift. That work finds a clear signature of decreasing $f_{\rm esc}$ at the high-mass end, for $M_\star \gtrsim 10^{8.5}\,{\rm M}_\odot$, where our current sample runs out of statistics.

The level of disagreement with THESAN is notable because it is based on the same IllustrisTNG galaxy formation model, essentially unchanged from its fiducial incarnation in TNG50, as we analyze here, except for the addition of on-the-fly radiative transfer and non-equilibrium thermochemistry [101]. In THESAN, a non-trivial complexity therefore arises in how radiation interacts with star-forming gas [185], influencing its phase distribution [63]. We remind the reader that in the TNG model this gas has its thermal state set by a sub-grid, two-phase model for pressurization of the ISM by unresolved stellar feedback processes [190]. Because the effective temperature is high, dense ISM gas is effectively ionized, and the escape fraction from the (resolved) ISM in THESAN is therefore unity. Different choices in the coupling of the RT with the sub-grid ISM model could change these results, and our comparison. The on-the-fly RT treatment in THESAN is clearly a key strength, and captures the dynamic impact and back-reaction on the gas, which we miss in TNG50. However, our post-processing approach also enables a more accurate (and expensive) Monte Carlo RT solution. Finally, the hydrodynamical resolution of TNG50 is higher than THESAN – 6.8 times better in baryonic mass resolution, and this could also play a role in resolving small-scale structure in the ISM. A full understanding of the

predictions for escape fractions in the TNG galaxy formation model will benefit from a future, apples-to-apples comparison between our current results and those from THESAN.

With respect to redshift trends, we find that the average $f_{\rm esc}$ decreases with decreasing redshift, although the trend is weak, from a few percent to perhaps ten percent from $z = 10$ to $z = 6$. We note that this correlation with redshift is expected for models which produce enough photons to sustain the reionization process [60, 168]. The CoDa-II and [106] simulations show the opposite trend, while the FiBY simulation finds no strong dependence, and THESAN suggests a non-monotonic behavior.

Although it is difficult to ascertain the reasons for such discrepancies, we note that the escape fraction is strongly dependent on the small scale density distribution, and clumpiness of gas in the ISM [176], and hence on simulation resolution, which varies (substantially) between all the above studies. Additional causes are the different numerical and physical models used in the simulations, which greatly affect the distribution of stellar populations as well as the rate of star formation, resulting in vastly different modes of photon escape. Furthermore, the IMF used to sample the stellar populations, as well as the inclusion of binary systems, changes the amount of ionizing photons produced. We try to address some of these caveats by investigating the effects that the unresolved small scale distribution of the ISM has on $f_{\rm esc}$ by varying the local escape fraction (see Figure 4.7), we assume that its value is universal and constant: independent of halo mass and redshift, for example. Such dependencies could change the behaviour of $f_{\rm esc}$, in particular for larger halos, as we discuss in Section 4.3.3.

In Figure 4.4 we go deeper into the gas physics relevant for the escape fraction calculation, visualizing two representative $z = 8$ halos with similar mass, but with very different $f_{\rm esc}$. Indeed, the halos in the left and right panels have a mass of $M_{\rm vir} = 5.5 \times 10^9 M_\odot$and $8.2 \times 10^9 M_\odot$, respectively, while their escape fractions are 76.5% and 3.6%, respectively. As a result, these two halos fall at the upper and lower end of the scatter in $f_{\rm esc}$ for their mass. While similar in their stellar mass and SFR, the main difference between them is that the halo with the lower escape fraction has a gas mass which is almost two times larger. Hence, in this case, the difference in the escape fractions is mainly driven by more gas absorption taking place in the first halo.

We create two-dimensional projections of gas temperature, T, the gas number density, $n_{\rm gas}$, the fractions of HII, $\mathrm{x_{HII}}$, HeII, $x_{\rm HeII}$, and HeIII, $x_{\rm HeIII}$, and the stellar particle emissivity, $Q_{\rm sources}$. In both halos we see that the central gas cloud, at high density, remains cold and mostly neutral. At larger distance, the right-side halo exhibits neutral gas in appreciable quantities along overdense filaments and extended structures. In contrast, the left-side halo is comprised of fully ionized hydrogen, with the exception of a few localized clouds of gas which manage to remain mostly neutral.

As expected, the vast majority of ionizing sources are located in the center of the halo, where the central galaxy is found. The halo on the left has an ionization rate of 6×10^{52} s^{-1}, while the one on the right of 2×10^{51} s^{-1}. This difference in ionizing photon production rate, i.e. the scatter of stellar population properties at a given halo mass, is the key driver of the scatter in escape fraction.

In addition, we see that in the left-hand side halo the overall source distribution is

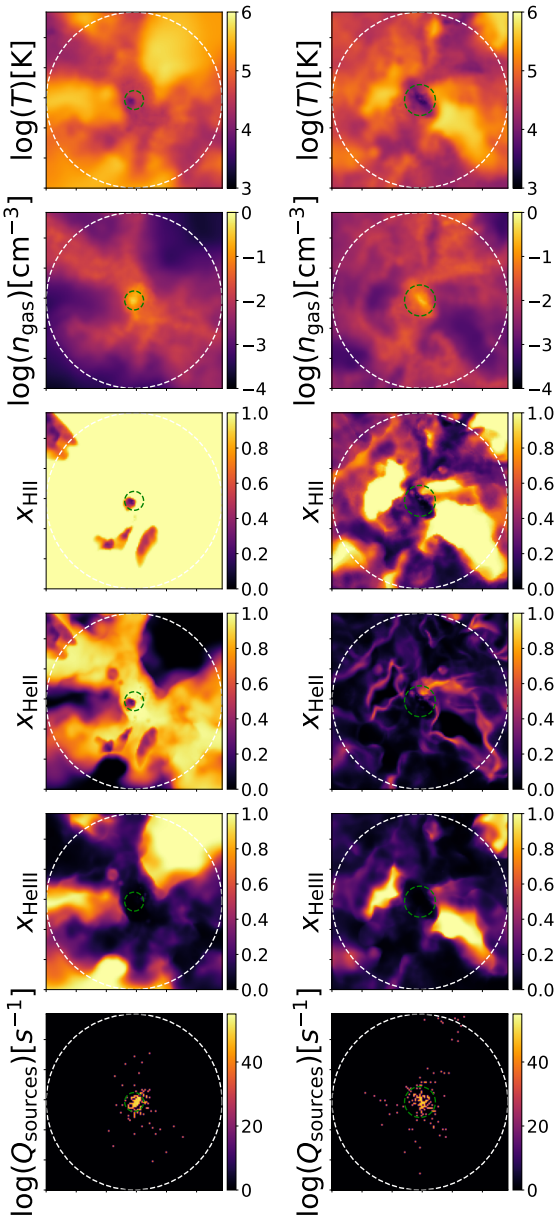

Figure 4.4: Two similar mass halos with different escape fractions. From top to bottom, the panels show 2D projections of temperature, gas number density, HII, HeII and HeIII fractions and stellar particle emissivity after the RT simulation run. The left (right) panels correspond to a $z = 8$ halo with mass $M_{\rm vir} = 5.5 \times 10^9 M_\odot (8.2 \times 10^9 M_\odot)$, and $f_{\rm esc} = 76.5\%$ (3.6%). The white and green circles indicate the virial radius of the halo, and the radius encompassing 50% of the total stellar particle emissivity, respectively. The temperature and the ionization states are density weighted in projection.

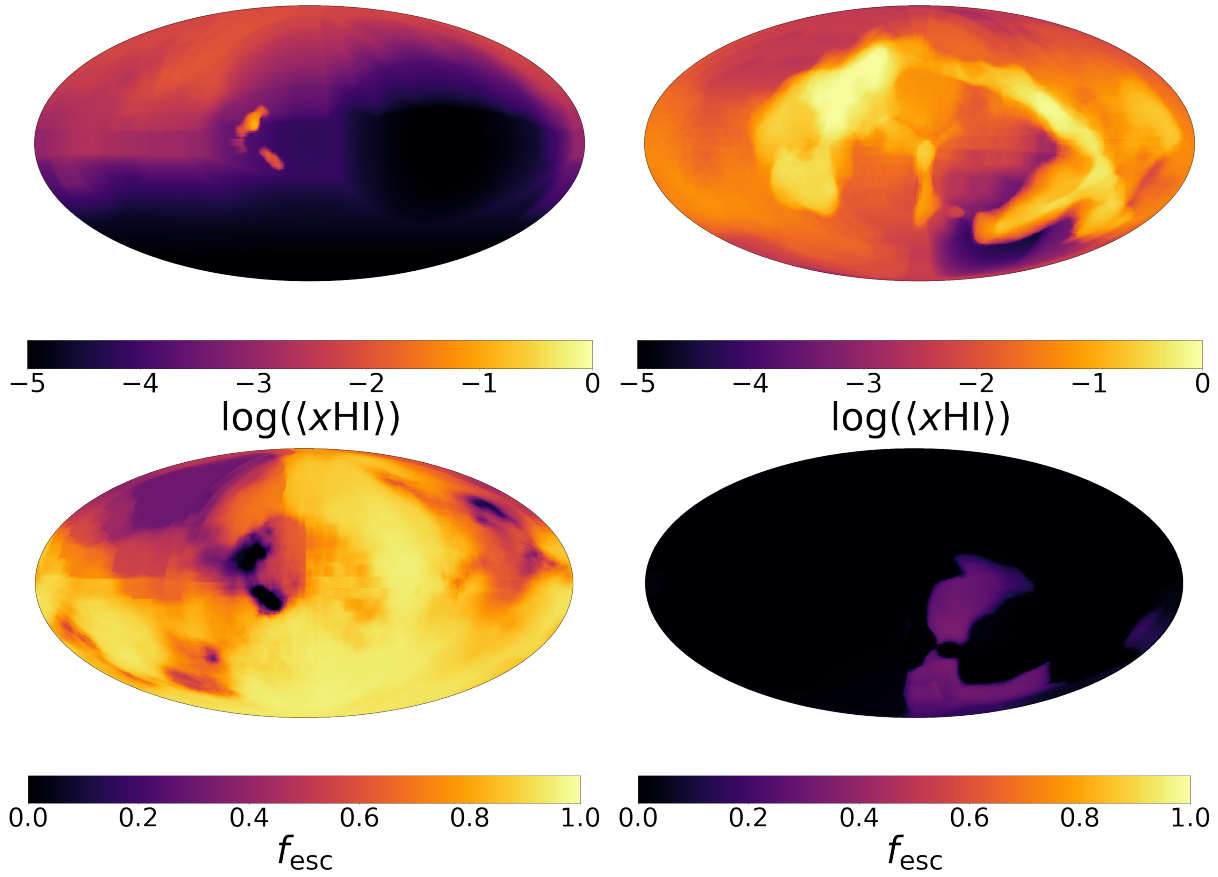

Figure 4.5: Mollweide all-sky projections of the same two halos presented in Figure 4.4. *Top:* Average neutral hydrogen fraction along radial lines of sight from the halo center to a sphere at the virial radius. *Bottom*: Emissivity weighted escape fraction of all sources at the virial radius of the halo, i.e. the fraction of photons emitted from all sources in a given direction which reach the virial radius of the halo.

somewhat displaced (to the right) with respect to the central overdense region, in the right-hand side halo they are mostly aligned with the halo center. In the former case, the radiation can ionize the surrounding gas more easily than in the latter, an effect which can be seen in the x_{HII} maps.

In the left-hand side halo the sources are also able to ionize the surrounding HeI. However, in both halos x_{HeIII} is negligible in the central region and the only HeIII present is due to ionization from shocks. We therefore expect that the higher energy tail of the radiation emitted by the sources will be absorbed more in comparison to the less energetic photons (see discussion in Section 4.3.6).

In Figure 4.5 we investigate in more detail the spatial dependence of the escape fraction in the same two example halos. Here we show the average neutral fraction of hydrogen (top), together with the corresponding average emissivity weighted escape fraction (bottom), along radial lines of sight from the halo center to the virial radius. As expected,

there is an anti-correlation between the escape and average $x_{\rm HI}$, with photons preferentially escaping through channels of circumgalactic gas which are highly ionized.

In the halo on the left ($f_{\rm esc} = 76.5\%$) photons are able to escape through most of the virial surface of the halo, the only exception being small regions of solid angle with residual dense and neutral gas at the center and in the top-left corner, also visible in Figure 4.4. In the halo on the right ($f_{\rm esc} = 3.5\%$) only a relatively small area in the bottom-right part of the image has a significant escape fraction, corresponding to channels of the most ionized gas, visible in the top panel as well as in Figure 4.4. The escape fraction through this channel, though, is fairly low ($\approx 30\%$) since a significant fraction of the stellar particles are located outside of it, such that ionizing photons emitted from these particles are largely absorbed.

The escape of ionizing radiation depends strongly on direction.

4.3.2 Dependence on galaxy and halo properties

In order to explore the variation of $f_{\rm esc}$, we study its dependence on a number of properties of both the central galaxy and its parent dark matter halo. We note that the phrases 'within the galaxy/galactic' or 'halo' refer to the collection of gas cells or particles residing within $R_{\rm gal} = 0.2R_{\rm vir}$ or $R_{\rm vir}$, respectively. All properties are calculated directly from the CRASH grids, to guarantee they are consistent with the RT inputs. Finally, as these dependences of $f_{\rm esc}$ on different properties have little redshift dependence, we combine all halos across redshifts in the following analysis.

In Figure 4.6 we show eight panels, each visualizing the plane of escape fraction versus stellar mass. In each case, we color bins by the median value of a third physical property, as indicated by the colorbars and labels. In addition, we normalize these physical values by their median at each given stellar mass bin, making the color scales relative (i.e. conditional) to the typical property of galaxies or halos at that mass. To represent the actual density of objects in this plane, we use the solid and dashed contours to demarcate the 1σ and 2σ regions of galaxy occupation.

Gas surface density

First we examine the effect of galactic gas surface density, defined as

$$\Sigma_{\rm gas,gal} = M_{\rm gas,gal} / \left(\pi R_{\rm gal}^2\right), \tag{4.6}$$

where $M_{\rm gas,gal}$ is the gas mass within the galactic radius $R_{\rm gal}$ (top left panel). We observe two effects in the escape fraction due to variation in $\Sigma_{\rm gas,gal}$. First, higher gas surface density leads to a higher SFR and hence more stars which can ionize the surrounding medium and create channels for ionizing radiation to escape. On the other hand, higher gas surface density also implies that the medium is more opaque, making it more difficult to ionize. We find that the second effect dominates, as the escape fraction negatively correlates with the surface density of the gas. For example, at $M_\star = 10^7\,{\rm M}_\odot$, the escape fraction decreases from ~ 0.8 to ~ 0.6 as the gas surface density increases by a factor of

two. At the same time, outliers with low $f_{\rm esc} \lesssim 0.4$ at this mass scale exhibit similarly low gas surface densities as the highest escape fraction galaxies. Such a non-monotonic trend is visible at intermediate galaxy masses.

Stellar surface density

We calculate the mass surface density of stars $\Sigma_{\star,\rm gal}$ within the galaxy analogously as above, replacing gas mass with stellar mass. The top right panel of Figure 4.6 is noisy, but broadly speaking we see a negative correlation for halos with $M_\star > 10^{7.5}\mathrm{M}_\odot$, and a positive/non-monotonic trend at lower masses. Indeed, the correlation of $f_{\rm esc}$ with stellar surface density at fixed mass is qualitatively similar, but inverted, with respect to the correlation with gas surface density. At intermediate masses, galaxies with both the lowest and highest escape fractions have relatively low $\Sigma_{\star,\rm gal}$, while those with average escape fractions have lower stellar surface densities.

We suggest that lower mass halos have less dense centers, such that young stellar particles are usually able to ionize their environment. Therefore, the escape fraction is mostly determined by the number of stars contributing to the ionization of the whole halo. The negative correlation for halos with a higher stellar mass, instead, may be due to the association of higher stellar surface density with higher gas density, so that stars are unable to fully ionize their immediate surrounding. As a result, a higher number of stars would not necessarily result in a stronger ionization of the halo.

Ionizing emissivity

There is a clear and unambiguous positive correlation between escape fraction and the total ionizing emissivity of the halo, Q_0, particularly for lower mass halos. The large scatter of $f_{\rm esc}$ at $M_\star < 10^7\,\mathrm{M}_\odot$ is due to variation in Q_0 - those galaxies with low to zero escape fraction have substantially lower total ionizing emissivities, by more than a factor of four (where we saturate the relative color range). At these low masses, the escape fraction is often dominated by a few young stellar populations, and the location of these sources with respect to the underlying gas distribution in the galaxy and halo is key. Depending on their position within the halo, these can either fully ionize the surrounding medium, or barely ionize it at all.

At the high-mass end of our study, $10^{7.5} < M_\star/\mathrm{M}_\odot < 10^8$, the correlation of escape fraction with total ionizing emissivity has the same sign, although it is weaker. In particular, high $f_{\rm esc}$ galaxies are always those with larger Q_0, as expected.

Halo virial radius

At fixed stellar mass, galaxies can reside in dark matter halos of varying total mass, and thus size. To explore this, we examine the correlation with the virial radius of the parent halo. As with gas surface mass density, we find that galaxies with typical $f_{\rm esc}$ values sit in halos with typical (median) virial radii, whereas outliers in escape fraction, either high or

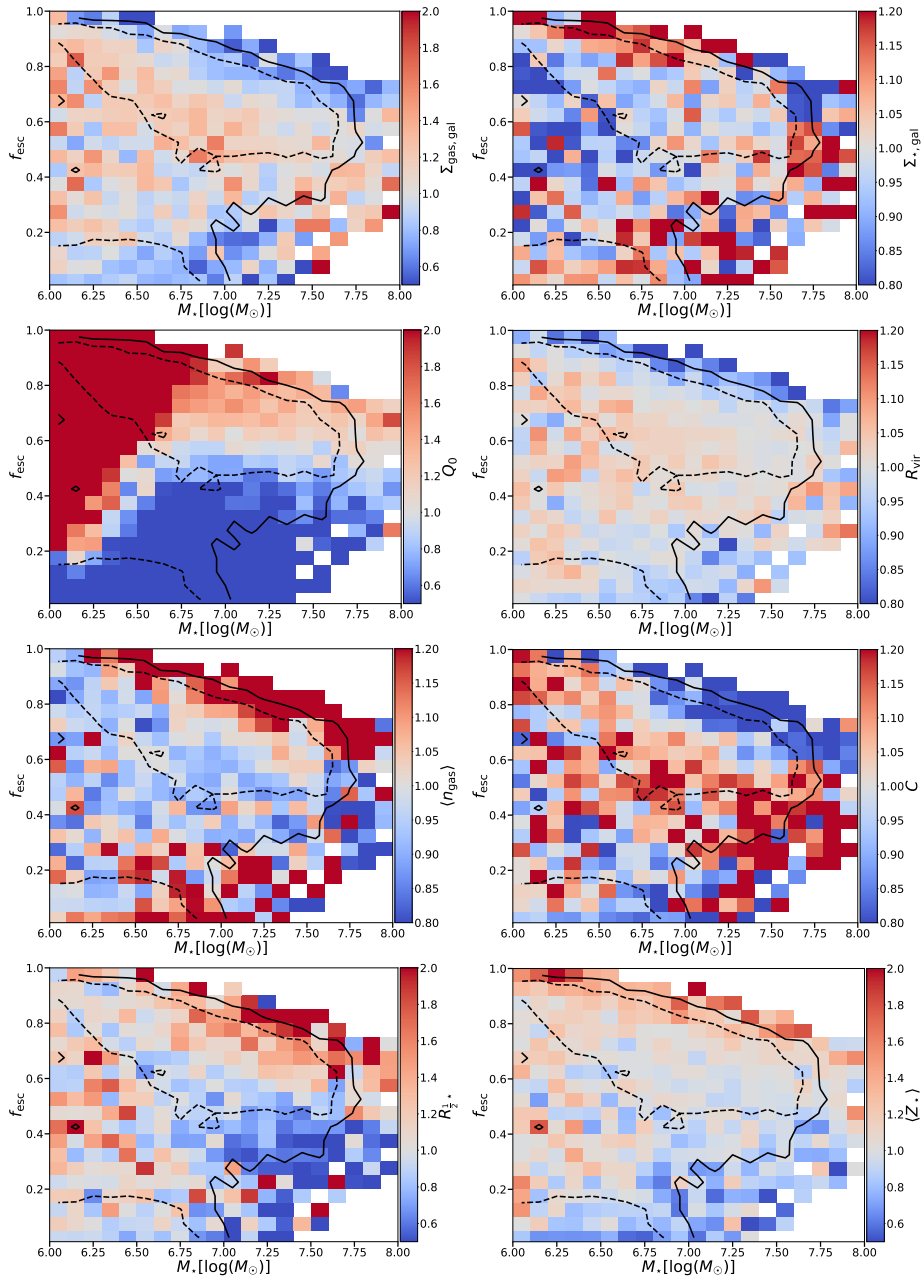

Figure 4.6: Ionizing escape fraction f_{esc} as a function of stellar mass for halos, combining $6 < z < 10$. In the eight panels, each colorbar and label refers to one of eight different physical properties. In each case, the color of every bin represents the median value of that quantity for all galaxies in that bin, normalized to the median value in that 0.1 dex stellar mass bin. That is, blue shows values lower than typical at that mass, while red shows values higher. From left to right, top to bottom, the properties are: gas surface density $\Sigma_{gas,gal}$, galactic stellar surface density $\Sigma_{\star,gal}$, halo's ionizing emissivity Q_0, virial radius of the halo R_{vir}, average number density $\langle n_{gas} \rangle$, halo clumping factor C, radius at which half the stellar emissivity of the halo is reached $R_{1/2,\star}$, and emissivity-weighted stellar metallicity $\langle Z_\star \rangle$. The solid and dashed lines represent the 1σ and 2σ contours of the number of galaxies in this plane.

low, tend to sit in smaller (more compact) halos. This trend is most visible at intermediate stellar masses, and is negligible at both the low-mass and high-mass ends of our sample.

Together with the observed correlation with gas surface density, this result suggests that more compact halos hosting less compact galaxies tend to have the highest escape fractions.

Average gas density

The propagation of ionizing radiation is strongly impacted by the surrounding gas density structure. To zeroth order, we therefore examine the connection between escape fraction and the average gas number density of the halo $\langle n_{\rm gas} \rangle$. We again observe a characteristic non-monontonic correlation whereby galaxies at typical values of $f_{\rm esc} \sim 0.6$ have the lowest average gas densities, whereas outliers both high and low reside in denser halos.

This effect is qualitatively similar to that observed for stellar surface density, but even more clear and pronounced. If the overall gas density in the halo is higher than is typical at a given mass, then the escape fraction can be driven either low (for low total emissivity), or high (for high total emissivity); in both cases the stellar source distribution is also (overly) compact.

Halo gas clumping factor

The gas density field encountered by propagating photons is not smooth. We therefore define and measure the gas clumping factor as

$$C = \langle n_{\rm gas}^2 \rangle_V / \langle n_{\rm gas} \rangle_V^2, \tag{4.7}$$

where the average of gas number density is taken over the volume V of the halo. Overall, we see that escape fraction negatively correlates with clumping. Since the recombination rate scales as density squared, a stronger clumping facilitates more recombinations, making it more difficult for photons to create an ionized escape channel. On the other hand, stronger clumping also means that the gas distribution is more localized and less homogeneously distributed, which could lead to more underdense regions and facilitate the creation of ionized channels, increasing the escape fraction.

However, the latter effect seems to be subdominant. This roughly agrees with [82] and FiBY, which found a strong correlation between escape fraction and clumping for only very low values of clumping, while we see that relatively small variations in C significantly change $f_{\rm esc}$. Higher resolution simulations could potentially lead to a different result, as clumping on smaller scales leads to the formation of more clustered star formation and so coherent emission of ionizing radiation [31].

Stellar half emissivity radius

The galaxy stellar 'size', emissivity weighted, is calculated as the stellar half emissivity radius (lower left panel). Above a stellar mass of $M_\star \gtrsim 10^{6.5}\,{\rm M}_\odot$ we find a clear, positive

correlation, such that galaxies with more extended stellar source distributions have higher escape fractions. This connection is reassuring and as expected: when stellar populations are less centrally concentrated, they are less surrounded by the densest gas at the center of the halo, facilitating the ionization of the halo gas and higher $f_{\rm esc}$.

Emissivity weighted stellar metallicity

Finally, we find a clear positive correlation between the emissivity-weighted stellar metallicity and the escape fraction (lower right panel). As higher metallicity stars have longer lifetimes, this increases the time where such stellar populations have the chance to leave their initial birth clouds while still young enough to produce significant amounts of ionizing radiation.

In addition to the quantities explored here, we also considered halo metallicity, the gas fraction of the halo, total halo mass itself, the galaxy SFR as well as the emissivity weighted age of the stellar populations (not shown). In these cases any trends with escape fraction are weak and tentative at best. Although a correlation with SFR would be expected, we suspect that the instantaneous values of SFR we use, which oscillate on short timescales, are not sufficiently connected to the ionization state of the gas. Short time-scale variation of SFR, over different time periods, is expected to be connected to highly time variable $f_{\rm esc}$ [176].

4.3.3 Impact of the local escape fraction

In all numerical hydrodynamical simulations with finite resolution, small-scale gas structure will be resolved down to some scale, but unresolved for smaller scales. Although the resolution of TNG50 is comparably high, achieving gas cell sizes of order a few physical parcsecs at these redshifts, it does not well resolve parsec-scale ISM structure. In particular, due to resolution limits pressure support of the star forming gas due to feedback at small scales is not modelled explicitly but relies on sub-grid pressure support [190]. Additionally, the sub-grid escape fraction is likely to be affected by the gas being either in a clumpy cold state or in a diffuse hot state in a given star forming cell, which is not modelled explicitly in our framework. Therefore, gas at these scales would realistically impact the small-scale escape of ionizing radiation [35, 90, 104, 105, 83]. As a result, some simulations adopt a sub-grid escape fraction, also referred to as a local escape fraction, or unresolved escape fraction. This value accounts for photon absorption on subgrid scale, i.e. the fraction of ionizing photons that escape their cell of origin.

In many RHD simulations of reionization, this $f_{\rm esc,loc}$ parameter is taken to be unity, which assumes that there is no unresolved gas density structure of relevance. The validity of such a choice depends sensitively on the numerical resolution of the underlying simulation.

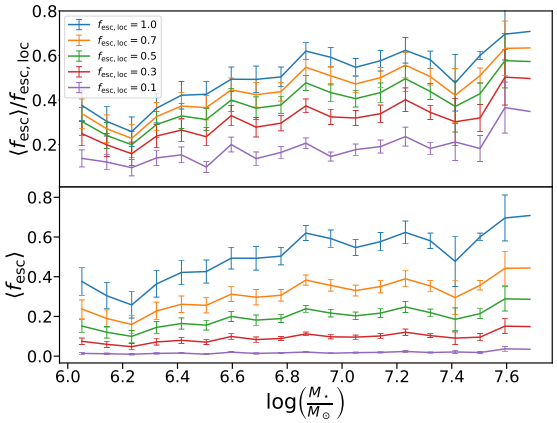

Figure 4.7: *Top:* Average halo escape fraction of ionizing photons as a function of stellar mass for different values of local escape fraction, $f_{\rm esc,loc}$, as indicated by the colors. The error bars show the standard deviation on the mean in each mass bin, and here we combine halos at all three examined redshifts. *Bottom:* Average total escape fraction, obtained multiplying the halo escape fraction from the top panel by the corresponding local escape fraction. Measured values of $f_{\rm esc}$ depend sensitively, and non-linearly, on the value of the local escape fraction assumed.

For our fiducial results, we have also adopted $f_{\rm esc,loc} = 1$, as the simplest possible choice. We now test the validity and impact of this assumption for the specific case of TNG50.

To do so, we have repeated our RT calculations adopting different values of $f_{\rm esc,loc}$, and Figure 4.7 shows the result. In the top panel we show the average escape fraction obtained with different assumptions for $f_{\rm esc,loc}$, from a value of 10% to the fiducial case of 100%. As expected, a higher $f_{\rm esc,loc}$ results in a higher fraction of photons which can escape the halo, as the larger production rate of ionizing photons ionizes more of the halo gas. There is an increase of $5-10\%$ in the escape fraction for every 20% increase in the local escape fraction, with the exception of $f_{\rm esc,loc} = 0.1$ where the difference is in the range of $10-15\%$. This effect is more strongly seen for more massive halos, while for halos with a stellar mass of $M_\star < 10^{6.5}$ $\rm M_\odot$ the variation is smaller. For the smallest local escape fraction of $f_{\rm esc,loc} = 0.1$ there is almost no evolution in the halo escape fraction with stellar mass.

There is a clear, non-linear dependence of $f_{\rm esc}$ on the value of the local escape fraction, and thus the global escape fraction cannot be simply obtained by re-scaling. Instead, separate RT simulations must be run for different values of $f_{\rm esc,loc}$.

In any of the cases with $f_{\rm esc,loc} < 1$, the halo escape fraction, i.e. the ratio of emitted photons to halo escaping photons, is given by the multiplication of the local escape fraction parameter with the measured fraction, as described above. The bottom panel of Figure 4.7 shows these values, appropriate for comparison with observationally inferred escape fractions or for inclusion into large-scale models where the entire process of photon escape is unresolved.

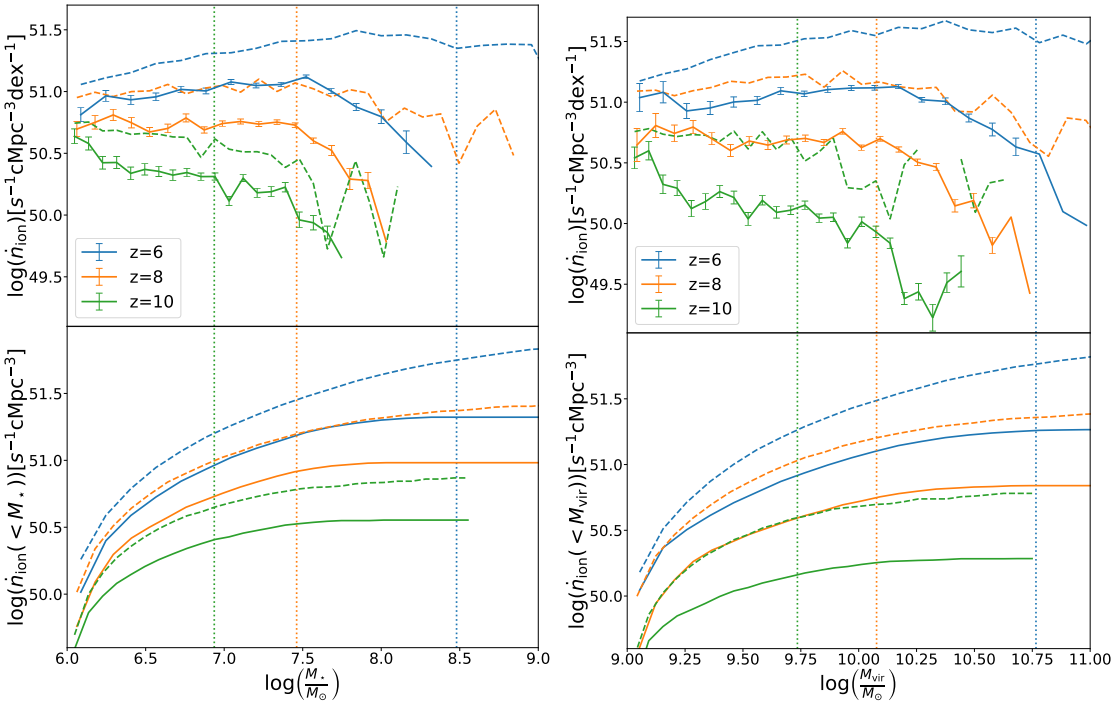

Figure 4.8: *Left:* Global ionizing photon emissivity (top panel) and cumulative emissivity (bottom) as a function of the stellar mass for halos at $z = 6$ (blue lines), $z = 8$ (orange) and $z = 10$ (green) as predicted by our TNG50+CRASH RT simulations. The error bars in the top panel represent the propagated error of the escape fraction. Depicted with the dashed lines are the intrinsic emissivity densities, i.e. the emissivity densities derived from all stellar populations associated with a halo. The vertical dotted lines refer to the stellar mass at which half the intrinsic emissiviy is reached at a given redshift. *Right:* The same quantities, shown as a function of total halo mass instead of galaxy stellar mass. Galaxies with a stellar mass of $M_\star < 10^{7.5}\mathrm{M}_\odot$ (halos with $M_{\rm vir} < 10^{10}\mathrm{M}_\odot$) contribute the bulk of the ionizing photons at all redshifts.

4.3.4 Density of ionizing photon escape

In Figure 4.8 we investigate the contribution of halos of different mass to the total production of ionizing photons. To calculate the emissivity, $\dot{N}_{\rm ion}$, we weight the average number of ionizing photons escaping from objects in a given mass bin with the density of halos within the same bin, obtained from the halo abundance in the TNG50 catalog. Throughout this study we use the results of our fiducial run, i.e. $f_{\rm esc,loc} = 1$. We also depict the intrinsic ionizing emissivity density, i.e. prior to absorption. For the intrinsic emissivity we also use a lower cut-off stellar mass $M_{\star,\rm min} = 10^6 M_\odot$.

Halos with a stellar mass of $M_\star < 10^{7.5}\mathrm{M}_\odot$ ($M_{\rm vir} < 10^{10}\mathrm{M}_\odot$) contribute the largest number of escaped ionizing photons at all redshifts. While the maximum of the emissivity at $z = 10$ corresponds to $M_\star < 10^6\mathrm{M}_\odot$ ($M_{\rm vir} < 10^9\mathrm{M}_\odot$), such halos are not included in this study as they are not well resolved. Therefore, the budget of ionizing photons presented

here could be seen as a lower limit at $z \gtrsim 10$. Our upper mass cutoff, instead, excludes the heaviest halos, but these are contributing fewer and fewer ionizing photons, making them relatively unimportant. Specifically, at $z = 8$ and $z = 10$ we already see a strong decrease of the escaped emissivity density at these masses. A similar but less pronounced behaviour is in place also at $z = 6$, although a larger sample of RT-processed halos at these times would be useful to confirm the trend.

At $z = 6$ and $z = 8$, the escaped emissivity curves are almost flat over about an order of magnitude in mass. At $M_\star \sim 10^6 \mathrm{M}_\odot$ ($M_{\mathrm{vir}} \sim 10^9 \mathrm{M}_\odot$) the emissivity at different redshifts does not vary significantly, while it declines with increasing mass for all redshifts. Since the escape fraction is not strongly dependent on redshift, the difference in emissivity can be mostly attributed to the lower abundance of massive halos at higher redshifts. As the abundance of higher mass halos increases, reionization will be progressively more driven by such halos.

In the bottom panels of Figure 4.8 we plot the cumulative emissivity. As before, we observe a rapid rise in the range $M_\star \sim 10^6 - 10^7 \mathrm{M}_\odot$ ($M_{\mathrm{vir}} \sim 10^9 - 10^{10} \mathrm{M}_\odot$) for all redshifts, while at higher masses the emissivity begins to saturate. Halos with a stellar mass of $M_\star \gtrsim 10^7 \mathrm{M}_\odot$ ($M_{\mathrm{vir}} \gtrsim 10^{10} \mathrm{M}_\odot$) do not significantly contribute to the budget of ionizing radiation at high redshifts.

In Figure 4.9 we compare the emissivities obtained with our model to observational constrains from [16] and [133], in addition to the results of [195], [170], and [18] as presented in [15] with the assumption of a constant $f_{\mathrm{esc}} = 0.2$. This is a comparison at face value, i.e. we have not replicated the selection functions of the observed data nor the measurements via e.g. forward modeling, and therefore intent only a qualitative assessment.

We find that while our prediction with $f_{\mathrm{esc,loc}} = 1.0$ lies above most observational constraints, and is thus at face-value disfavored, adopting $f_{\mathrm{esc,loc}} = 0.1$ tends to underestimate the data. Values in the range $f_{\mathrm{esc,loc}} = 0.3 - 0.7$ are in the best agreement with observational constraints – for the specific case of TNG50, i.e. the realization of the TNG galaxy formation model at the numerical resolution of TNG50. We further note that we have adopted only globally constant values of $f_{\mathrm{esc,loc}}$, i.e. the local escape fraction parameter does not depend on redshift nor mass. In reality, the dependence is likely more complex.

4.3.5 Single source escape fractions

We next examine the ability of ionizing photons to escape from individual stellar populations, in order to explore the stars that contribute, or not, to the budget of ionizing radiation escaping the halos.

The top panels of Figure 4.10 show the average escape fraction from individual star particles as a function of their age (left column) and distance from halo center (right column). We separate halos into three different stellar mass bins, namely, $M_\star = 10^{6.0-6.7} \mathrm{M}_\odot$, $10^{7.0-7.4} \mathrm{M}_\odot$ and $10^{8.0-8.1} \mathrm{M}_\odot$ (red, green, and blue lines). Note that while the scatter in the escape fraction of individual stellar populations is high, the large number of total stars in our calculations gives us strong confidence in the average values.

The average escape fraction as a function of stellar age (top left panel) decreases with

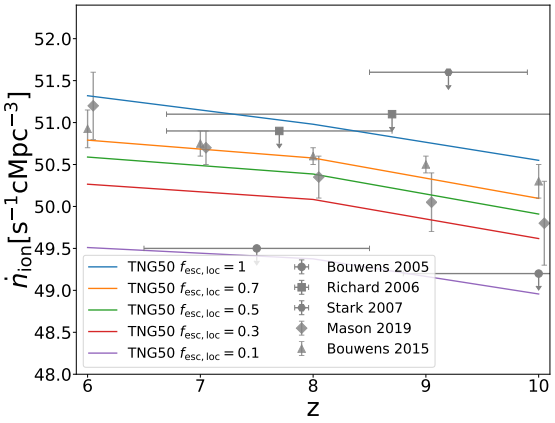

Figure 4.9: Ionizing photon emissivity predicted by the TNG50 and CRASH simulations as a function of redshift for various settings of the local escape fraction (indicated by lines of different color). Symbols refer to data, as indicated in the labels.

increasing age until it reaches a minimum at $\sim 20-30\%$ for ages of $\sim\ 20-30\,$Myr, before increasing slightly for older populations. As we have previously seen, young stars produce abundant ionizing photons, which are able to efficiently ionize the dense gas surrounding their formation sites and eventually escape. On the other hand, older stars are less efficient at forming ionized channels in the gas, resulting in a lower escape fraction. At the same time, older stars are less clustered within clouds of the densest and most neutral gas, enabling their relatively low production of ionizing photons to induce high escape fractions.

With respect to trends with galaxy mass, the youngest stellar particles tend to have the highest escape fractions for smaller halos, while the trend is reversed for the oldest stellar particles. We speculate that this behaviour is driven by the high central gas densities in massive halos, hindering the escape of the radiation from young stars.

The average escape fraction as a function of distance (top right panel) shows that close to the halo center the average escape fraction is smallest ($\approx 10-20\%$), as stellar particles located there are embedded in the denser gas. As we move further away from the center, the gas becomes less dense, resulting in higher escape fractions. Any sources which are located outside the central galaxy, i.e. in the circumgalactic medium, have large $f_{\rm esc}$, although the total luminosity of such sources is low. At large distances, the escape fraction plateaus to a constant value of $\approx 50\%$ and 30% for heavier and lighter halos, respectively. Here the decreasing gas density reaches a balance with the decreasing density of stellar sources.

The evolution of the escape fraction with radius is qualitatively similar for all mass bins. However, the effects of the absorption in the central regions is strongest for the most massive halos, and smallest for the least massive. Note that although the spread of the escape fraction of individual stellar particles is large, our sample size is sufficient to identify differences in the mean trends.

The bottom panels of Figure 4.10 show the fractional contribution of stars to the total budget of escaping and emitted photons, again as a function of their age (left) and halocentric distance (right). The contribution to the escaping photons (solid lines) peaks at

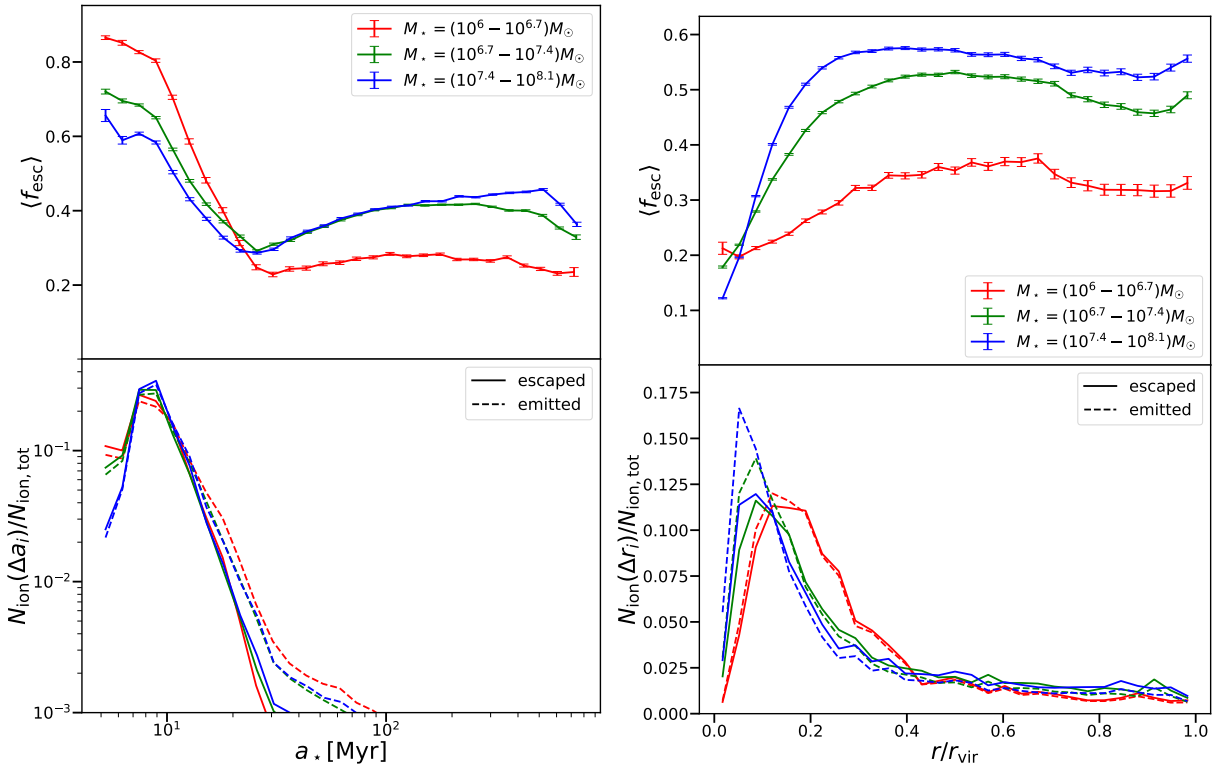

Figure 4.10: *Top panels:* Average halo escape fraction of individual stellar particles as predicted by the TNG50 and CRASH simulations, as a function of their age (left) and distance from the center of the halo (right) in three bins of stellar mass, indicated with the different colors. The errorbars represent the errors of the mean values. *Bottom panels:* Relative contribution of stars in a given age (left) and distance from the center (right) bin to the total ionizing photon budget. The solid and dashed lines denote the contribution to the escaped and emitted ionizing photons, respectively. Intermediate age stars born $\sim$tens of Myr ago, especially those not in the densest central region of the galaxy, have the largest escape fractions, while younger $\sim$ 10 Myr old stars on the outskirts of galaxies have the largest fractional contribution to the total ionizing photon budget.

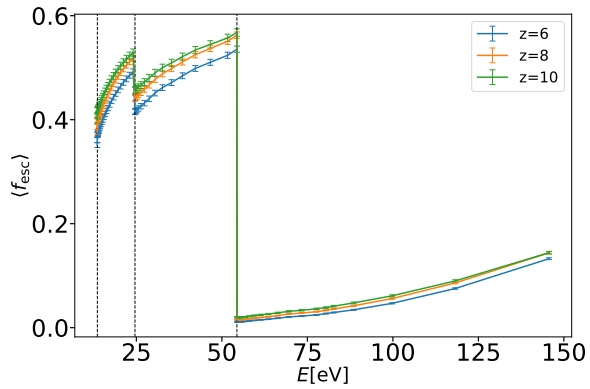

Figure 4.11: Average halo escape fraction as a function of photon energy for three different redshifts as predicted by the TNG50+CRASH RT simulations. The vertical dotted lines denote, from left to right, the ionization energies of HI, HeI and HeII. The error-bars correspond to the error of the mean value in a given energy bin. The results refer to our fiducial model with $f_{\rm esc,loc} = 1$. Escape fractions at high energies $E > 54.4$eV are substantially suppressed with respect to lower photon energies.

a stellar age of $a_\star \approx 10$Myr. The behaviour for $a_\star \gtrsim 10$Myr is very similar in all mass bins, while for younger stars the relative contribution is more significant for low-mass halos. Through a comparison to the emitted photons (dashed lines), a difference is seen in the two contributions only for $a_\star \gtrsim 20$Myr. In short, we find that while younger stars contribute to the emitted and emerging photon budget more or less equally, older stars contribute substantially more to the former than to the latter. This is due to stars whose emissivity is not enough to ionize the surrounding dense gas, corresponding to the minimum in the escape fraction observed in the top-left panel.[4]

As a function of distance (bottom right panel), the fractional contribution for both emitted and escaping photons rises quickly at small radii, reaching a peak at $\sim 0.1\,R_{\rm vir}$, before slowly declining at the very center. This peak shifts outwards and broadens with decreasing stellar mass. Emitted versus escaped photons show similar behavior in the smallest stellar mass bin. For higher masses, escaped photons exhibit a flatter distribution than their emitted counterparts. This reflects the fact that in larger halos ionizing photons emitted near the center are more easily absorbed by the surrounding gas.

4.3.6 Frequency dependence and the escaping spectra

Moving beyond a single (gray) characterisation of the escape fraction, we now take advantage of our multi-frequency approach to study how the escape fraction depends on photon frequency, as well as the impact on the emergent, versus intrinsic, spectra.

[4]Note, however, that these differences appear for stellar ages which contribute little to the total ionizing photon budget. They are, therefore, not of great importance for the resulting $f_{\rm esc}$. Even older stars have such a small contribution to the emission budget that they lie outside the range depicted.

Figure 4.11 shows the average escape fraction as a function of photon energy. We examine the halos in our fiducial configuration, i.e. $f_{\rm esc,loc} = 1$. Due to the frequency dependence of the cross section, the escape fraction has a local minimum at each of the ionization thresholds of hydrogen and helium. Rightwards of each such feature, $f_{\rm esc}$ then rises for higher energies, as gas becomes increasingly transparent to these frequencies.

The escape fraction is also dramatically reduced at energies just above the HeII ionization threshold because halos have abundant HeII – see the examples in Figure 4.4. This is largely due to the paucity of photons emitted at these frequencies, and this reduction acts in addition to the cross section effect. These finding are in agreement to those presented in [152].

We note only a slight evolution in the frequency-dependent escape fraction with redshift, where halos at $z = 10$ have an approximately 5% higher $f_{\rm esc}$ than halos at $z = 6$. Interestingly, the difference between the escape fraction at $z = 8$ and $z = 10$ is much smaller than between $z = 8$ and $z = 6$, suggesting a faster evolution of the escape fraction with redshift towards the end of reionization.

Additionally, also in agreement with [152], we find that the escape fraction of photons with energies larger than the HeI ionization energy (24.6eV) is slightly higher due to the lower abundance of Helium as compared to hydrogen. However, we do not find a significant redshift dependence. This could be partly explained by the fact that we do not consider halos with $M_{\rm vir} \sim 10^7$ M$_\odot$ which are thought to be the cause of that redshift evolution.

Figure 4.12 shows how the actual spectra are modulated by escape. We plot the normalized sum of spectra[5], i.e. the volume enclosed by each curve is the same. Most of the escaping radiation has energies below the HeII ionization at 54.4eV.

The top panel contrasts emitted versus escaping ionizing photons, and we see that the escaped spectrum has a lower amplitude at, or directly after, the ionization thresholds of hydrogen and helium. This effect is particularly visible after the HeII line at 54.4eV, reflecting the behaviour observed in Figure 4.11.

The middle panel splits this comparison based on galaxy stellar mass, comparing $M_\star > 10^8\,{\rm M}_\odot$ (blue lines) versus $M_\star < 5 \times 10^6\,{\rm M}_\odot$ (red lines). The difference between emitted and escaping spectra at energies E above 54.4eV is higher for the high-mass bin, than for the low-mass bin. As helium in all halos is mostly in the form of HeII rather than HeIII, photons with $E > 54.4$eV in more massive halos typically travel longer distances, and hence encounter a larger optical depth, before reaching the virial radius than photons in smaller halos. Such an effect is much less visible at $E < 54.4$eV because the gas is mainly in the form of HII and HeII and hence does not contribute to absorption in this range of energies.

However, this scenario does not apply for halos with small escape fractions, where both hydrogen and helium are mainly in their neutral state. When we split this comparison based on halo escape fraction (bottom panel), we see that halos with $f_{\rm esc} < 0.1$ have similar shapes in their emitted versus escaping spectra at all energies. In contrast, for high $f_{\rm esc}$ halos, we observe a clear difference at $E > 54.4$eV.

[5]As a result, the features of individual spectra are averaged out.

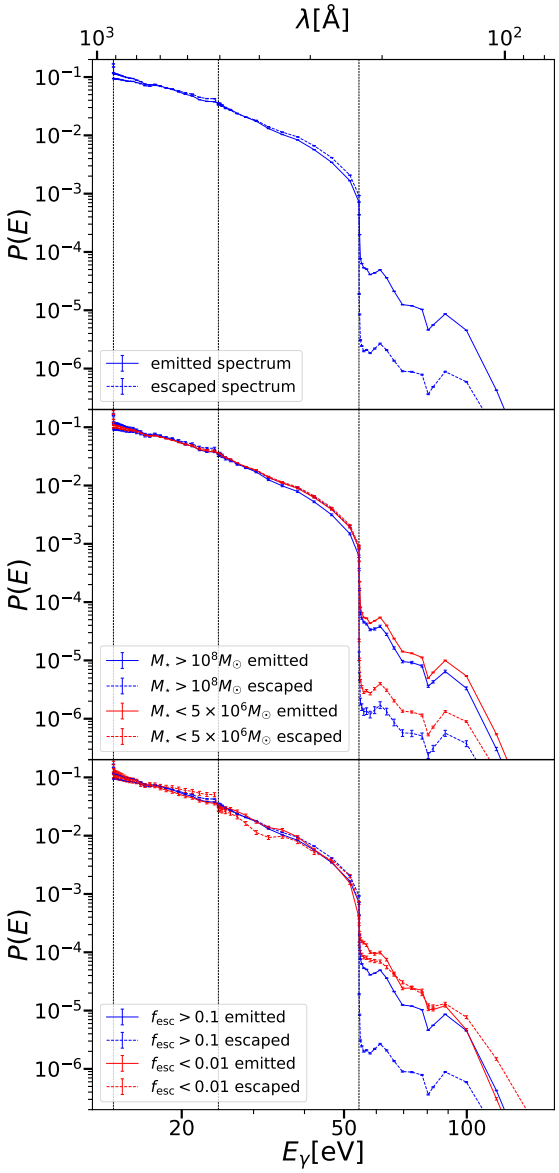

Figure 4.12: Normalized spectra of the emitted (solid lines) and escaping (dashed) ionizing photons for halos at all redshifts as predicted by the TNG50+CRASH RT simulations. The spectra have been calculated combining all halos (top panel); considering separately halos with stellar masses higher than $10^8\,M_\odot$ and lower than $10^6\,M_\odot$ (middle panel); and considering separately halos with an escape fraction higher than 10% and lower than 0.1% (bottom panel). In each case, the vertical dotted lines denote, from left to right, the ionization energies of HI, HeI and HeII.

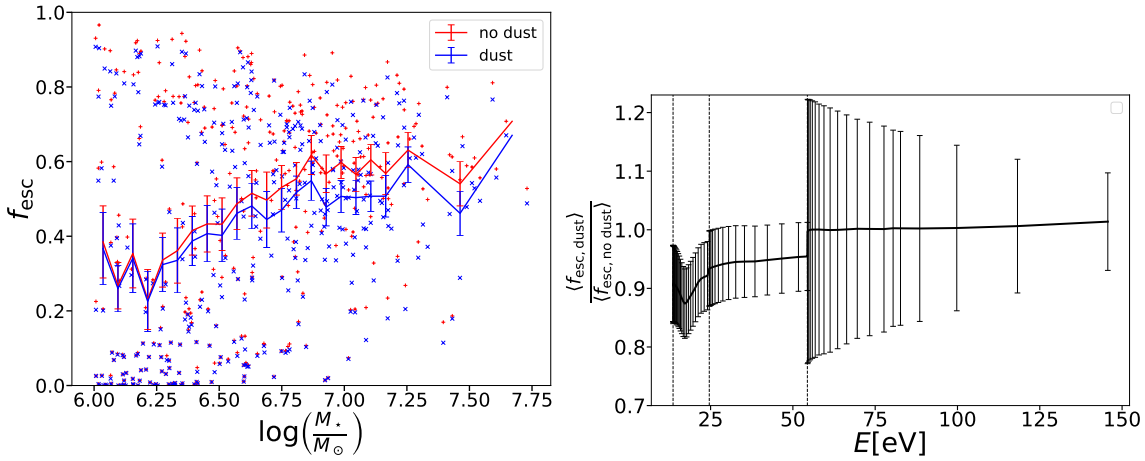

Figure 4.13: *Top:* Halo escape fraction as a function of stellar mass with (blue) and without (red) dust absorption, as predicted by the TNG50+CRASH RT simulations. The scatter corresponds to individual halos at all redshifts, while the lines show the average escape fractions. Overall, dust reduces the escape fraction of ionizing radiation, although the magnitude of this effect is modest. *Bottom:* Mean ratio of the halo escape fraction for dust versus no dust absorption, as a function of frequency. The error bars show the statistical uncertainty on the mean for each energy bin.

Taken together, these results suggest the following scenario. Although the SED of stellar populations with binary stars has a significant tail of HeII ionizing photons which is absent when only single stars are considered [72], these photons are more easily absorbed in comparison to those with energies below 54.4eV. Thus, the larger fraction of HeIII found in simulations of reionization including binary stellar systems (e.g. [123]), might be reduced when accounting for a frequency dependent escape fraction. We note, though, that HeII reionization is driven by more energetic sources (i.e. luminous black holes and X-ray binaries) and thus this caveat is not expected to have any major impact on the global reionization history.

4.3.7 Impact of dust absorption

Finally, we investigate the effect of dust on the escape fraction. To do so, we select a subset of halos and re-run the radiative transfer simulations including an additional dust component. The cross section of gas including dust is based on the model presented in [67], i.e. the Silicate-Graphite-PAH model [208, 43]. As total dust mass is not tracked in the TNG model, we adopt the simple prescription of a constant dust-to-metal (DTM) ratio of 40%, applied to each gas cell individually. In reality, the DTM ratio will be more complex, with dependencies on galaxy properties such as metallicity [169]. Our model is a simple choice which enables to explore, and place a reasonable upper bound, on the contribution of dust to the absorption of ionizing radiation (see also [119]).

Figure 4.13 shows the resulting trend of escape fraction versus stellar mass (top panel), contrasting the fiducial no dust case (gray) with the dust included model (black). At low stellar masses the escape fraction is only marginally affected by the presence of dust, with differences of order a few percent for $M_\star < 10^{6.5}\,\mathrm{M}_\odot$. Additionally, we still observe the bimodality from Figure 4.2, i.e. the existence of low-mass halos with very small escape fractions, further demonstrating that dust has little effect on $f_{\rm esc}$ in small halos.

However, dust becomes more important with increasing stellar mass. We observe a maximum impact on the escape fraction of $\sim 10\%$, which occurs for galaxies with $M_\star = 10^7\mathrm{M}_\odot$ and remains fairly constant for even larger halos. This trend is consistent with higher mass halos having a higher total metal and thus dust content, such that the dust contribution to total absorption is larger in more massive halos (see also [125]).

Figure 4.13 also presents the impact of dust on the average halo escape fraction as a function of frequency (bottom panel). One can see that the strongest decrease in the halo escape fraction happens at energies between the HI and HeI ionization thresholds, where the presence of dust decreases the escape fraction by $10 - 15\%$. In particular, we observe a dip in the escape fraction with a minimum at $\approx$ 20eV, roughly corresponding to the peak in the dust grain cross-section used in our model (see [67]). Between the HeII and HeIII ionization energies the suppression of the escape fraction remains roughly constant at $\approx 5 - 7\%$.

Finally, at energies higher than the HeII ionization threshold the contribution of dust to the total absorption becomes negligible. By comparing to Figure 4.11 it is clear that this is due to the absorption of ionizing radiation being fully dominated by the abundant HeII which has a significantly larger contribution to the absorption of highly energetic ionizing radiation than dust [67].

4.4 Summary and Conclusions

In this work we have investigated the dependence of the escape fraction of ionizing photons at halo scales, $f_{\rm esc}$, on different properties of the host galaxies and halos. To do this, we have post-processed halos extracted from the TNG50 simulation [146, 160] with the 3D multi-frequency radiative transfer code CRASH [32, 131, 74, 67]. We have explored galaxies with stellar masses $10^6 \lesssim M_\star/\mathrm{M}_\odot \lesssim 10^{8.5}$ at redshifts $6 < z < 10$.

Our main results can be summarized as follows:

- We find a large scatter of $f_{\rm esc}$, at fixed stellar and halo mass, across all redshifts and stellar masses in the range $10^6 - 10^8\mathrm{M}_\odot$ studied herein. This scatter increases substantially for low mass galaxies ($M_\star \lesssim 10^7\mathrm{M}_\odot$), where $f_{\rm esc}$ ranges from essentially zero to nearly 100% across the galaxy population, due to the inherent stochasticity of the (young) stellar populations of these galaxies.

- The escape fraction rises with increasing galaxy (or halo) mass, from $\sim 20\%$ at $M_\star = 10^6\,\mathrm{M}_\odot$ to a roughly constant value of $\sim 60\%$ at $M_\star = 10^7 - 10^8\,\mathrm{M}_\odot$. Towards

even higher masses, we see the hint of a turnover, after which escape fractions begin to decline.

- There is no consensus from cosmological (radiative/magneto)-hydrodynamical simulations for the value of $f_{\rm esc}$, nor its trend with galaxy mass. Our results are roughly consistent with some previous findings, and inconsistent with others.

- At fixed mass, the strongest predictor for the scatter in $f_{\rm esc}$ is the total ionizing emissivity of the halo. However, the escape fraction also depends on the details of the spatial distribution of (stellar) sources in relation to the underling gas distribution.

- Halos with a stellar (halo) mass $\lesssim 10^{7.5}$ (10^{10}) $\mathrm{M}_\odot$ contribute the majority of ionizing photons at all redshifts. The global ionizing emissivity $\dot{N}_{\rm ion}$ obtained by summing the contributions of all halos can easily match observational constraints, for intermediate values of an unresolved local escape fraction $f_{\rm esc,loc} = 0.3 - 0.7$.

- The absolute value of $f_{\rm esc}$ depends, non-linearly, on our adopted value for the local (unresolved) escape fraction, i.e. the attenuation of ionizing radiation below the resolution scale of the simulation.

- $f_{\rm esc}$ is strongly dependent on the photon energy. Due to the frequency dependence on the absorption cross-section and the abundant HeII present in most halos, its global average value is much smaller ($<$ 10-15%) at $E > 54.4$eV than at lower energies, where it is above 35%. This suggests that the impact on reionization from the high energy tail of binary stellar systems might be reduced when accounting for an energy dependent escape fraction.

- The presence of dust, when included self-consistently in our radiative transfer approach, reduces $f_{\rm esc}$. However, the magnitude of this effect is moderate, escape fractions decreasing by a few percent at $M_\star \lesssim 10^{6.5}\mathrm{M}_\odot$, and up to 10% for larger halos.

In this work we have opted to solve the radiative transfer in post-processing. While RHD simulations have the advantage of capturing the back-reaction of the radiation on the gas, they are extremely expensive in terms of computation time and thus generally employ a less accurate radiative transfer scheme (often applied only to the hydrogen component of the gas), as well as a fairly coarse resolution of the source spectrum (typically 1-3 frequency bins). Conversely, performing the radiative transfer in post-processing allows us to employ an accurate Monte Carlo algorithm to follow the propagation of ionizing photons, as well as employ a fine spectral resolution (64 bins), in addition to modeling dust and gas (in its hydrogen as well as helium components) absorption self-consistently. Due to the computational expense of our approach we have limited the analysis to halos with $M_{\rm vir} < 10^{11}\mathrm{M}_\odot$. However, we have seen in Figure 4.8 that such halos, because of their low abundance, do not provide a major contribution to the process of reionization. Hence,

although intrinsically an interesting problem, precise knowledge of the escape fraction from high-mass halos is not critical for the modeling of cosmic reionization.

Currently, the main limitation in our modeling of the escape fraction is the treatment of the gas phase-structure in the dense interstellar medium. This arises from two related aspects: the numerical resolution of the TNG50 simulation, and the sub-grid model for the two-phase structure of star forming gas. As a result, our findings depend on a local, or unresolved, escape fraction parameter. This choice applies to all simulation studies of escaping radiation. The absolute value of $f_{\rm esc}$ is ultimately dependent on the adopted prescription for the unresolved absorption. In this work we have presented the first systematic study of the effect of varying the sub-grid cloud-scale escape fraction on $f_{\rm esc}$, but more study is motivated. In the future, it will be imperative to better constrain and/or model $f_{\rm esc,loc}$ as a function of local gas properties, global galaxy or halo properties, and/or a combination thereof.

Data Availability

Data directly related to this publication and its figures is available on request from the corresponding author. The IllustrisTNG simulations, including TNG50, are publicly available and accessible at `www.tng-project.org/data` (see [146]).

Acknowledgements

We thank the anonymous referee for an insightful review that helped to improve the manuscript.The authors are grateful to Enrico Garaldi for useful discussions, and also thank Aaron Smith for helpful comments. DN acknowledges funding from the Deutsche Forschungsgemeinschaft (DFG) through an Emmy Noether Research Group (grant number NE 2441/1-1). This work is supported by the Deutsche Forschungsgemeinschaft (DFG, German Research Foundation) under Germany´s Excellence Strategy EXC 2181/1 - 390900948 (the Heidelberg STRUCTURES Excellence Cluster). The TNG50 simulation was run with compute time granted by the Gauss Centre for Supercomputing (GCS) under Large-Scale Projects GCS-DWAR on the GCS share of the supercomputer Hazel Hen at the High Performance Computing Center Stuttgart (HLRS). GCS is the alliance of the three national supercomputing centres HLRS (Universität Stuttgart), JSC (Forschungszentrum Jülich), and LRZ (Bayerische Akademie der Wissenschaften), funded by the German Federal Ministry of Education and Research (BMBF) and the German State Ministries for Research of Baden-Württemberg (MWK), Bayern (StMWFK) and Nordrhein-Westfalen (MIWF). Additional simulations and analysis were carried out on the Freya machine of the Max Planck Institute for Astrophysics (MPA) and systems at the Max Planck Computing and Data Facility (MPCDF).

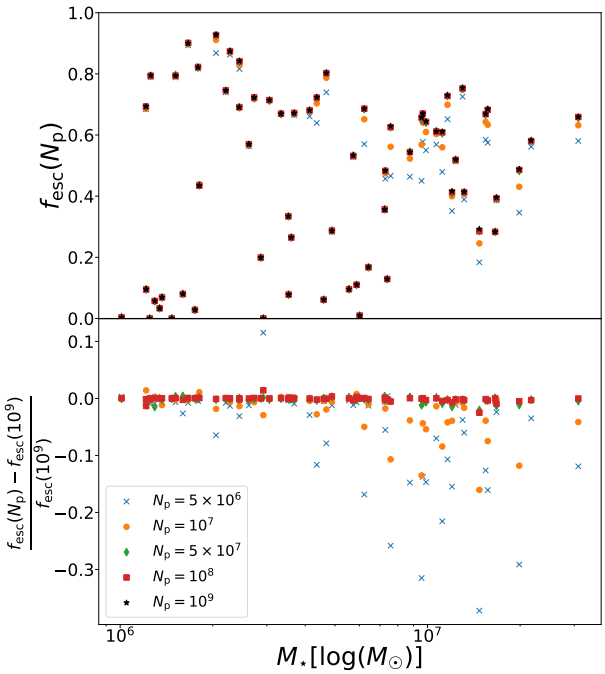

Figure 4.14: *Top panel:* Escape fraction as a function of stellar mass for different numbers of photon packets emitted per stellar particle. *Bottom panel:* Relative deviation of $f_{\rm esc}$ obtained with N_p photons from $f_{\rm esc}$ obtained with $N_p = 10^9$ photon packets.

Appendix

Numerical convergence

As discussed in Section 4.2, in the CRASH radiative transfer (RT) simulation, Monte Carlo sampled photon packets are propagated from stellar sources through the simulation domain. To obtain an accurate evaluation of gas properties, it is crucial that each voxel is crossed sufficiently often by a photon packet, i.e. the results are sensitive to the source sampling. To demonstrate that our results are numerically converged with respect to the photon packet number, we have thus run a subsample of halos with different numbers of photons packets emitted per source.

We show the resulting escape fractions in Figure 4.14, where we also plot the relative deviation of the escape fraction obtained with a given photon packet number from the highest setting, i.e. $N_{\rm p} = 10^9$. We see that a strong convergence, with an error $\lesssim 1\%$ for all mass bins, is reached only for $N_{\rm p} \gtrsim 5 \times 10^7$. To account for a possible increase in the error due to longer lines of sight in larger halos, we have therefore adopted a conservative $N_{\rm p} = 10^8$ for our RT runs.

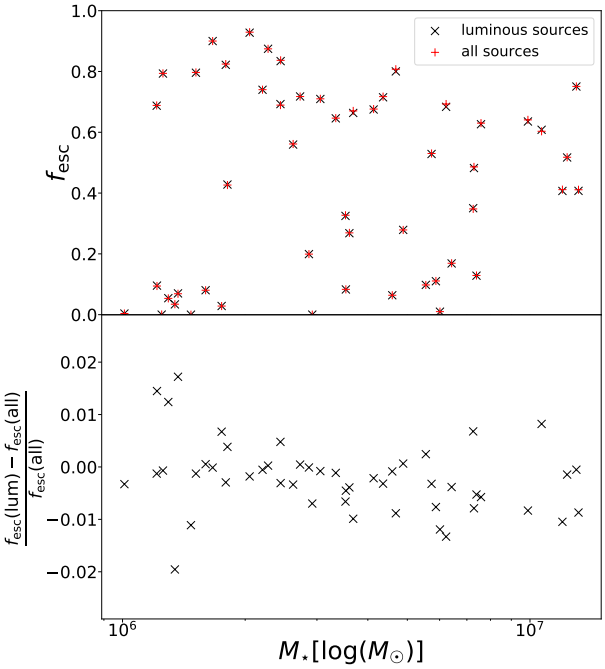

Figure 4.15: *Top panel*: Escape fraction for a subsample of halos with source reduction as used in our production runs (black) and all the stellar particles in the simulation (red). *Bottom panel*: Deviation from the escape fraction in the runs with reduced sources as compared to running the halos with all sources.

Reduction of source numbers

To limit the computational cost of the radiative transfer simulations, we have developed and tested an approach, similar to the one described in [44], which reduces the number of sources without affecting the final results. For each halo, all sources with an emissivity Q_{sources} less than a given percentage of the maximum source emissivity found within that halo are merged into nearby more luminous sources if they are within N voxels, otherwise they are completely removed. We have run a number of tests to investigate the impact of a different choice for the merging distance.

Figure 4.15 shows the effect of the source reduction on the escape fraction of a sample of halos for our reference case of a threshold percentage of 1% and a merging distance of 5 voxels. We have verified that as long as the threshold percentage is below 1%, more than 99% of the halo emissivity is conserved, and our results are unchanged.

Gas phase diagram in a prototypical halo

Here we investigate the temperature of the gas in our simulation, and the resulting impact of RT. To do so we consider the temperature-density distribution of gas in galaxies, as well as how the escape fraction is affected by an accurate temperature solver in the RT simulation.

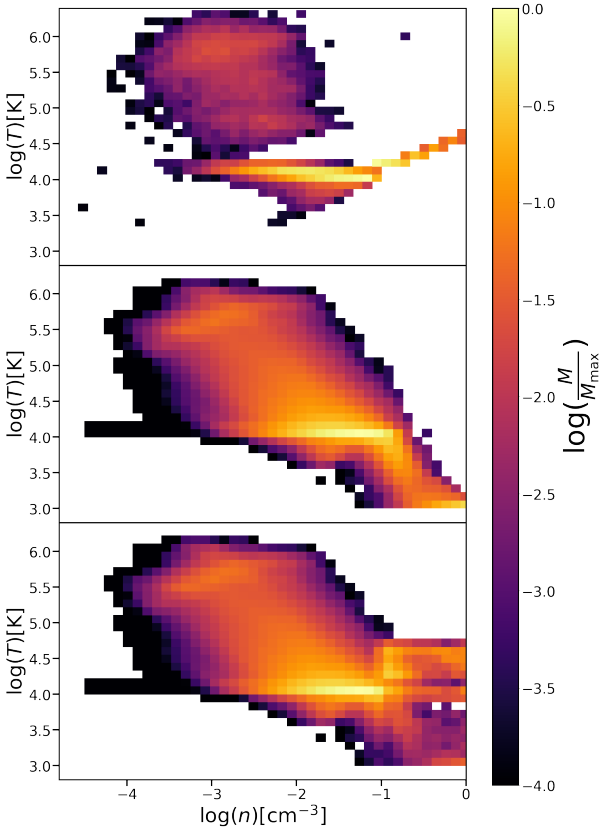

Figure 4.16: Phase diagrams of one example halo with a stellar mass of approximately $10^8 M_\odot$. From top to bottom: Histogram of gas cells before gridding, after gridding, and after RT processing. Note that during the gridding procedure we set the temperature of star-forming gas (densities above 0.1cm^{-3}) to 1000K, to be consistent with the two-phase ISM pressure model of TNG50.

One representative example of the temperature-density diagrams is shown in Figure 4.16. Other halos exhibit similar temperature-density distributions. Here, we show the distribution of gas mass in this phase diagram for three cases: before gridding (top panel), after gridding (middle panel) and after radiation equilibrium has been reached (bottom panel), i.e. after the RT simulation.

As mentioned previously, the temperature of star forming gas particles with $n > 0.1\text{cm}^{-3}$ is set to 1000K, consistent with the two-phase ISM model [190] used in TNG50. This, after gridding, explains the turnover of the high density gas towards colder temperatures. After RT, a significant fraction of this dense gas has been heated. Importantly, our RT does not cause a change in the temperature state of the very hot, low density gas. This is because we do update the temperature of cells crossed by photon packets if the temperature of that cell is larger than 10^4K, to avoid losing effects such as feedback-induced heating and hydrodynamical shock heating.

Finally, in Figure 4.17 we explore the importance of using a temperature solver (our

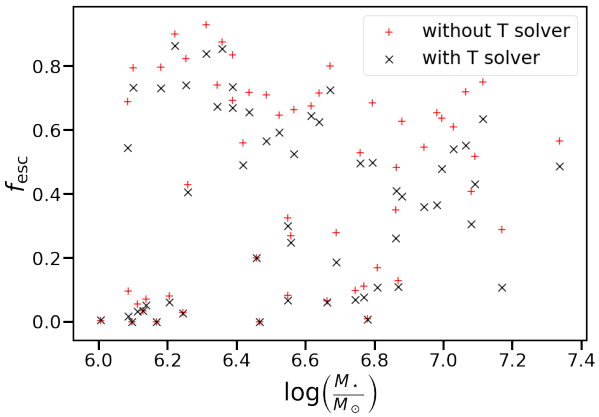

Figure 4.17: Comparison of the escape fraction if the CRASH temperature solver is turned on (black), versus if it is not (red). In the latter case, a simple temperature update scheme is applied (see text). Overall, this choice is not critical to our fiducial results.

fiducial choice) rather than a simplified temperature update scheme. In the simplified scheme the temperature for most cells is given by the input temperature of the cells. However, if the cell reaches an ionization state of $x_{\rm HII} > 0.5$ the temperature in that cell is set to $T = \max(T_{\rm cell}, 10^4{\rm K})$. This is necessary to avoid numerical problems that occur if a cell is fully ionized while also having a relatively low temperature.

The simplified temperature update scheme causes the escape fractions to be slightly higher, a $\sim 5\%$ level effect. This is caused by an overestimation of the temperature of partly ionized cells, which reduces the recombination rate considerably, as the recombination parameter scales negatively with temperature [24]. Overall, this choice is not critical to our fiducial results.

Convergence with underlying simulation resolution

In order to investigate how the escape fraction converges with the numerical resolution of the underlying galaxy formation simulation, we processed a sample of halos from the TNG50-2 and TNG50-3 simulations with the same RT procedure as the fiducial sample, and investigated the resulting escape fraction. The TNG50-2 and TNG50-3 simulations are run with the same initial conditions as TNG50, but with a reduced number of particles, resulting in 8 and 64 times worse mass resolution, respectively.

Figure 4.18 shows the average escape fraction trends as a function of stellar mass, for these three resolution levels. For most stellar masses the escape fraction is smaller with lower resolution. At the low-mass end, this trend is largely due to the bimodality observed in Figure 4.2 extending to higher masses. That is, low mass galaxies at low resolution are less populated by stars, and this stochasticity pulls down the average escape fraction. However, only a small fraction of halos have most of the ionizing emissivity, such that the emissivity weighted escape fraction is roughly unchanged, while the average escape fraction is lower. For stellar masses $M_\star \lesssim 10^7 M_\odot$, the escape fraction decreases on average

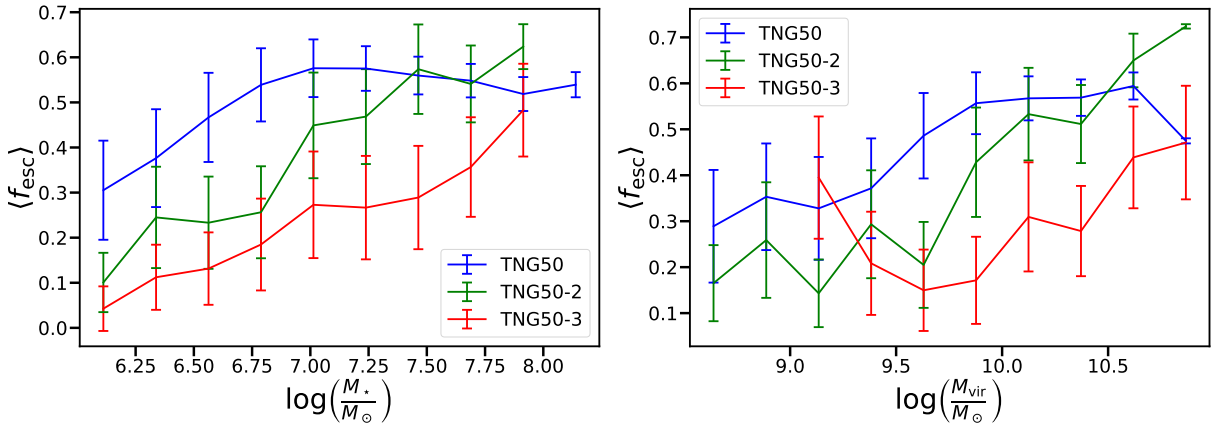

Figure 4.18: Average escape fraction as a function of stellar mass (top) and halo mass (bottom) for three different resolution realizations of the TNG50 volume: TNG50-1 (highest), TNG50-2 (intermediate) and TNG50-3 (low). At each step the mass, or spatial, resolution is worse by a factor of eight, or two, respectively.

by $\sim 15\%$ for a factor 8 worse simulation mass resolution.

For intermediate mass halos, with stellar masses $\sim 10^{7.5}\,\mathrm{M}_\odot$, TNG50-2 and TNG50-1 show reasonable convergence. Given our lack of sampling of high-mass halos, the convergence behavior at $\gtrsim 10^8\,\mathrm{M}_\odot$ is difficult to demonstrate.

Numerical convergence is clearly a challenging issue. Note, however, that when moving to lower resolution simulations, we would typically adopt a correspondingly higher galaxy mass threshold above which a galaxy was considered 'well-resolved'. In this sense, it is expected that the lowest mass galaxies are simply not resolved in TNG50-2 and especially in TNG50-3, and should not be studied in detail.

Chapter 5

Physically motivated modeling of LyC escape fraction during reionization in the TNG50 simulation

5.1 Introduction

To gain a more comprehensive understanding of the mechanisms behind LyC escape, it is of great interest to construct an analytical physical model that delineates this process. By enabling rapid, simulation-independent estimation of the escape fraction, this would facilitate straightforward adaptation to new discoveries and constraints regarding galactic populations at high redshift. As the last chapter and in particular fig. 4.3 have shown, the LyC escape fraction is only weakly constrained through simulations. Likewise, a simple analytic model is unlikely to capture the process of LyC escape with quantitative precision. Therefore, the objective of the presented analytical model is to accurately depict the locations and conditions in which LyC leakage occurs.

Our approach builds on the LyC escape modeled being developed by Ferrara et al. (in prep.). However, while this model is build to evaluate the escape of LyC photons directly for the entire galaxies. In our approach however, we subdivide the galaxy onto a regular grid and evaluate the LyC escape on each individual grid cell. In this work we calculate the LyC escape of TNG50 galaxies at redshifts $20 > z > 5.2$. However, this model can be easily generalized to other simulations.

Finally, for large scale simulations individual galaxies and their LyC producing and leaking regions are often not sufficiently resolved. In order to nevertheless have an estimate for the escape fraction we fit our result to a simple six parameter model which only takes into account the galactic gas mass, its stellar mass and its redshift to provide a statistically reliable estimate for the escape fraction.

We structure this chapter as follows: In section 5.2 we present our methodology for modelling LyC photon production and escape in TNG50 galaxies. In section 5.3 we discuss the geometry of LyC escape as well as its correlation with galactic properties. We

subsequently introduce a fitting formula for the LyC escape fraction and analyze its accuracy in section 5.5. We finally summarize our results and conclude in section 5.6.

5.2 Method

5.2.1 The IllustrisTNG simulation

In this work we model the LyC escape fractions of galaxies taken from the Illustris TNG50 simulation [159, 191, 142, 145, 129]. It is one of three large scale cosmological simulations together with TNG100, and TNG300. These simulations use the same physical modelling. TNG50 simulates the evolution of structures in a cosmological volume of $(51.7\text{Mpc})^3$ [146, 160]. In order to generate the initial conditions for the simulation, the N-GenIC code [192] was used and the initial redshift was set to $z = 127$. The cosmological parameters were set to the values as measured by [162], i.e. $\Omega_\text{m} = 0.3089$, $\Omega_\text{b} = 0.0486$, $\Omega_\Lambda = 0.6911$, $h = 0.6774$, $\sigma_8 = 0.8159$ and $n_s = 0.9667$. The simulation is run up to the present moment, i.e. $z = 0$ and the galactic distribution is verified against cosmological observations. For our investigations of high redshifts, this fact provides some reliability that the high redshift galaxies we work with are realistic progenitors of the galactic populations we see today.

The mass resolution of the TNG50 galaxy given by the initial masses of the particles in the simulation is $4.5 \times 10^5 M_\odot$ for dark matter and $8.5 \times 10^4 M_\odot$. However during the simulation refinement and de-refinement of Voronoi cells leads to these values to vary within a factor of two. The spatical resolution varies strongly from the inner part of galaxies to the IGM. The mean size of star forming gas cells which are of most relevance for our study at $z = 6$ is 144pc with 16-84th percentiles ranging from 96 to 184pc. When a stellar particle is formed it inherits the mass of the baryonic gas cells it formed in. This mass decreases as its stellar population evolves with time.

The underlying physical model is described using the AREPO code [189]. Hereby, the interaction of baryonic matter is modelled using the equations of ideal MHD [153] solved on a Voronoi grid. The galaxy formation model is based on [207] and [161]. Hereby, baryonic mass is converted to stellar particles stochastically in Voronoi cells where the critical density threshold of $n_\text{H} = 0.1\text{cm}^{-3}$ is surpassed based on the Kennicutt-Schmidt relation [190]. Each stellar particle represents a stellar population for which TNG assumes a Chabrier initial mass function [25]. To capture the effects of subgrid feedback and account for pressure support in star-forming gas, the [190] model for the ISM was employed. Feedback from supernovae is modelled through decoupled kinetic wind particles [161]. Supermassive black holes (SMBHs) are seeded at the center of all galaxies that surpass a threshold mass of $10^{10.8} M_\odot$. The seeded black holes have an initial mass of $8 \times 10^5 h^{-1} M_\odot$. These SMBHs then proceed to grow through gas accretion in accordance to the Bondi formalism with the limit given by the Eddington rate. Further growth is enabled though SMBH-SMBH mergers during the merging of galaxies. To account for feedback effects of SMBHs, the simulation implements thermal heating and radiative influences when the accretion rate is high, as well as kinetic wind when the accretion rate is low. These mechanisms subsequently deposit

the feedback energy into the surrounding gas [207]. Finally, the metallicity enrichment is traced including the individual enrichment with C, N, O, Ne, Mg, Si, Fe and Eu in addition to the modelling of the H and He gas contents.

Radiation transfer is not modelled explicitly in TNG. However, at redshifts $z < 6$, i.e. after reionization, a spatially uniform UV-background (UVB) is turned on. The results of [53] (including its 2011) update are used for the UVB prescription.

The galaxies we investigate in this work are contained in subhalos. They are identified using the SubFind algorithm [193] which uses the friends-of-friends algorithm [37] to detect structures. The minimum number of particles required for a subhalo is 20 which results in a minimal subhalo mass of $\sim 10^6 M_\odot$ that can be considered resolved.

5.2.2 Physical model of LyC escape

The model underlying our calculations of the escape fraction was developed in (Ferrara et al. 2022, in prep). Hereby, the galaxy is considered a plan parallel slab based on the model presented in [55]. The stars are distributed on the galactic disc, with the gas distributed above and below the galaxy with a constant density up to a column height of H resulting in a column density N_0. The stars emit an ionizing flux which is absorbed by gas and dust on top an below the disc. LyC photons can escape if the ionizing flux is large enough to form an ionized channel in the gas.

The ionizing photon number flux is given by

$$F_i = \int_{\nu_L}^{\infty} \frac{F(\nu)}{h_P \nu}. \tag{5.1}$$

Here ν represents the frequency, ν_L the Lyman continuum limit frequency corresponding to a photon energy of 13.6eV, $F(\nu)$ is the energy flux as a function of frequency and h_P the Planck constant.

Given the gas density $n = N_0/H$ the photon flux can be related to the photon-to-gas density ratio as

$$U = \frac{F_i}{nc}, \tag{5.2}$$

with c being the speed of light. We can further related the flux to the Strömgren depth l_S, i.e. the maximum distance that can be ionized by the flux

$$l_S = \frac{F_i}{n^2 \alpha_B}, \tag{5.3}$$

with α_B being the case B recombination rate. Given these quantities we can define the maximum column density that can be ionized by the flux

$$N_S = n l_S = \frac{Uc}{\alpha_B}, \tag{5.4}$$

and the optical depth encountered by LyC photons through the hydrogen gas

$$\tau_{\mathrm{HI}} = \frac{N_0}{N_S}. \tag{5.5}$$

The ionizing flux is additionally absorbed by the dust content in the gas. The dust cross section per H atom in the V band is given by

$$\sigma_{d,V} = 4.8 \times 10^{-22} \mathcal{D} \mathrm{cm}^2. \tag{5.6}$$

Hereby, $\mathcal{D}$ represents the dust-to-gas ratio normalized to the galactic value. Assuming a linear relation between the metallicity Z and dust, the dust content can be written as

$$\mathcal{D} = \frac{Z}{Z_\odot}, \tag{5.7}$$

with $Z_\odot$ being the solar metallicity. With this we can define the dust optical depth to LyC photons

$$\tau_d = \left(\frac{A_L}{A_V}\right) \sigma_{d,V} N_0. \tag{5.8}$$

Here the LyC to V-band attenuation ratio was used which according to [208] and assuming an $R_V = 3.1$ is given by $A_L/A_V = 4.83$. It should be noted that this ratio is based on Milky Way extinction curves and could be sensitive to redshift evolution. By utilizing the result of the optical depth due to dust, we are able to determine the gas column density at which it reaches unity

$$N_d = 4.3 \times 10^{20} \mathcal{D}^{-1} \mathrm{cm}^{-2}. \tag{5.9}$$

The LyC escape fraction f_{esc} is defined as the fraction of photons not absorbed by the optical depth, i.e. it is given by

$$f_{\mathrm{esc}} = e^{-\tau_{\mathrm{tot}}}. \tag{5.10}$$

Here, τ_{tot} is the total optical depth of the gas in the galaxy i.e. $\tau_{\mathrm{tot}} = \tau_{\mathrm{HI}} + \tau_d$. Hence, we can write the escape fraction as [1]

$$f_{\mathrm{esc}} = \exp\left[-N_0 \left(\frac{1}{N_S} + \frac{1}{N_d}\right)\right]. \tag{5.11}$$

5.2.3 Obtaining the escape fraction of TNG50 galaxies

In this work we analysed the escape fractions of $\approx 600,000$ TNG50 galaxies in the redshift range $5.2 \geq z \geq 20$. To have a sufficient resolution we post-processed all galaxies within the simulation with a minimum stellar mass of $M_\star = M_{\star,\mathrm{min}} = 10^{5.5} M_\odot$ and a minimal gas mass of $M_{\mathrm{gas,min}} = 10^6 M_\odot$. The number of galaxies in each redshift bin is depicted in fig. 5.1. Given that the snapshots in the TNG50 simulation are not sampled in constant redshift intervals, the lower redshift range is significantly better sampled.

In order to obtain the LyC escape fraction for each galaxy we proceede as follows. First we define the galactic disc as the plane defined by the first two principle axes of the galaxy.

[1] Note that in (Ferrara et al., in prep) also takes into account a reduction in N_0 due to radiation pressure pushing out part of the gas. However, in our study this effect turned out to be negligible. Therefore, here we present only this simplified model.

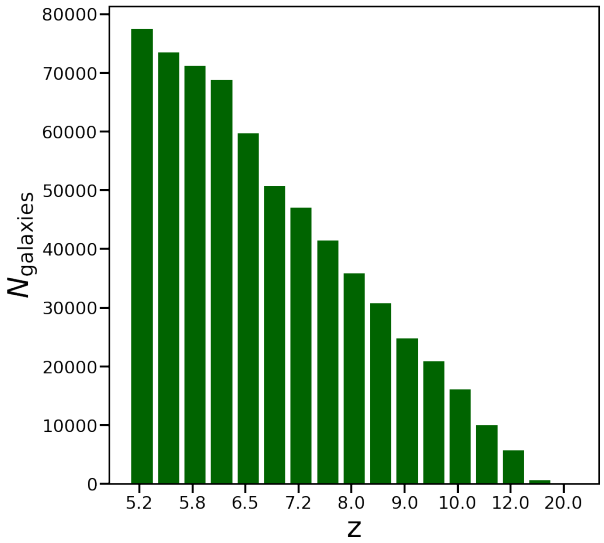

Figure 5.1: Number of galaxies processed as function of redshift.

We cut out a box with a side length of four times the stellar half mass radius r_{HMR} of the galaxy i.e. we ensured that the galactic disc up to a radius of $2r_{\text{HMR}}$ is included in the analysis. The gas particles within that box were distributed on a regular Cartesian grid using 100^3 grid cells for each galaxy (see appendix 5.6 for a convergence study). The goal hereby is to sufficiently resolve the distribution of gas as well as the star forming regions.

The column height H of the gas in the galaxy was defined by the height above and below the galactic disc plane, containing $\approx 63\%$ $(1/e)$ of the gas mass. Once we have obtained the scale height the needed information about the gas namely its mass, star formation rate (SFR) and metallicity is projected onto a two dimensional 100^2 grid and converted into area density values.

In order to obtain the ionizing flux in the galaxy we need to relate it to a quantity that is traced in the TNG simulations. In this work we use the star formation rate (SFR) of the gas for this purpose. We used the fact that the ionizing energy flux as a function of frequency as used in eq.5.1 can be modelled through a power law decline with energy [55]

$$F(\nu) = F_L \left(\frac{\nu}{\nu_L}\right)^{-\beta}. \tag{5.12}$$

Here F_L is the energy flux at the Lyman limit $\nu_L = 3.2 \times 10^1 5\text{Hz}$. The value for β is usually assumed to be in the range $4-5$ for PopII stellar populations. Inserting eq.5.12 into eq.5.1 and solving the integral results in

$$F_i = \frac{F_L}{\beta h_P}. \tag{5.13}$$

To relate F_L to the SFR we use the conversion between UV luminosity F_{1500} and the surface density of star formation Σ_{SFR} as used by the REBELS collaboration [39]

$$F_{1500} = \Sigma_{\text{SFR}} \times \kappa^{-1}. \tag{5.14}$$

For a Chabrier IMF as it is assumed in the TNG50 simulation the conversion factor is $\kappa = 7.1 \times 10^{-29} M_\odot \mathrm{yr}^{-1} \mathrm{erg}^{-1} \mathrm{sHz}$. We further take into account that for a Chabrier IMF $F_{1500} \approx F_L$. Hence, the ionizing flux can be calculated through

$$F_i = \frac{\Sigma_{\mathrm{SFR}}}{\beta h_P \tau}. \tag{5.15}$$

In order to obtain the escape fraction we computer N_0, N_S and N_d individually for each element of the 2-dimensional grid and evaluate eq.5.11. The escape fraction of the galaxy is then given by the emissivity weighted average escape fraction of these cells

$$f_{\mathrm{esc}} = \frac{\sum_{\mathrm{cell}} F_{i,\mathrm{cell}} f_{\mathrm{esc,cell}}}{\sum_{\mathrm{cell}} F_{i,\mathrm{cell}}}. \tag{5.16}$$

5.3 Results

5.3.1 Dependence on stellar mass and redshift

First we investigate the distribution of LyC escape fractions (f_{esc}) as a function of the galactic mass. In fig.5.2 we depict the distributions of the average f_{esc} on a color scale as a function of both the redshift and the galactic stellar and gas mass.

In the left-hand plot we see a strong correlation between the the stellar mass and f_{esc}. The escape fraction increases with stellar mass up to $M_\star \approx 10^{6.5} M_\odot$ at $z = 5.2$, with this value reaching $M_\star = 10^7 M_\odot$ for $z \approx 10$. Afterwards, the value decreases and is essentially zero for large stellar masses $M_\star > 10^8$. We see that the region with the highest escape fractions moves towards higher stellar masses with redshift a phenomenon which will be discussed later. In the lowest stellar mass bin we obtain high escape fractions as well. However, as the contour lines indicates, these galaxies only make up a small fraction of the sample.

The scatter of escape fractions is much larger as a function of the galactic gas mass. Here we see a maximum in the escape fraction ranging from a gas mass of $M_{\mathrm{gas}} = 10^8 M_\odot$ at $z = 5.2$ to $M_{\mathrm{gas}} = 10^{8.5}$ at $z = 12$. The generally higher f_{esc} we see are explained by the majority of the high-escape bins being located outside the regions containing most of the galaxies. We also see a secondary peak in the escape fractions for galaxies with a gas mass $< 10^{6.5} M_\odot$. Here the trends indicate the opposite evolution with redshift as in the first peak.

In fig. 5.3 we depict the average f_{esc} as a function of stellar and gas mass for a sample of redshifts.

In the left-hand plot we see again the shift of the peak of the f_{esc} towards higher stellar masses with redshift. Furthermore, we also see that the absolute value of the f_{esc} seems to decrease with redshift as well up to $M_\star \approx 10^7 M_\odot$ after which the lines overlap and the high redshift results becomes less reliable due to the the small samples of high redshift galaxies.

In the right-hand plot the evolution with gas mass is slightly different. First of all, as we have already seen in fig.5.2 the escape fraction at first decreases with gas mass up to a

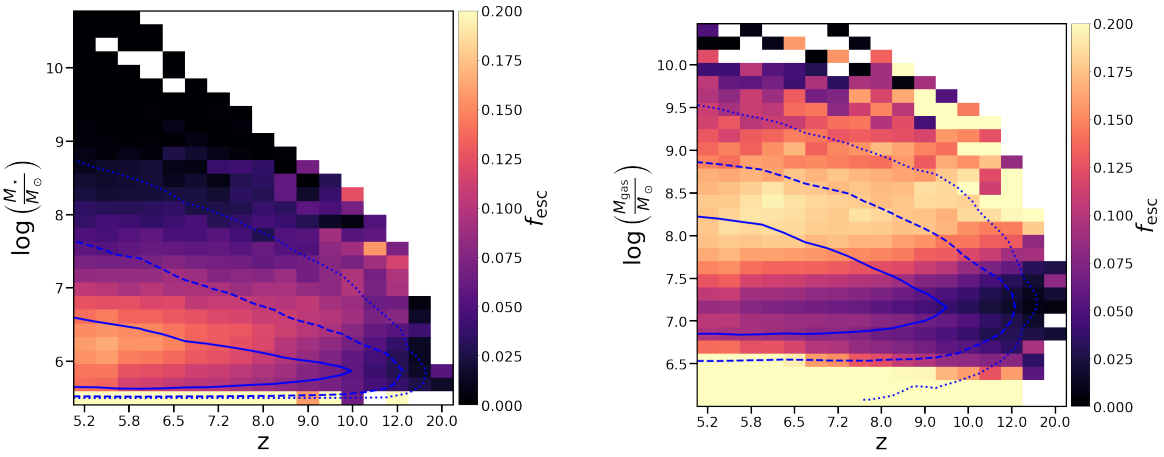

Figure 5.2: Average LyC escape fraction on a color scale as a function of redshift and stellar (left) as well as gas (right) mass. The blue contours denote the one (solid), two (dashed) and three (dotted) sigma distribution of galaxy counts.

minimum at $10^{7.3} M_\odot$ before increasing again for higher gas masses. Note that this initial decrease is particularly strong from lower redshifts reflecting the trend in the color plot. Unlike, in the left-hand plot there does not seem to be a difference in the peak escape fraction at the various redshifts although the we do see higher escape fractions for lower redshifts for lower gas masses.

5.3.2 Escape modes

Next we analyze in detail what drives LyC escape in the galaxies we investigated. For that purpose we investigate the correlations of $f_{\rm esc}$ with various properties of the galaxies.

In fig. 5.4, we depict a histogram of the average escape fraction as a function of column heights and star formation rate. Here, we can identify two distinct modes where we observe relatively high escape fractions of $f_{\rm esc} > 0.2$. We will denote these two regions as escape mode 1 and 2. Mode 1 is characterized by higher column heights $> 10^{21}$cm and a higher upper bound in terms of SFR as well as the presence of a lower bound. Here we see at higher SFR values a power-law trend dividing the LyC leaking and non leaking galaxies. This trend reverses its direction at lower SFRs. Region 2 is located at smaller column height $< 10^{21}$cm which is capped at relatively small SFRs and is bounded from above by a similar trend as mode 1. However, we do not observe a lower bound. The two regions are divided by region 3 where the average escape fraction is lower than in the two modes. This region contains the bulk of galaxies as indicated by the contour lines.

In the lower part of the figure we plot a sample of three galaxies from each of the three regions. In fig.5.5 we examine these galaxies in some more detail by looking at their ionizing fluxes and the ratio N_0/N_S, which in this case is approximately equivalent to the

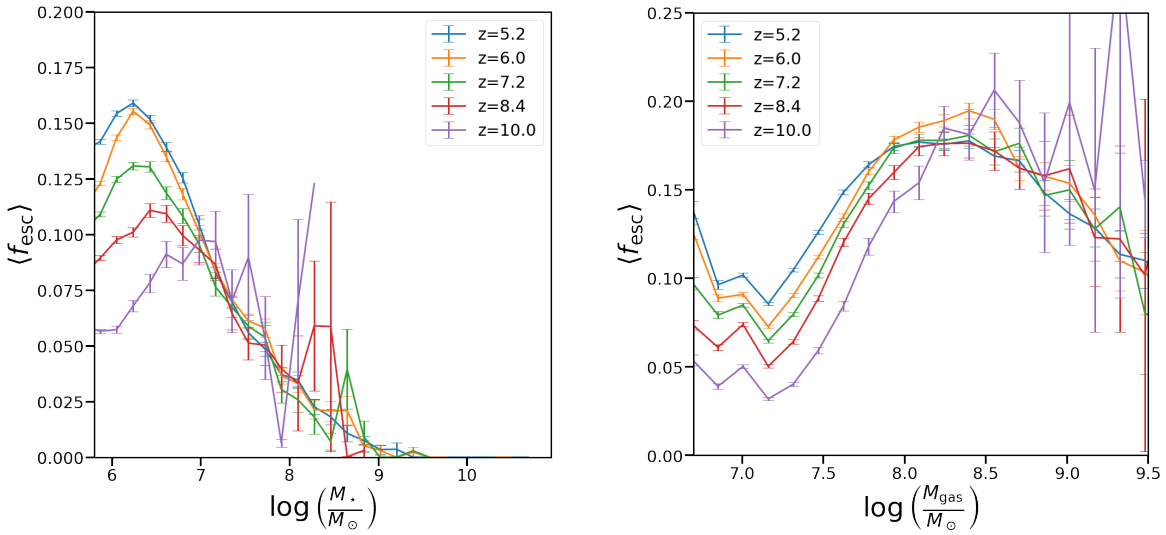

Figure 5.3: Average LyC escape fraction as a function of stellar mass (left) and gas mass (right) for a sample of redshifts. The error bars denote the statistical error of the mean.

optical depth τ_i, as N_d is negligible[2]. We clearly see major differences in the two modes of escape.

In region 1 on the right-hand side ionizing photons escape by forming localized channels which are often located in the central regions of galaxies, i.e. where most of the star formation is taking place. We also see by comparing to fig.5.5 that these regions strongly correlate with the regions of the highest ionizing flux. This also helps explain why this region is correlated with high column heights, given that N_S decreases with the recombination rate and hence $N_S \propto n^{-2}$. Meanwhile the density scales as $n \propto H^{-1}$ with the column height.

The LyC escape region in galaxies of group 2 on the other hand is spread over a far larger area but it is mostly surrounding the central part of the galaxies with very little to no LyC leakage in the center. When comparing to fig.5.5 we see that this mode of LyC escape shows essentially the inverse correlation between SFR and LyC escape as mode 1, i.e. the central region has the highest N_0/N_S ratio while the outskirts show little absorption. In order for the escape fractions to be large, it is therefore crucial that a significant fraction of star formation is happening on the outskirts of the galaxy as the top panels of fig.5.5 confirm. In this mode, the correlation with low column height is caused by the star formation being driven by high densities, i.e. even though the recombination rate in higher density regions is higher in the outer regions of the galaxies, it is compensated by the higher production rate of ionizing photons driven by star formation.

Finally group 3 shows properties appearing in both of these modes. However, in this regime there are limitation for leakage from the center due to low column height, as well as little star fomation in the outer regions of the galaxy. This limits the escape through both

[2]We do not show N_d here as the map would essentially be fully dark.

channels as can be seen in the bottom panel of fig. 5.4. The regions of ionizing flux are less extended than in the example galaxies of mode 2. At the same time there is less correlations of low N_0/N_S ratios and high star formation regions. Hence, this boundary region shows properties of both escape modes, but has at the same time stronger restrictions in both modes leading to an on average lower total LyC escape fraction.

When examining the first escape mode in fig. 5.4, we see that for $\log(\mathrm{SFR}) < -2.5$ the escape fraction correlates positively with SFR. However, for higher values of SFR ($\log(\mathrm{SFR}) > -2$ this trend reverses as the average escape fraction decreases with SFR. To understand this trend in more detail we examined three example halos from both of these extremes in fig. 5.6. In the low SFR sample we see that, only a few very small escape channels exist. In these channels, the absorption due to dust is negligible and the escape fraction is fully determined by the gas optical depth N_0/N_S. As the escape channels are highly localized, the deciding factor for the escape fraction is the amount of ionizing photons produced which is proportional to the SFR. On the other hand, in the upper limit sample we see that the deciding factor for the escape fraction in the central region is the dust optical depth N_0/N_d. This factor is correlated to the metallicity. At the same time, a higher metallicity content facilitates gas cooling and thus the SFR. In this case, the higher absorption due to dust out weights the higher ionizing photon production due to more efficient cooling, thus reducing the resulting escape fraction.

Note that the escape regions of the upper limit in mode 1 look similar to the structures we see in mode 2. However, in the former case, while the outer escape regions are extensive, only a small fraction of the galaxies' ionizing photons are produced in these regions thus leading to a small overall f_{esc}.

Finally, in fig. 5.7 we explore the correlation of the two escape modes with other galactic properties. For that purpose we separate the sample of galaxies into two groups: one with $\log(H/\mathrm{cm}) > 21.3$ containing mode 1 and one $\log(H/\mathrm{cm}) < 20.8$ containing mode 2. We then examine the correlation of these groups separately in relation to various galactic properties.

In the top panels we examine the dependence of f_{esc} on the galactic gas mass and metallicity. Here we see significant differences in the two groups. For small column heights on the left, the metallicity is positively correlated with the gas mass. All galaxies with significant escape fractions have higher metallicites $10^{-4} < Z < 10^{-2}$. We can thus deduce that mode 2 is characterized by low gas mass and high metallicity in addition to low column heights and SFR. In this mode gas cooling is driven by metals. This leads to the gas reaching relatively high densities despite low galactic masses and thus igniting star formation. As these galaxies contain little gas, photons can escape despite the relatively low columns heights.

In the group containing galaxies with large column heights, there is very little correlation between gas mass and metallicity. We further see that metallicity in this mode is negatively correlate with f_{esc}. This is especially true for higher M_gas. This reflects the fact that escape of higher SFR galaxies is bound by dust absorption as we have discussed previously. Interestingly, there is no bound to the f_{esc} by gas mass. This again reflects the fact the the LyC escape in more massive galaxies is not limited by gas but dust. Thus,

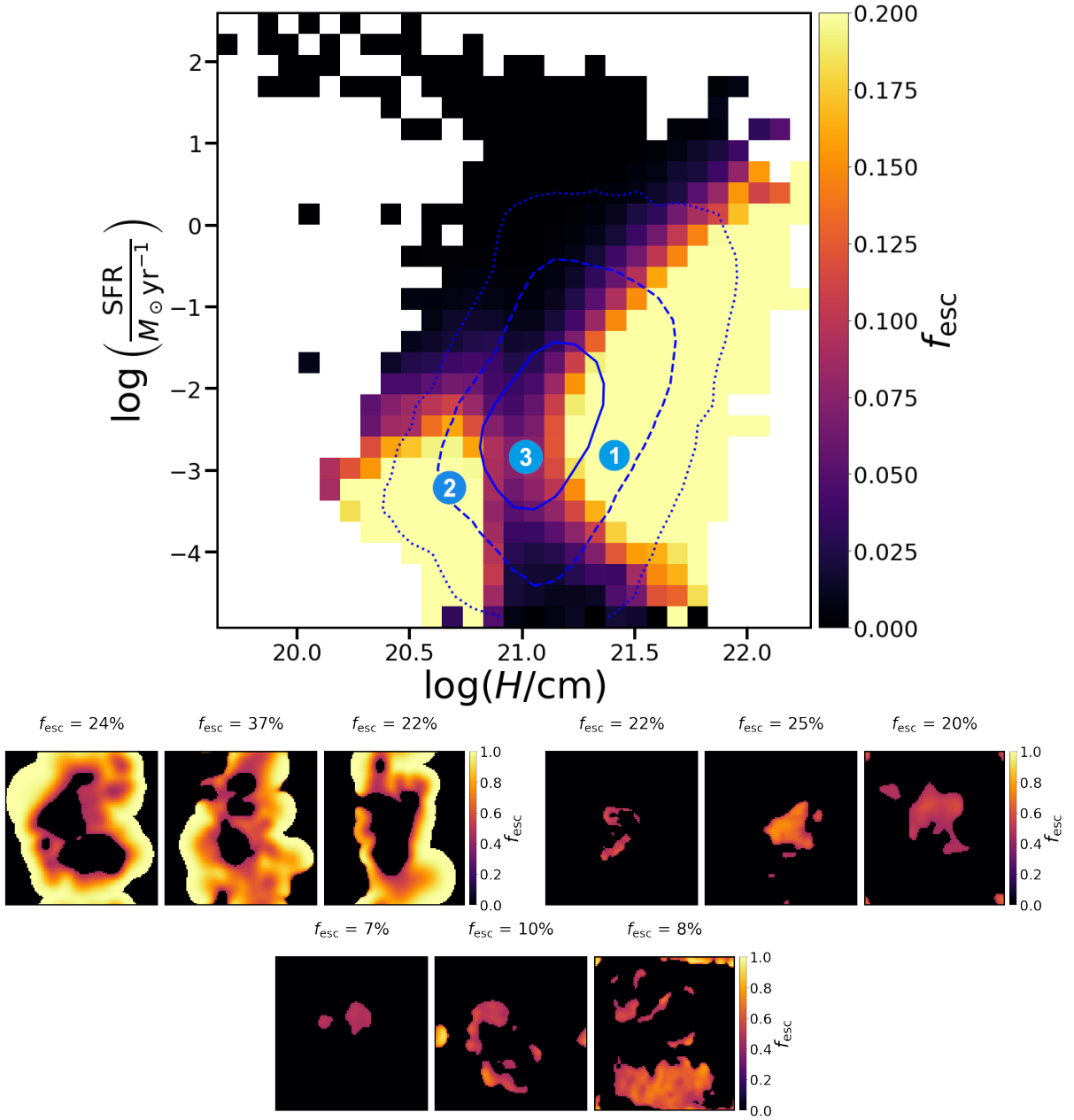

Figure 5.4: Top: Average escape fraction as a function of column height and star formation rate. The contours represent the distribution of galaxies as described above. Bottom: Escape fraction distribution for three example galaxies from each of the three regions indicated by numbers. The left-hand galaxies are sampled from the second mode (region2), the right-hand sample from the first mode (region 1) and the bottom sample to the boundary region 3.

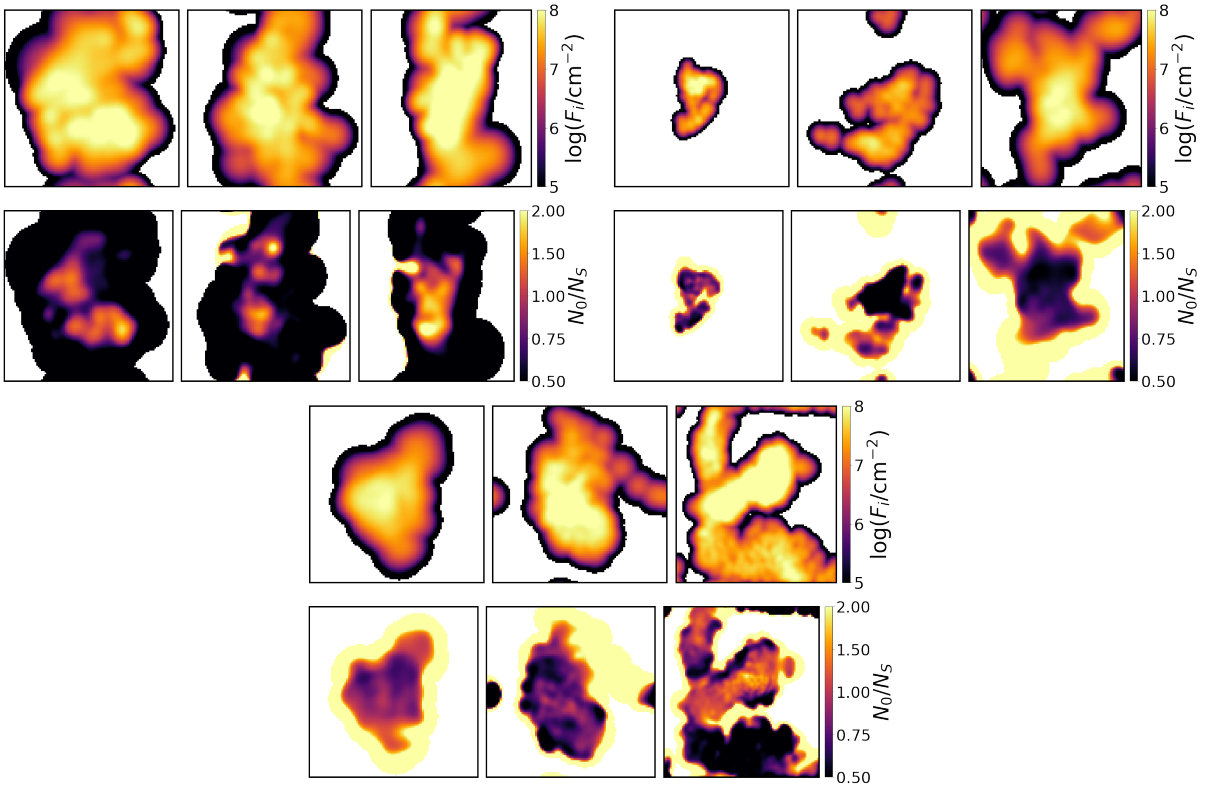

Figure 5.5: Top: Ionizing flux for the sample galaxies in the two modes in fig. 5.4. The left-hand sample corresponds to mode 2 and the right-hand sample to mode 1. Bottom: Ratios between the column density N_0 and the highest ionizable column density N_S for the same galaxies.

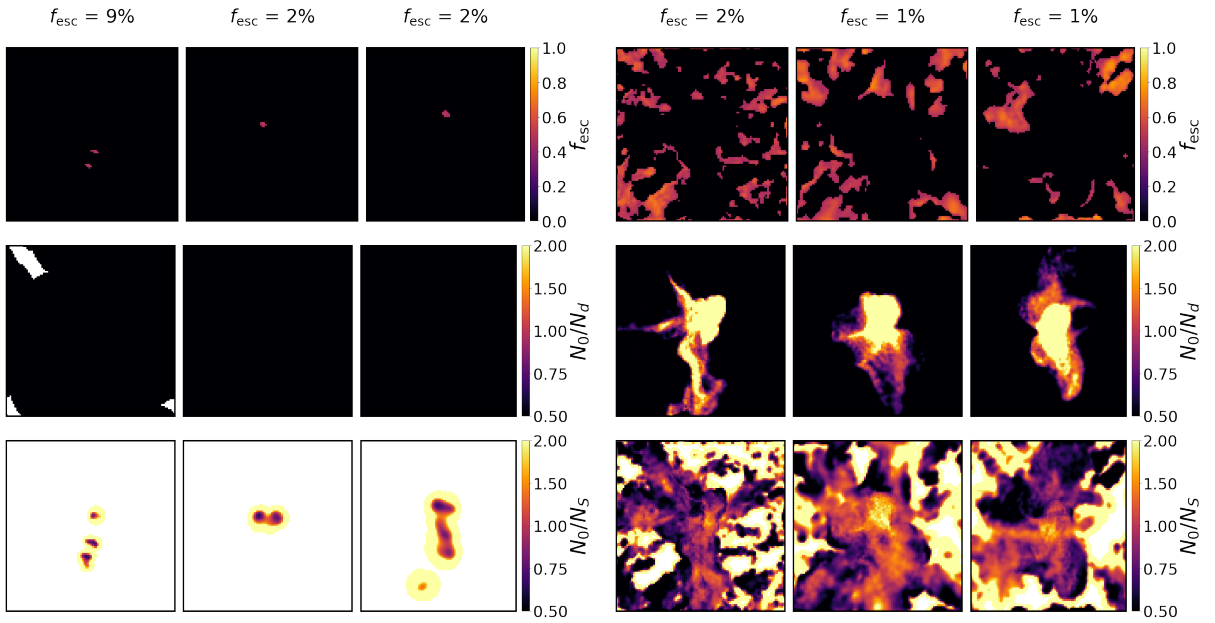

Figure 5.6: Three sample galaxies from the lower limit of mode 1 (left) and the upper limit (right). From top to bottom we depict the escape fraction, the optical depth of dust N_0/N_d and of gas N_0/N_S.

massive, metal poor galaxies tend to have sufficient star formation to form escape channels.

When examining the distribution of galaxies as a function of stellar mass and SFR, we see that both groups mostly follow the main sequence. However, the group with low column heights has a higher scatter in SFR at a fixed $M_\star$ for $M_\star > 10^7 M_\odot$. This is likely caused by both old, mostly quenched galaxies with little feedback as well as efficiently cooling high SFR galaxies having small column height falling into this group. The sequence in the second group extends to approximately one order of magnitude higher SFR and $M_\star$. The reason is that large galaxies are usually found at lower redshifts and are usually more enriched by metals. This facilitates their cooling resulting in lower column heights. As these galaxies mostly follow the main sequence we find that the bound in SFR that was seen in fig. 5.4 also introduces a limit on the stellar mass resulting in only galaxies with $M_\star \lesssim 10^8 M_\odot$ being significant LyC leakers.

The group with $\log(H/\mathrm{cm}) > 21.3$ contains LyC leakers up to higher $M_\star$ as galaxies with $M_\star \approx 10^8 M_\odot$ have average LyC leakage of $f_{esc} \approx 10\%$. As discussed previously at the upper stellar mass end the escape of LyC photons is mainly limited by dust absorption. Since, higher metallicities correlate with more efficient cooling and thus lower column heights, galaxies with higher H tend to have lower metallicities and thus less dust absorption. The reason why the escape fraction is constraint for higher stellar masses but not gas masses is likely caused by higher stellar mass galaxies often containing a significant amount of older stellar population which have enriched the ISM with metals thus limiting the escape of LyC photons.

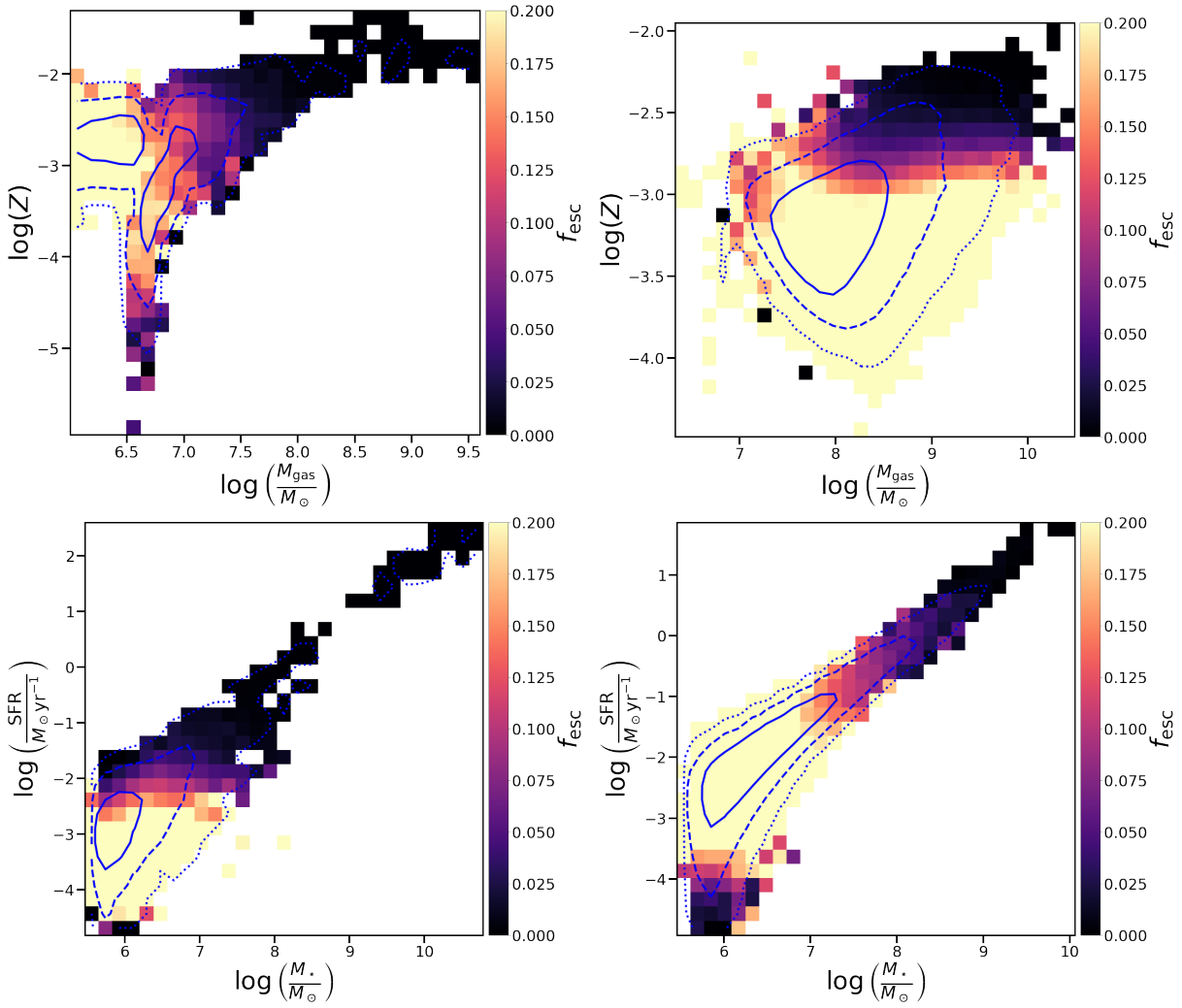

Figure 5.7: Top: Average escape fraction as a function of metallicity and galactic gas mass for galaxies with $\log(H/\mathrm{cm}) < 20.8$ (left) and $\log(H/\mathrm{cm}) < 21.3$ (right). Bottom: Average escape fractions as function of stellar masses and SFRs selected according to the criteria.

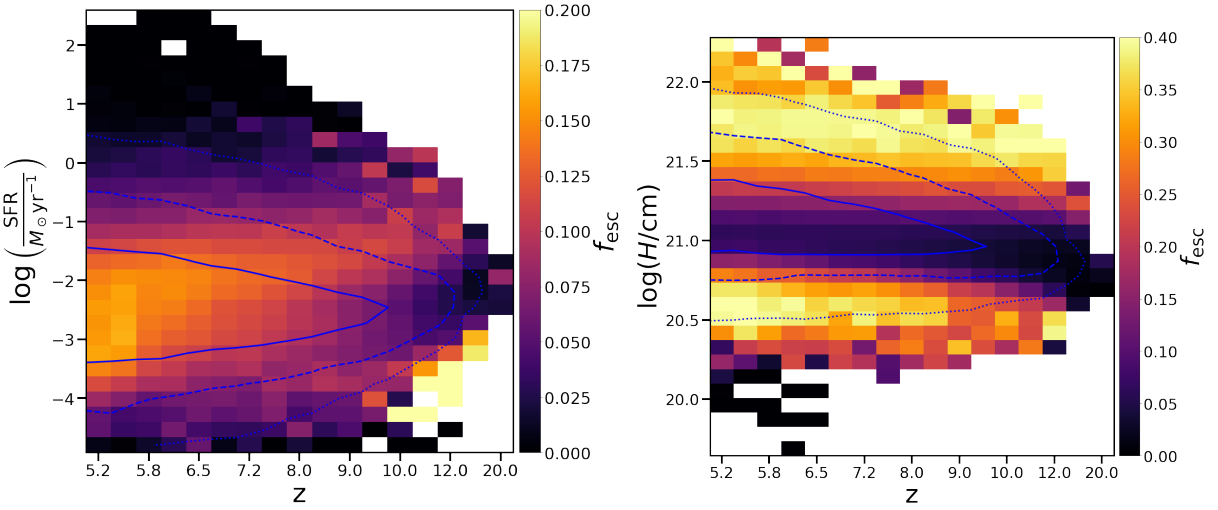

Figure 5.8: Evolution of the escape fraction as a function of redshift and SFR (left) as well as column height (right).

5.4 Redshift evolution

Based on the findings discussed in the previous section, we examine here the redshift evolution of $f_{\rm esc}$. For that purpose, we depict $f_{\rm esc}$ as a function of the SFR and redshift as well as column height and redshift in fig. 5.8.

In the left-hand plot of fig. 5.8 we see a trend of increasing $f_{\rm esc}$ with SFR, showing a very similar pattern as with $M_\star$ in fig.5.2. The reason for this trend is that at higher redshifts the metallicity of galaxies tends to be lower and hence cooling and star formation over a wide area as we saw in escape mode 2 does not occur frequently. Therefore, most galaxies leak LyC photons through the mechanism for mode 1. In this mode the lower bound is given by low star formation and therefore galaxies with higher SFR tend to be LyC leakers. Additionally, we saw that the upper SFR bound for LyC leakage in this mode is caused by dust absorption which is also reduced at high redshifts due to low metallicity.

This behaviour is further confirmed by the right-hand plot of fig.5.8 where the trends in $f_{\rm esc}$ with columns height show that, the low H mode of LyC leakage decreases in amplitude with increasing redshift while the opposite is true for the high H mode.

As a result, the LyC escape fraction decreases with increasing redshift on average due to less massive galaxies not leaking photons through the process of mode 2. Even though leakage through mode 1 for massive galaxies is enhanced at high redshifts, their abundance in the early Universe is too low, to compensate for the decrease in mode 2 leakage.

5.5 Fitting model

As large scale simulations often do not have the resolution to accurately model the process of radiation escape, the accuracy of future large scale cosmological modelling of reionization

can be improved by including a more accurate modelling of the LyC escape. In this section we therefore develop a fitting functions which allows to predict the escape fraction based on a few macroscopic properties of galaxies.

In order to model the escape fraction we use a polynomial fitting method. We initially used three parameters namely the stellar mass of the galaxy $M_\star$, its gas mass $M_{\rm gas}$, the Metallicity Z and the redshift z. We used a quadratic model and found that there is little change in the accuracy when increasing the number of parameters beyond seven. We also found that metallicity does not appear in the best fit model. The best fitting formula is given by

$$\begin{aligned}\tilde{f}_{\rm esc} =& 0.1197 M_{\star,\log}^2 + 0.3737 M_{\rm gas,log}^2 - 0.4676 M_{\star,\log} M_{\rm gas,log} \\ & - 0.0019 M_{\rm gas,log} z + 1.8589 M_{\star,\log} - 2.5041 M_{\rm gas,log} + 3.5620.\end{aligned} \tag{5.17}$$

Hereby, the masses are given in logarithmic units i.e. $M_{\rm x,log} := \log_{10}(M_x/M_\odot)$ and $\tilde{f}_{\rm esc}$ is the unconstrained estimate for the LyC escape fraction. However, some of the values of the unconstrained estimate are below 0 or above 1 and hence outside the physically possible range. These results should then be set to the lower and upper bound respectively. Finally, since only a few galaxies in our sample have high stellar masses of $M_{\star,\log} > 8.5$ the estimates in that region are likely to be inaccurate. Indeed the unconstrained estimate $\tilde{f}_{\rm esc}$ predicts high escape fraction values in the high stellar mass range and hence does not match our findings in fig. 5.4. We therefore artificially set the $f_{\rm esc}$ value to 0 for galaxies with high stellar masses. ($M_{\star,\log} > 8.5$). Therefore the resulting escape fraction is given by

$$f_{\rm esc} = \begin{cases} 0 & \tilde{f}_{\rm esc} < 0 \text{ or } M_{\star,\log} < 8.5 \\ 1 & \tilde{f}_{\rm esc} > 1 \\ \tilde{f}_{\rm esc} & \text{otherwise} \end{cases} \tag{5.18}$$

In order to determine the accuracy of the model in predicting individual escape fractions we selected a subsample of galaxies, not used for the fitting in order to avoid problems due to over-fitting. As a measure for this accuracy we used the average relative deviation

$$r = \frac{1}{N_{\rm test}} \sum_{i=1}^{N_{\rm test}} \frac{|f_{\rm esc,pred},i - f_{\rm esc,i}|}{f_{{\rm esc},i}} \tag{5.19}$$

with $f_{{\rm esc,pred},i}$ and $f_{{\rm esc},i}$ being the predicted and modelled $f_{\rm esc}$ of the i-th galaxy respectively. $N_{\rm test}$ is the number of test galaxies. We only used galaxies with $f_{\rm esc} > 0.01$ for this measure is not useful for $f_{\rm esc}$ approaching 0. We find a value of $r \approx 1.2$ i.e. the average estimation error is on the order of a factor of 2. As such the accuracy of predicting the escape fraction of a single halo is limited. However, for large scale studies where the statistical distribution of the escape fraction is more important this model performed significantly better. The average escape fraction obtained with the fitting formula is $\bar{f}_{{\rm esc,pred},i} = 0.121 \pm 0.086$ with the modelled escape fraction being $\bar{f}_{{\rm esc},i} = 0.117 \pm 0.1334$.

In fig. 5.9 we analyze how well applying the fitting formula is able to reproduce the behaviour of $f_{\rm esc}$ in relation to various properties of the galaxy. For this purpose we

reproduced the left-hand plot of fig. 5.8, the main plot of fig. 5.4 as well as fig. 5.3 using the fitted escape fraction.

In the top-left plot we see that the evolution of the escape fraction with redshift is successfully reproduced. However, the strong color gradients that are seen in fig.5.8 are smoothed out. The reason for this likely lies in the optimization process used to find the fitting formula. Since, the mean squared error was used for optimization, large gradients in the fitting function were disfavored as they led to large errors for the outer mass ranges.

On the top-right we see that the fitting formula is able to successfully predict the bimodality in the escape fraction. However the boundary between the two modes is less pronounced. This is likely also caused by the smoothing effect of the optimization process of the fitting function discussed above.

Finally, by comparing fig.5.3 to the bottom row of fig.5.9 we see that the fitting formula is able to reproduce all important trends. Namely, the decrease in peak escape fraction with redshift and the approximate locations and values of the peaks. We also reproduce both the minima and maxima in the dependence of $f_{\rm esc}$ on $M_{\rm gas}$.

As we have discussed previously, we finally note that the goal of our modelling is to capture the general trends of LyC escape with galactic properties. Given the limited resolution and simplifications made in estimating the LyC flux, the absolute value predicted by the fitting formula is unlikely to be quantitatively reliable and should be scaled with a free parameter depending on the ionizing photon budget required for reionization.

5.6 Summary and Conclusions

In this work we have have applied a physically motivated model for the LyC escape fraction of galaxies to the large sample of galaxies contained in the TNG50 simulation [146, 160] to gain a better understanding of the correlation of LyC escape with galactic properties. This model is based on the idea that the escape of LyC photons is inhibited by two optical depths: one given by the galaxies gas content and the other one is caused by dust absorption. We have post-processed $\approx$ 600 000 galaxies over a wide range of redshifts $5.2 < z < 20$.

Our main finding are:

- High redshift galaxies have two possible modes for LyC leakage
  - Mode 1 is characterized by localized ionized channels in central highly star forming parts of galaxies with large column heights. It is driven by high SFR but is limited in highly star forming galaxies by metal enrichment and the dust absorption resulting from it.
  - Mode 2 is characterized by extensive star forming regions where LyC photons escape from the outer regions of galaxies where the gas column density is particularly low. Galaxies in this mode usually have high metal contents which facilitate the cooling process of gas and thus allow the gas to collapse into a thin disc with low column height where stars can form over a wide area.

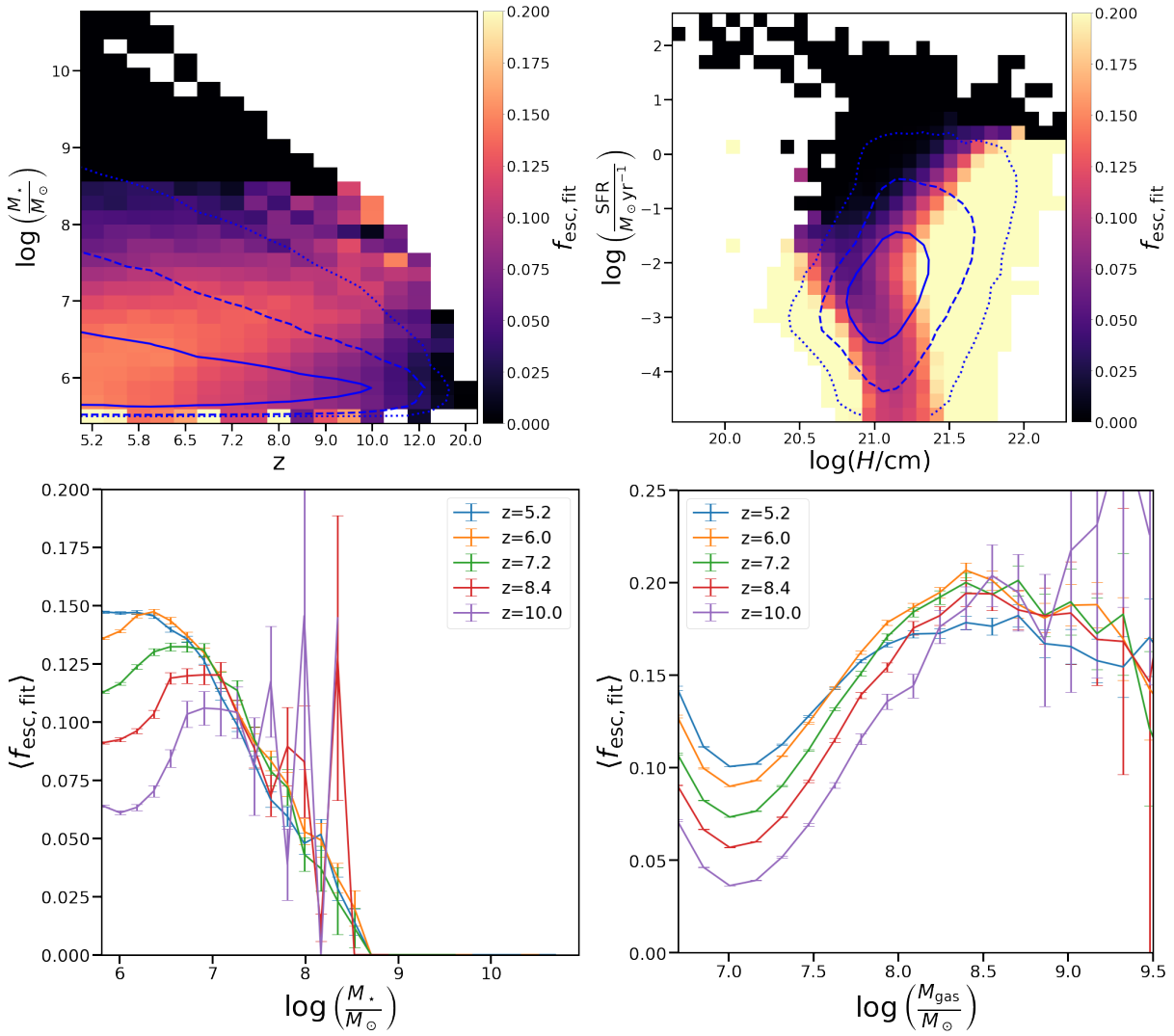

Figure 5.9: Reproductions of plots of f_{esc} as a function of galactic properties as seen in fig.5.2, 5.3 and 5.4 using the fitting formula eq. 5.18 to calculate the escape fraction.

- The average escape fraction decreases on average with increasing redshift. This is mainly due to high redshift galaxies having low metallicities and thus only leaking photons through the mechanism of mode 1.

- We have developed a fitting function for the LyC escape fraction to be used in future large scale simulations. This function is able to predict the escape fraction of a galaxy within a factor of ~ 2 in most cases. Statistically it is able to accurately capture most features of LyC leakage as a function of galactic properties that we have seen in our study.

Moving forward, there are several steps that should be taken to build on this model and further refine it. As a next step, it is of interest to model the history of reionization given our model for the production of ionizing photons and their escape. This would further allow us to set an absolute scale for the obtained LyC escape fractions.

Additionally, the physical model presented here can be further extended to take into account a more complex structure of the absorbing gas. In particular it is of interest to model the changes in optical depth due to the gas in the ISM having a two state structure.

Appendix

In order to accurately capture the escape of LyC radiation, we need to ensure that the galaxies are sufficiently resolved. In our approach, we distribute the gas particles of the TNG50 galaxy as well as their physical properties on a regular Carthesian grid before projecting all galactic properties as surface densities onto the galactic plane. To ensure the escape fraction we obtain is sufficiently resolved we applied this method to a sample of galaxies varying the grid sizes in the range of 2^3 to 502^3 in steps of 20. We used a sample of 80 galaxies. To ensure that the sample represents the range of galaxies in the TNG50 simulation, the halos were sampled from logarithmically spaced stellar mass bins ranging from the least to the most massive galaxies in the simulation.

The result of the convergence study can be seen in fig. 5.10. We see that f_{esc} rapidly converges with grid size, i.e. there is no significant change in f_{esc} for grid sizes $> 60^3$. The increase in f_{esc} for small grid sizes is explained by the smoothing out of regions containing dense gas thus decreasing its optical depth. Finally, at large grid sizes $> 150^3$ there are a few galaxies where the escape fraction is increasing while for a few others it becomes undefined. This is likely caused by numerical problems as the smoothing kernel decreases to small, numerically unstable values in some grid cells. Based on these results we have chosen 100^3 grid cells to be a reliable number to ensure that the LyC escape fraction is fully resolved within the resolution limits of the TNG50 simulation itself.

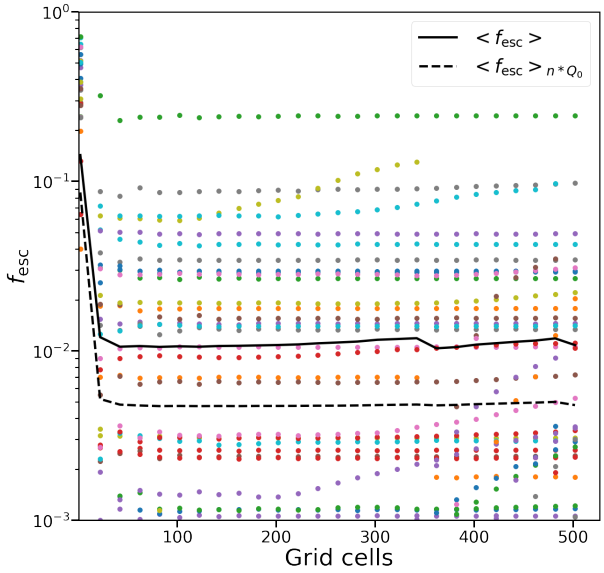

Figure 5.10: Escape fraction of a sample of galaxies as a function of the number of grid cells per dimension. We additionally depict the average escape fraction (black continuous line) and the average escape fraction weighted by the emissivity (black dashed line).

Chapter 6

Super-resolving cosmological simulations

6.1 Introduction

As we have seen in the previous chapters, one of the problems in simulations is often the large range of scales that they have to bridge. For the computation of the escape fraction the required lower end of this range is the subparcec scale of star-formation and subsequent production of ionizing photon while the simultaneously needed upper end of this range is the scale of galaxies which frequently have a size > 100 kpc. Furthermore, in order to investigate the history and topology of reionization on cosmological scales, simulations are needed that connect the scale of the smallest galaxies to cosmological volumes which are sufficiently large to accurately sample galactic populations up to the high mass range.

These problems therefore require simulations with an accurate spatial resolution over a large volume. However, if the volume of the simulation becomes larger than the number of simulated particles has to increase with the cube of the box size in order to keep the mass resolution fixed. At some point this becomes computationally unfeasible. Therefore, a compromise has to be made between mass resolution and simulation volume.

Recent advancements in Machine Learning, particularly neural networks (NN), have enabled a novel approach to address the problem at hand. This approach, called super resolution (SR), artificially generates small scale patterns into a coarser base structure. Initially developed for the super resolution of 2D images, convolutional neural networks (CNN) with a fixed loss function were used [220, 206]. However, with the introduction of generative adversarial networks (GAN) [71], the fixed loss function was replaced by an additional neural network that distinguishes the super-resolved images from the original ones. Using a multi-pass approach, two generator and critic networks were used to super-resolve 3D simulations of gases and add a temporal dimension [209, 214]. More recently, GANs in combination with 3-dimensional networks have allowed super-resolution of cosmological simulations. The first approach was used to super-resolve QUIJOTE simulations [204] with large volumes of $(1000\ \mathrm{Mpc}/h)^3$ [108]. Smaller boxed were super-resolved in

[148] and [120], where the super-resolution was applied down to smaller scales and the dark-matter particle number was enhanced instead of the density field. Finally, in [184], super-resolution algorithms were applied to fuzzy dark matter simulations.

In this work, we build on the multi-pass method of [209] in order to super-resolve gridded GADGET 3 cosmological simulations [188] of a cosmological volume of 10 Mpc^3. The output of this procedure is a simulation box with the volume of the larger simulation but with an effective mass resolution of the smaller one.

This chapter is structures as follows. In section 6.2 we introduce neural networks and in particular architectures of relevance to our project namely convolutional neural networks and generative adversarial networks. We then proceed to describe our data generation and network design in section 6.3. Our results are presented in section 6.4 and we summarize and conclude in section 6.5.

6.2 Artificial neural networks

6.2.1 Machine learning and neural networks

The idea of machine learning in general is to design a program which is able to improve its capabilities with respect to a metric for its performance by processing some input information [138].

For our purposes, it is sufficient to examine a specific type of machine learning namely artificial neural networks (ANN or simply NN). These networks map a vector of input data which is called the features vector $\vec{x}$ onto an output vector $\vec{y}(\vec{x})$. Both the in- and output vectors can also be single valued. In most cases, the features and the outputs are connected through an element wise applied non-linear function. The goal of the NN is to approximate that function.

The non-linear function is modelled through a set of intermediate layers of vectors called 'hidden layer' whereby each element of a hidden layer is determined through a linear combination of all elements from the previous layer transformed by a non-linear activation function. Hence, the values at the layer n are given by

$$\vec{L}_n = g_n(\hat{\Theta}_n \cdot \vec{L}_{n-1} + \vec{b}_n). \tag{6.1}$$

Here, g_n is the non-linear activation function of the n-th layer that is applied to each entry of the input vector, $\vec{L}_n$ and $\vec{L}_{n-1}$ are the values of the layer n and the previous layer respectively, $\hat{\Theta}_n$ is the matrix containing the weights between layer $n-1$ and n and $\vec{b}_n$ is shift (bias) vector. The goal is to tune the parameters $\hat{\Theta}$ such that the mapping corresponds to the desired output. In fig. 6.1 we depict a visualization of an example neural network with one hidden layer.

In the applications discussed here we are working with labelled datasets, i.e. for each feature vector $\vec{x}$ we have the corresponding ideal output value $\vec{y}_{\mathrm{true}}(\vec{x})$. The accuracy of the NN is improved through a process called training. The training method when using a labelled dataset is called supervised learning. Hereby, a loss function $\mathcal{L}[\vec{y}(\vec{x}), \vec{y}_{\mathrm{true}}(\vec{x})]$ can

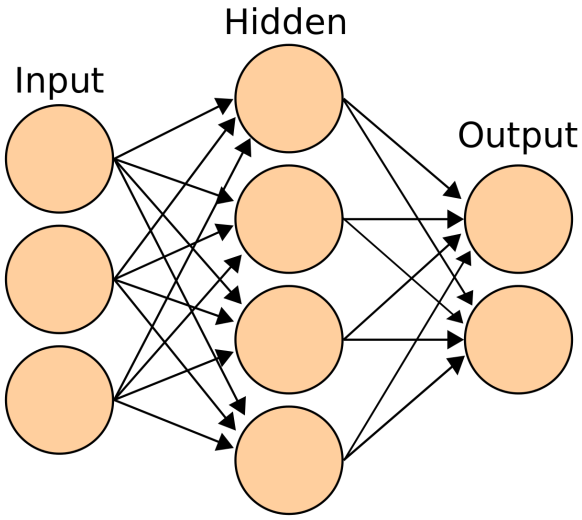

Figure 6.1: Example of a neural network with one hidden layer. The circles represent nodes and the arrows represent the weighted connection between the individual nodes. (Obtained from [1])

be defined which measures by how much the output function deviates from the expected value.

In order to train the network the loss function needs to be minimized with respect to all parameters $\hat{\Theta}_n^{i,j}$ of that network. This is achieved through gradient decent. Hereby, the values of all parameters $\hat{\Theta}$ are improved by stepping along the negative gradient of the loss function. The updated values after each steps are given by

$$\hat{\Theta}' = \hat{\Theta} - \alpha \nabla_{\hat{\Theta}} \mathcal{L}. \tag{6.2}$$

Here, $\hat{\Theta}'$ denotes the values of the parameters after the step. The hyperparameter α is the learning rate of the network. It has to be set by hand and can greatly influence the reliability and numerical stability of the minimization process. A too small learning rate can slow down the learning process such that the training process becomes computationally unfeasible. On the other hand, a large learning rate can lead to a lack of convergence as the gradient steps become large than the distance to the minimum in parameter space. Note that, unlike in e.g. linear regression, there is no guarantee that the loss function is convex with respect to all parameters. This means that gradient decent can drive the optimization into a local minimum rather than a global one. Therefore, to ensure reliability it is often beneficial to train the network several times initiating it at different values of $\hat{\Theta}$.

In order to compute the gradient in eq. 5.18, a method called back-propagation is used. The idea behind this method is that a neural network can be represented by a chain of functions

$$\vec{y}(\vec{x}) = g_N(\hat{\Theta}_N(g_{N-1}(\hat{\Theta}_{N-1}...g_1(\hat{\Theta}_1\vec{x} + \vec{b}_1)... + \vec{b}_n). \tag{6.3}$$

Here N is the number of layers in the network, excluding the input layer. This allows

to use the chain rule to calculate the derivative of the loss function with respect to each network parameter

$$\frac{\partial \mathcal{L}}{\partial \Theta_n^{ij}} = \frac{\partial \mathcal{L}}{\partial g^n} \frac{g^n}{\partial L^n} \frac{\partial L^n}{\partial \Theta_n^{ij}}. \tag{6.4}$$

$$\frac{\partial \mathcal{L}}{\partial \vec{b}_n} = \frac{\partial \mathcal{L}}{\partial g^n} \frac{g^n}{\partial L^n} \frac{\partial L^n}{\partial \vec{b}_n}. \tag{6.5}$$

Using this property the gradient is calculated iteratively based on the gradient of the previous layer.

Artificial neural networks, like any other machine learning algorithm, face two potential issues during the training process: underfitting and overfitting. Underfitting occurs when the number of free parameters is inadequate to model the non-linear relationship between $\vec{x}$ and $\vec{y}(\vec{x})$. Even after full training, the network may not be successful in completing the desired task, and more parameters need to be added to enhance the network's performance. Overfitting, on the other hand, arises when too many parameters are trained, causing the network to match the training data successfully between $\vec{x}$ and $\vec{y}(\vec{x})$. However, this doesn't generalize well to new data that wasn't used in training, as the network also captures the stochastic noise from the training data into its weights, which adversely affects its predictive power for new data.

6.2.2 Convolutional neural networks

Fully connected neural networks exhibit the property that the number of parameters, i.e. the weights, in each layer scales with the product of the number of features of the two layers it connects. When the number of input features is large, as is e.g. the case for images, if each pixel is a feature, the number of parameters can become very large. In that case, either it becomes computationally not feasible to train the network, or the network will have problems with overfitting.

Therefore, convolutional neural network (CNN) were developed [113] in order to process features structured on an n-dimensional grid such as images a specific network architecture.

The idea behind a CNN is that the correlation of data is strongest locally and decays with distance. This is particularly true for an application to super-resolution where the small scale data is almost completely determined by is local environment. In a CNN the feature-map is transformed onto the next layer through a convolution with a filter-kernel that is usually of a much smaller size than the feature-map. On a discrete space the convolution element $S(i,j)$ between one feature map I and one $m \times n$-kernel K can be expressed as [70] [1]

$$S(i,j) = \sum_m \sum_n I(i-m, j-n) K(m,n). \tag{6.6}$$

The idea is that each kernel learns to extract a different characteristics from the map (e.g. edges) which have similar structures independently from the location on the map. This

[1] Note that to ensure that the map in the next layer does not decrease by the size of the convolution kernel, feature maps are often patted by either fixed values or by imposing periodic boundary conditions.

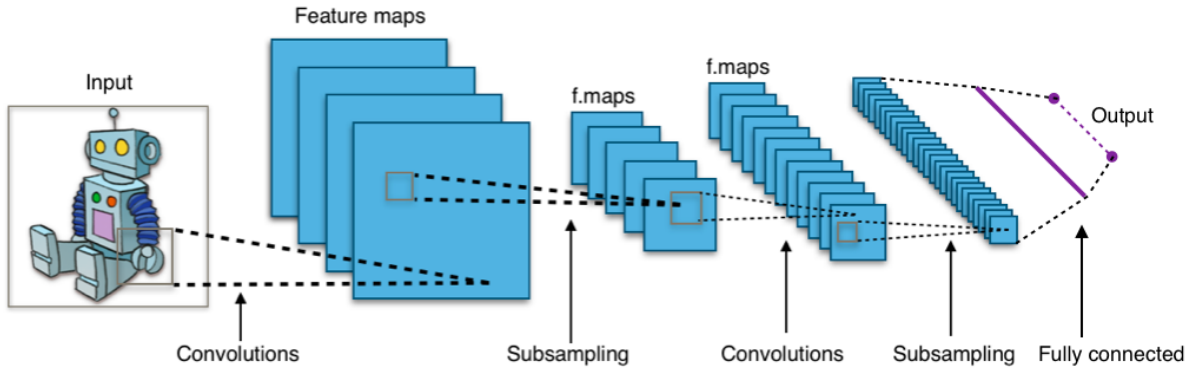

Figure 6.2: Example of a typical convolutional neural network architecture. A input map is convolved with a set of kernels to produce a set of feature maps. These maps a subsequently subsampled and processes by additional layers up to a fully connected layer which returns and output layer. Note that in case of the cnn we use the output is again a image. (Obtained from [3])

sharing of a few kernel parameters for the whole feature map (or maps) allows to extract important information from a large feature space using relatively few parameters.

However, as shown in equation 6.6, the size of the map in the next layer remains the same as the previous layer in a convolutional neural network. To reduce the output to a smaller size, such as a single value or a smaller output vector as illustrated in Figure 6.2, the feature maps must be gradually reduced in size. There are two common methods for achieving this: subsampling and pooling. Subsampling involves increasing the distance the kernel shifts after each convolution, known as the stride, such as using a stride of 2 to produce a feature map in the next layer with half the size of the previous one in each dimension. Pooling reduces dimensionality by merging neighboring data points into one, and these pooling maps can be computed by taking either the average or the maximum of each group of neighbors.

6.2.3 Generative adversarial networks

As discussed in the previous sections, each network relies on a loss function which provides a metric for the quality of a neural network. An approach to the loss function which has proven successful for generating 2D images as well as 3D data structures is the Generative Adversarial Network (GAN) [71]. Hereby the loss function is replaced by an additional network, the so called Discriminator. The main idea is to simultaneously train the two networks the generator G and a Discriminator D. The aim of G is to generate samples which are as similar as possible to samples drawn from the true data distribution. The aim of D is to distinguish whether a given sample was generated or drawn from the ground-truth distribution.

From a mathematical perspective the goal is to be able to draw samples from a distribution $p(x)$ over some space X of which we have a set of samples, i.e. the ground truth

data. For that we train a generative network $G(z, \theta_g)$ which creates samples of a posterior distribution $p_g(x)$ which we want to resemble $p(x)$ as closely as possible. To compare samples drawn from $p(x)$ to the generated samples we use the discriminator $D(x, \theta_d)$ which is trained to distinguish generated and real samples. Its training objective is to assign values close to 1 to samples from the true distribution and close to 0 for outputs of the generator. The goal of the generator is however, is to fool the discriminator network. The value function assigned to this network is given by

$$V(D, G) = \mathbb{E}_{x \sim p(x)} [\log D(x)] + \mathbb{E}_{z \sim p_z(z)} [\log(1 - D(G(z)))]. \tag{6.7}$$

Here the first term corresponds to the ground truth data that should be assigned a high value by the discriminator and the second term is corresponds to the value of the sample of the generator which should be assigned a low value by the discriminator. Hence in order to optimize both network, a saddle point of the value function

$$\min_G \max_D V(D, G) \tag{6.8}$$

needs to be found.

The procedure of one training step in the training process of a GAN goes as follows [71]:

1. Draw a sample z from the prior distribution $p_z(z)$
2. Map this sample onto an element of the posterior distribution $p_g(x)$ using the generator network $G(z, \hat{\Theta}_g)$ with x being an element from the same space as the ground truth data.
3. Propagate this generated sample as well as a ground truth element through the discriminator $D(x, \theta_d)$ to predict whether a given element is generated or real.
4. Take the gradient of the loss function 6.7 with respect to the parameters $\hat{\Theta}_d$ of the discriminator network and update these. (Repeat this procedure k times)
5. Propagate a prior sample again through both networks but this time update the generator parameters $\hat{\Theta}_g$ by taking the gradient of the function

   $$\log D(G(z)) \tag{6.9}$$

   with respect to these parameters with the goal of maximizing it. This function was chosen because it does not saturate as quickly as $\log(1 - D(G(z))$, given that as the discriminator gets better this function approaches negative infinity rather than 0. It nonetheless results in the same fix point after training [71].

The explicit formulation of the training algorithm is described in algorithm 1 whereby the last step was changed as compared to [71] using the recommendation of [8] to avoid vanishing gradients in case of an overly confident discriminator.

Algorithm 1: Algorithm to train a GAN using a stochastic gradient descent (SGD) minimization. Hereby, each update is performed on a sample of the training data called minibatch to increase the speed of the training process.

for *number of training iterations* **do**

  for *number of discriminator updates per generator update* **do**

    - Sample minibatch of m prior samples;
    - Sample minibatch of m ground truth samples;
    - Update the discriminator by ascending its stochastic gradient:

$$\nabla_{\hat{\Theta}_d} \frac{1}{m} \sum_{i=1}^{m} \left[\log D\left(x^i\right) + \log\left(1 - D\left(G\left(z^i\right)\right)\right) \right]$$

  end

    - Sample minibatch of m prior sample ;
    - Update the generator by ascending the loss function

$$\nabla_{\hat{\Theta}_d} \frac{1}{m} \sum_{i=1}^{m} \log D\left(G\left(z^i\right)\right)$$

end

As presented in [8] GANs are designed to minimize the Jensen-Shannon divergence between a distribution we are trying to approximate $p(x)$ and a generator distribution $p_g(x)$. The JS-divergence between these two distributions is defined as

$$\mathrm{JSD}(p(x)||p_g(x) = \frac{1}{2}\mathrm{KL}(p(x)||p_a(x)) + \frac{1}{2}\mathrm{KL}(p_g(x)||p_a(x)) \tag{6.10}$$

with the average distribution being the defined as $p_a(x) = \frac{p(x)+p_g(x)}{2}$ and the Kullback-Leibler divergence

$$\mathrm{KL}(p(x)||q(x)) := \int_{\chi} p(x) \log \frac{p(x)}{q(x)} \mathrm{d}x. \tag{6.11}$$

The fact that GANs minimize the JSD divergence seems to have the advantage that the disadvantages due to the asymmetry of the KL divergence are accounted for [2].

One problem with GANs is that they are difficult to stabily train since if the discriminator becomes too good too early it becomes impossible to train the generator.

To combat this problem the Wasserstein GAN (WGAN) was developed [9]. Hereby, a critic network replaces the discriminator network with the main difference being that the critic networks provides a score for the quality of the data rather than a binary classification into real and generator, This ensures that the network can be stably trained regardless whether the quality of the critic surpasses that of the generator.

6.3 Methodology

6.3.1 Generating the training data

The goal is to super-resolve gridded cosmological simulations. We initially use the MUSIC software [80] to generate the initial conditions for simulations of a $(10\mathrm{cMpc}/h)^3$ box at redshift 100 at various resolution levels, namely 128^3, 256^3 and 512^3 particles per box. In order to ensure that the simulations represent the same cosmological structures at each step in resolution, the same random seeds for the overlapping scales to create the initial conditions was used. We run these simulations up to a scale factor of $a = 0.3$ i.e. a redshift of approximately 2.33.

Afterwards, the particles of these simulations are gridded onto a 512^3 regular grid. Note here that all the simulation use the same grid regardless of their mass resolution. The reason for this choice of gridding is that voxels with a high overdensity, i.e. containing many simulation particles, are already well sampled in the low resolution (LR) simulation. By using a coarser grid for the lower resolution simulation we would artificially destroy information in these well sampled areas.

The above process is repeated for another simulation run with different seeds to create test data. This second set of simulation runs is not used for training but only to evaluate

[2] However as pointed out in [115] the asymmetry of the KL divergence can actually be desirable for optimal learning

the result after the training process. This is done to test whether the trained network is able to generalize to new input data.

The training simulation is then cut into 512 training tiles of size 64^3. These are than rotated and flipped such that the effective number of training tiles we get from one simulation run is increased tenfold to 5120.

Additionally all tiles are scaled by the function

$$x_{\text{scaled}} = \frac{\ln(x + \epsilon)}{25} \tag{6.12}$$

with x being a voxel value (i.e. a dark matter density at a given location) and $\epsilon = 10^{-9}$ a regularization parameter to avoid infinite values at zero valued voxels. This procedure brings all the voxel values into a range of approximately $[-0.9; 0]$. It is necessary for the values to be on similar scales since otherwise the network would only be conditioned on very few exceptionally high values due to the low dynamic range individual network layers are build for.

6.3.2 Network architecture

In this work we base our network design on the ideas presented in [209], i.e. we use a multi-pass approach to super-resolution. The goal hereby is to decrease the number of required parameters given that this approach requires 2-dimensional kernels. Meanwhile direct processing would require 3-dimensional kernels. We use two generator 2D CNNs to super resolve the simulation. One of the networks has the task to super resolve slices along one axis and the other network receives the output of the first generator turned by 90 degrees and super resolves the input along the other axis. Thereby it is ensured that discontinuities and other errors which might emerge on the boundaries between two slices during the first pass (because these boundaries are not seen by the first network) are subsequently fixed by the second network.

For the generator CNNs we use a residual architecture [84]. This means that the low resolution input is passed directly to the output. The output of the convolutional layers is than added to the low resolution input in the last step. This can be expressed as

$$G(x) = x + \varphi(x), \tag{6.13}$$

with $G(x)$ being the output of the generator and $\varphi(x)$ the mapping of x through all the convolutional layers.

The use of such an architecture is reasonable if the output of the generator can be expressed as a combination of a unity mapping and a small perturbation around it. This is indeed the case for super-resolution tasks where the individual voxels are only slightly changed.

In the WGAN approach we use again CNNs for the architecture of the critic networks. However, since the WGAN has to map a given input slice onto a real number we need a

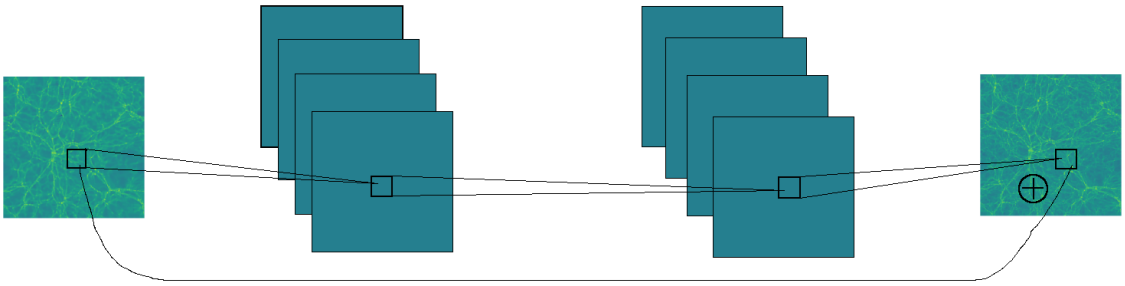

Figure 6.3: Visualization of one of the two generator neural network used in our model. The input is a 2D-slice of the low-resolution simulation and the output is a slice of the super resolved result. Note that this network adds the low resolution input at the end, i.e. the goal of the network is to only learn the difference between the low and high resolution simulations.

final layer with a single valued output to calculate the loss. The loss function for the critic network C, following [9], is given by

$$\mathcal{L}_{\text{crit}}(y) = C(y_{\text{SR}}) - C(y_{\text{hr}}) + \lambda(||\nabla_{\bar{y}} C(\bar{y})||_2 - 1)^2. \tag{6.14}$$

Here $y_{\text{SR}} = G(x)$ is the super resolved slice, y_{hr} is the ground truth i.e. the corresponding slice in high resolution (HR) and C is the function representing the critic network. Additionally we have introduced a gradient penalty term as it was defined in [76] which is required to enforce that the critic is a 1-Lipschitz function as described in [9]. The gradient of this term is taken with respect to an interpolated image $\bar{y}$ which is defined as

$$\bar{y} = (1 - \alpha) y_{\text{SR}} + \alpha y_{\text{hr}} \tag{6.15}$$

with $\alpha \in [0; 1]$ being a random interpolation parameter drawn anew for each slice.

6.3.3 Training process

We applied two different methods of network training. In both cases we use a multi-pass approach. However, in the first case we use only the generator networks and keep the loss function fixed to be a linear combination of l_p norms. Meanwhile in the other approach we use GANs, whereby we train the two critics as described in the previous section.

During the training process a 64^3 3D tile is passed to the first generator network as a batch of 64 individual 64^2 slices. The quality of the processed slices is than evaluated with the loss function. The gradient of the loss with respect to the network parameters is subsequently used to update the network parameters.

The tile is then rotated by multiples of 90 degrees and these are passed as a batch. These are then sliced along another axis by the second generator network. The parameters of the second network are subsequently updated in the same manner.

The networks are usually trained for 24 hours which results in approximately 150 iterations through the full training set of 5120 tiles.

When using l_p losses the training process is more straight forward than in the WGAN approach. Here the loss function is given by

$$\mathcal{L}_{\text{gen}} = \lambda_1 ||y_{\text{SR}} - y_{\text{hr}}||_1 + \lambda_2 ||y_{\text{SR}} - y_{\text{hr}}||_2 + ..., \tag{6.16}$$

whereby arbitrary many additional l_p losses can be added together. The parameters λ_n fix the relative contributions of the individual terms. Currently an l_1 and an l_2 loss function were tested individually as well as in combination with each other and with an additional l_∞ loss. The later was introduced to emphasize the accurate capture of peaks in the overdensities.

As described in the previous section, the main difference when using the WGAN approach is that we now do not write down the loss function explicitly. Instead the loss function is another network that is trained simultaneously with the generator network. Its goal to assign a high value for a slice which is very similar to a slice taken from a high resolution simulation and a low value to a slice which is super-resolved with the generator network.

Since in the WGAN approach there is never a problem with vanishing gradients, it is reasonable to make sure that the critic network is always ahead of the generator which can be achieved by doing several critic updates for each generator update. In the work presented here the critic parameters were updated five times for each time we updated the generator. Hereby we followed the method of [9]. We also tried out doing one and ten critic updates per generator step with worse results obtained for the one step approach and no improvement seen in the ten step approach over the fiducial five step approach.

The loss function for the generator networks is given by

$$\mathcal{L}_{\text{gen}} = -C(G(x)) \tag{6.17}$$

The training process itself is performed in the same way as described above for the l_p loss with the only difference that now we also update the critic network. However due to multiple failures of the training process in the multi-pass approach, we are now trying to stabilize one single pass. Hence we only use one generator and one critic for now.

6.4 Results

6.4.1 l_p results

We did three training runs with the following parameters

1. Using only the l_1 loss with prefactors set to $\lambda_1 = 0.5$, $\lambda_2 = 0$ and $\lambda_\infty = 0$

2. Using only the l_2 loss with the prefactors set to $\lambda_1 = 0$, $\lambda_2 = 10$ and $\lambda_\infty = 0$

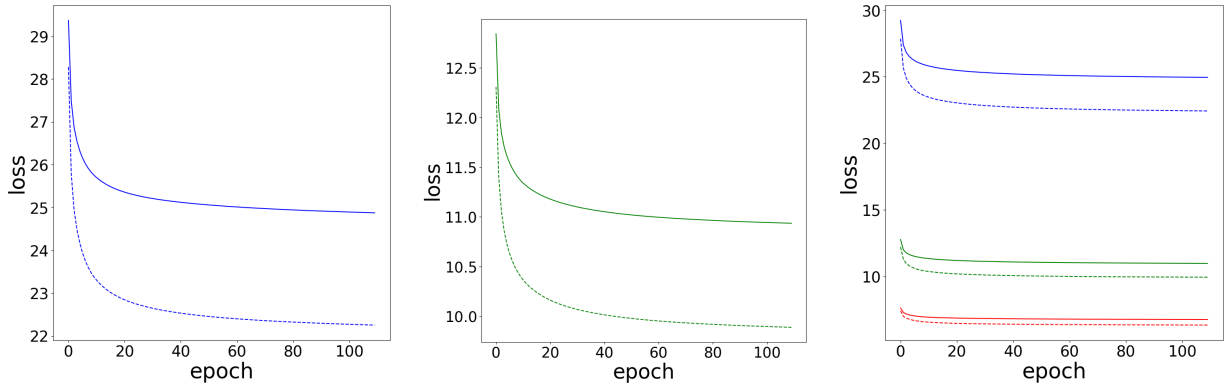

(a) Only l_1 loss (b) Only l_2 loss (c) l_1, l_2 and l_∞ loss

Figure 6.4: The average loss of the generators as a function of training epoch for the different l_p losses. The l_1, l_2 and l_∞ loss are denoted in blue, green and cyan respectively. The solid lines represent the loss of the first generator and the dashed the second.

3. Using an l_1, l_2 and an l_∞ loss with the parameters set to $\lambda_1 = 0.5$, $\lambda_2 = 10$ and $\lambda_\infty = 50$.

The prefactors were chosen in such a way that the gradients obtained from the individual contributions of the losses are of approximately the same order of magnitude.

The average loss function of a sample as a function of the training epoch is shown in fig. 6.4. It can be seen that the loss function is monotonously converging in all three configurations. As the curves stay relatively flat after approximately the first 40 epoch, a training session longer than 24 hours is not expected to significantly improve the results.

In fig. 6.5 we see the total average gradients for the different runs which were calculated as

$$g_{l_n} = \sum_\theta \left| \frac{\partial \mathcal{L}_{l_n}}{\partial \theta} \right|, \tag{6.18}$$

with θ being the parameters of the generator network and $\mathcal{L}_{l_n}$ being the loss function corresponding to a given l_n-norm. This means that this quantity expresses how strongly a given term in the loss function affects the parameters of the network. Plot c of fig. 6.5 illustrates that the choice of parameters was successful in keeping the gradients on a similar order of magnitude. The fact that the gradients decrease as a function of epoch confirms that the training process is indeed converging. However, the gradient is not approaching zero as there are statistical variations within the set of training batches.

In fig. 6.6 we depict a sample slice taken from the simulation at low and high resolution as well as the super-resolved results. The plots have a logarithmic color scale which is kept the same for all images. It is evident that the super-resolution process strongly improves the low-resolution input regardless of what loss function is used and all super-resolved images look strikingly similar to the ground truth. It even seems that, at very close inspection, the numerical artifacts (the faint stripes) in the underdense regions of the super-resolved

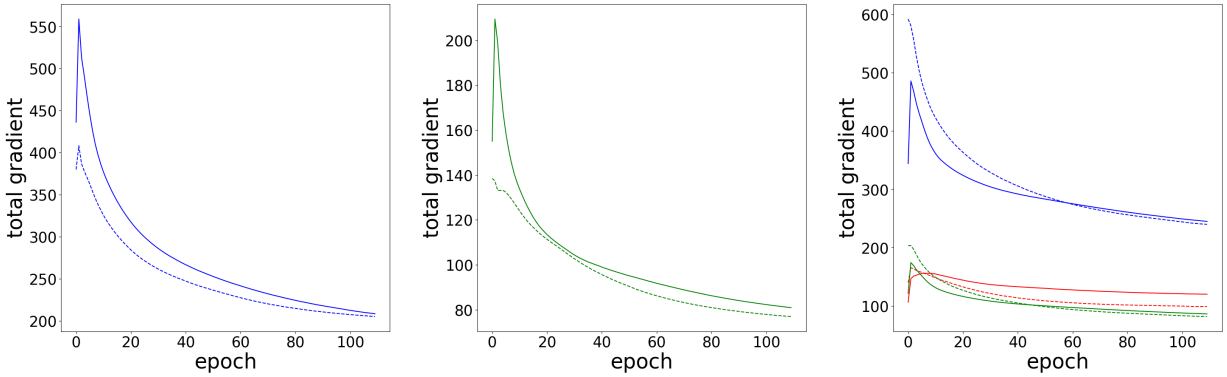

(a) Only l_1 loss (b) Only l_2 loss (c) l_1, l_2 and l_∞ loss

Figure 6.5: As fig. 6.4 but for the average total gradient

images are even less pronounced than in the high resolution. Visually there does not seem to be any noticeable differences between the three different choices of loss functions.

However, figure 6.7 paints a significantly different picture of the success of the super-resolution process. Depicted therein is the evolution of some of the statistical characteristics of the simulation box as a function of training epoch. Namely the mean, median and maximal voxel value as well as the one sigma scatter of values rescaled to the full dynamic range. The plots imply that the characteristics of the super-resolutions almost always deviate further from the ground truth value than those of the the low-resolution simulation. The only exception is the median in which case all the super-resolution methods outperform the input with no strong difference between the individual choice of loss function. It is also interesting to note that there does not seem to be any noticeable improvement of the characteristics with increasing epoch. The average and the median vary by a small amount. Meanwhile the maximum and the standard deviations fluctuate strongly but do not improve. The reason for this poor performance might be the logarithmic scaling in the preprocessing of the input tiles. The scaling procedure maps the very large dynamical range of the simulation onto a small range thereby obscuring the significance of the large dynamic range. The large error in the maximum value could also be explained by its singular occurrence within the simulation box. Since there are very few training tiles with such high value, the network has few samples to learn from. Nonetheless, the addition of an l_∞ loss should ensure that these exceptional overdensities are taken into account. However, this does not seem to be the case as the network that includes the additional l_∞ norm performs poorest on this measure.

Next in figure 6.8 we plotted the distribution of the relative density values as well as the relative deviations from the ground truth. These values were calculated by dividing all the values in a simulation by its average density and then binning the voxel values in bins with logarithmic width. The most noticeable difference of the super-resolved simulations as compared to both the low and high resolution simulations is the cut-off at scales of $\sim 10^{-3}$ to 10^{-4}. This however does not pose a significant problem as it only relates to a

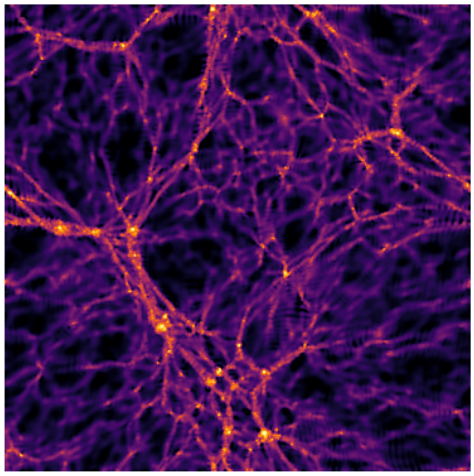

(a) Slice of the input simulation (256^3)

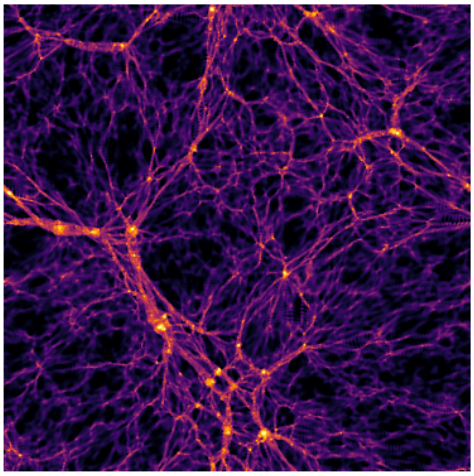

(b) Slice of the ground truth (512^3)

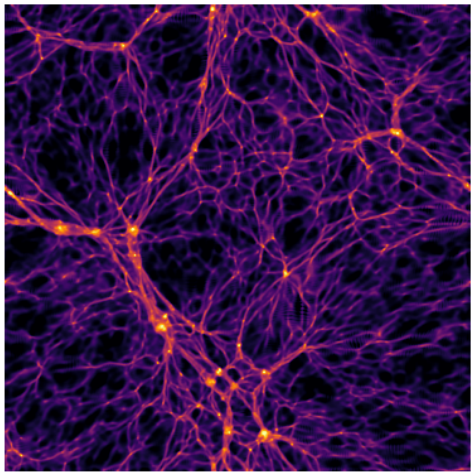

(c) Super-resolved using the l_1-loss

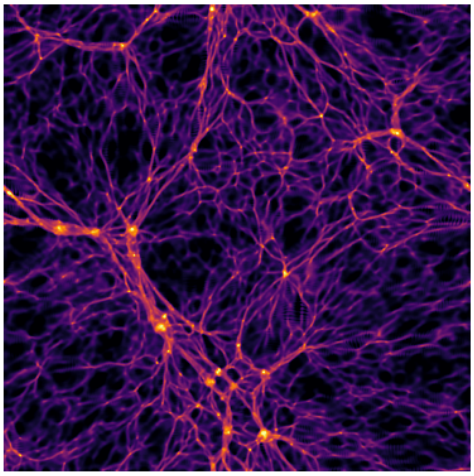

(d) Super-resolved using the l_2-loss

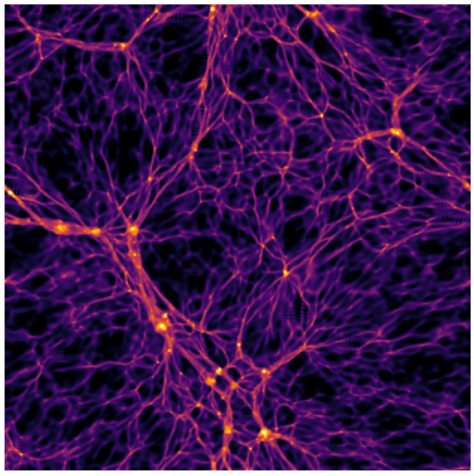

(e) Super-resolved using l_1, l_2 and l_∞ losses

Figure 6.6: Visualization of the super-resolved simulations together with the high resolution ground truth and the low resolution input simulation on a logarithmic color scale.

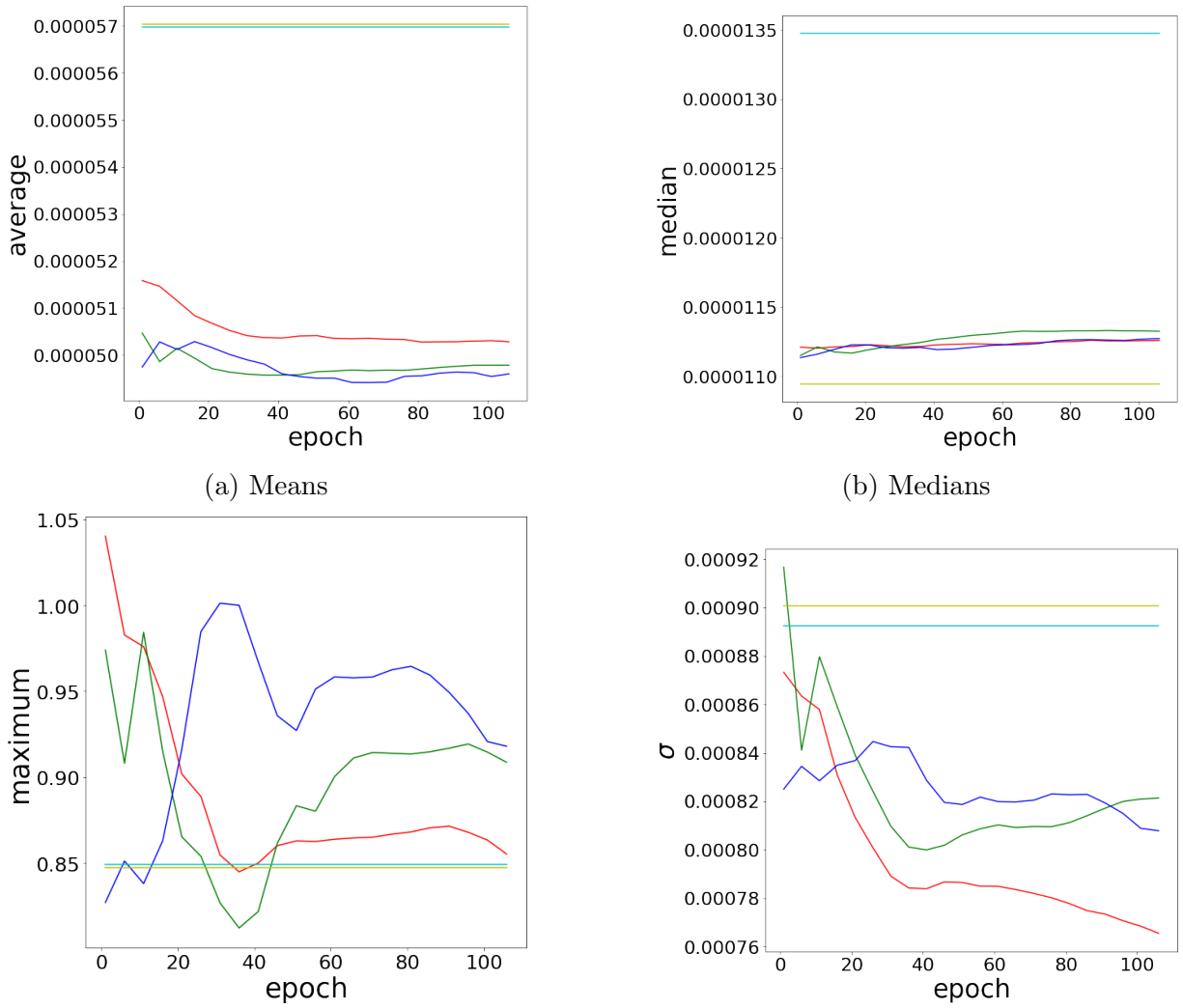

(a) Means

(b) Medians

(c) Maxima

(d) Standard deviations

Figure 6.7: Characteristic values of the super-resolved simulation boxes as functions of the training epoch. The red graph corresponds to the l_1 training, the green to the l_2 and the blue one the training process with all the loss functions. Additionally the corresponding value is plotted in cyan for the low-resolution simulation and in yellow for the high resolution simulation. In terms of these characteristic values the super-resolved simulation only outperforms the low resolution simulation in its median value as indicated by the proximity to the ground truth.

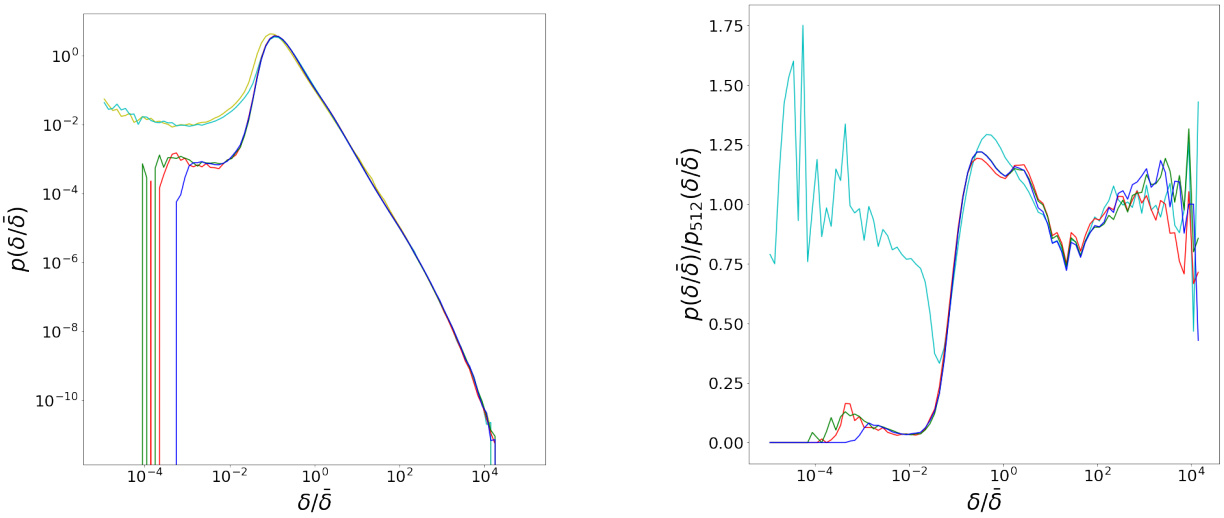

Figure 6.8: Distribution of the relative density (left) and the corresponding fluctuation relative to the true distribution (right). The red graph corresponds to the l_1 training, the green to the l_2, the blue one the training process with all the loss functions. The distribution for the high-resolution simulation is plotted in yellow and the one for the low resolution in cyan.

very small fraction of the actual voxels and only appears significant due to the logarithmic binning. Additionally, in these underdensities the ground truth itself is inaccurate as it contains numerical artifacts due to the low sampling of these areas by simulation particles. On scales that are of more interest the super-resolutions do not seem to perform strictly better nor strictly worse than the low resolution already did. It is also interesting to note that again there seems to be no significant difference in the performance of the different choices for the loss function.

To gain further insight into the statistical properties of our results we investigate the power spectra in figure 6.9. The power spectrum is plotted on the right and the corresponding relative deviation with respect to the ground truth on the left. We see that the power spectra of the super-resolutions all have a different form than both the input and the ground truth. The power spectra of the low and the high resolution simulations are identical at large scales while at small scales the low resolution simulation is slightly suppressed and shows more noise as one would expect for low-resolution simulations at small scales where the shot noise of the limited number of particles becomes significant. However, the low super-resolved simulations differ significantly from the other simulations at all scales, with the l_1-loss method being slightly closer to the correct values than the other two. All of the results from the super-resolution have a similar form, having too much structure on large scales and too little on small. The power spectra of the super-resolution have significantly less variation at small scales than the low-resolution simulation which shows that the generator networks are able to remove the features due to shot noise.

The different form of the power spectrum is mainly caused by a bad mapping of the

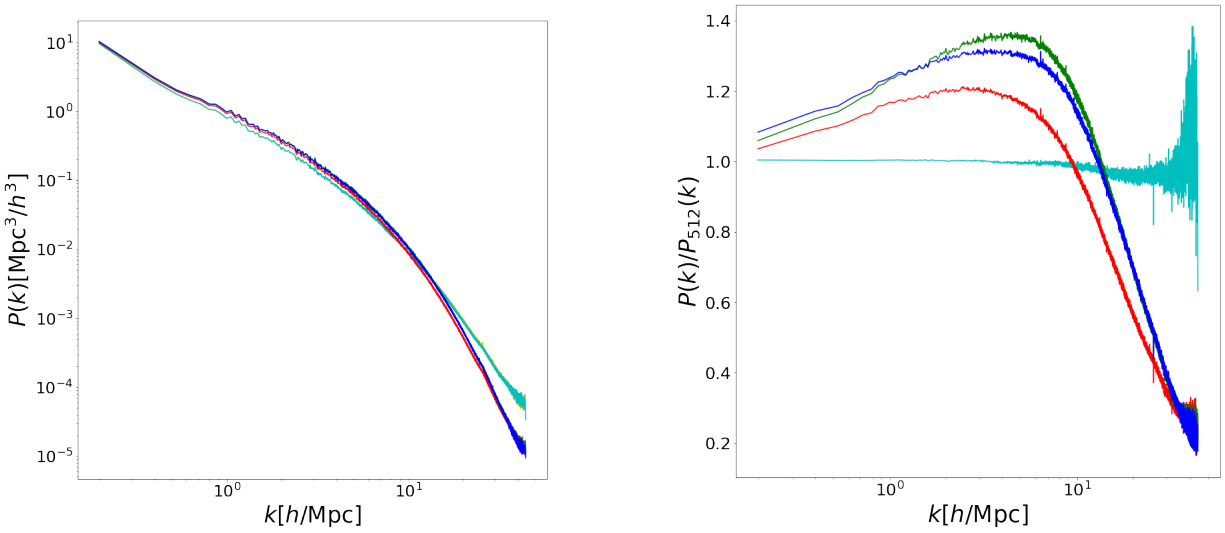

Figure 6.9: Power spectra of the simulation and its super-resolved versions (left) and the corresponding fluctuation relative to the power spectrum of the ground truth (right). The red graph corresponds to the l_1 training, the green to the l_2, the blue one to the training process with all the loss functions. The power spectrum for the high-resolution simulation is plotted in yellow and the one for the low resolution in cyan.

high overdensity voxels. This we tried to investigate in fig. 6.10. Therein we replaced the higher valued voxels of the super-resolution output with the values of the low resolution simulation. We chose different critical overdensity values as the boundary and investigated how it would affect the resulting power spectrum. We only used the results from the l_1-loss as there does not seem to be any qualitative difference between the results of the different method as we have seen in fig. 6.9. We see that the strong suppression of the power spectrum at small scales vanishes regardless of the choice of the critical overdensity. Even for a critical overdensity of 100 where we have replaced only 0.075% of all the voxels with the low-res input the strong suppression vanishes. However in all cases even for a critical overdensity of 1 where 10% of all voxels are replaced we still obtain a significant offset in the power spectrum which seems to be rather constant over all scales. This offset cannot be completely compensated by adjusting the average value to the be equal to the one of the input simulation. Furthermore as we increase the critical overdensity the super-resolved power spectrum ceases to have a constant shift relative to the ground truth but varies for different scales with a maximum at approximately $3h$/Mpc. We have not found so far an explanation for this behavior.

Finally we analyzed the void-size function (VSF) of the simulations. For that we used the Pylians3 library[3]. As the name implies the VSF is a function indicating the density of voids at a given radius R. We again present the absolute function as well as the relative deviations from the ground truth. Here it is again evident that our super-resolution results

[3]https://github.com/franciscovillaescusa/Pylians3

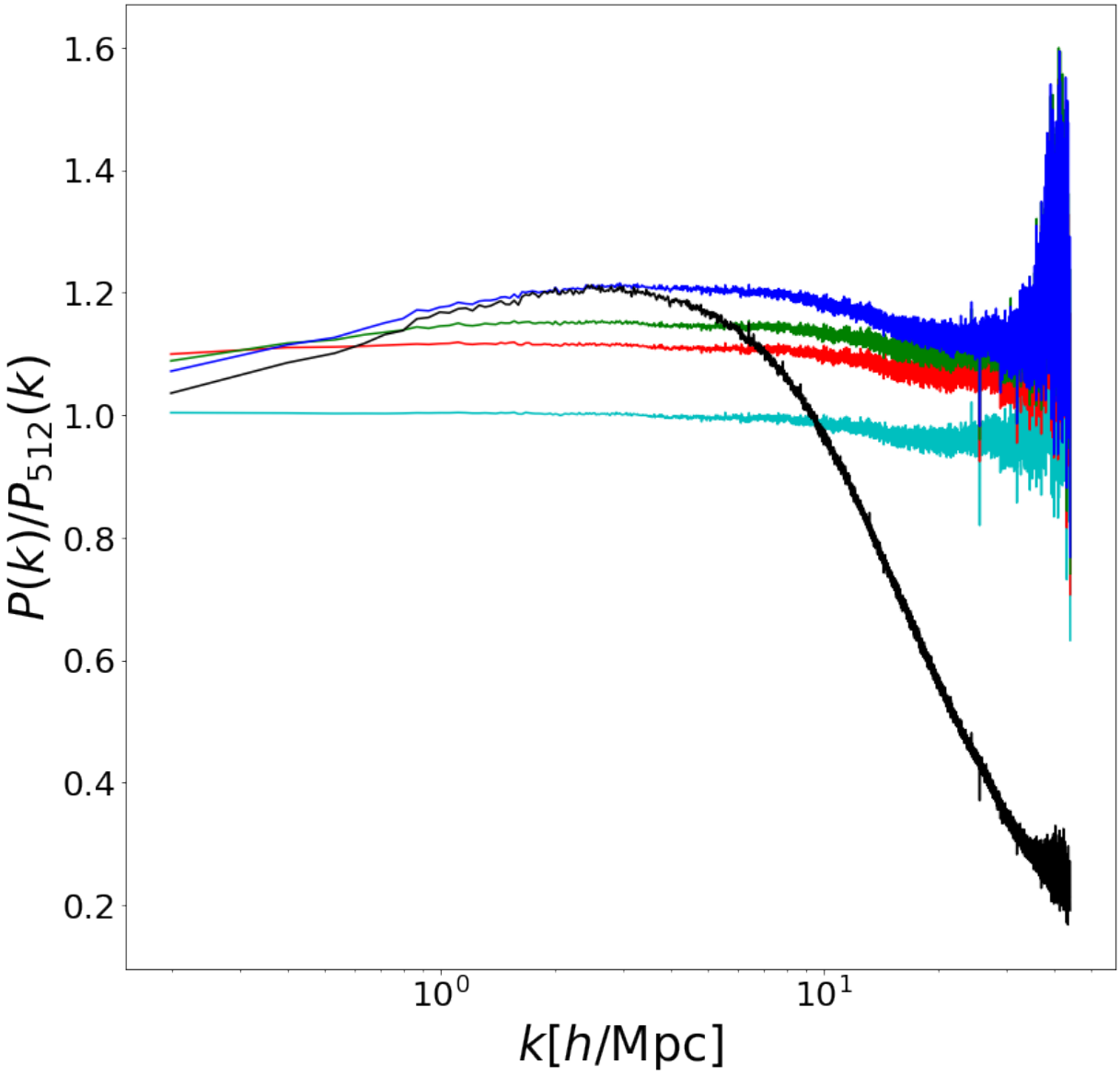

Figure 6.10: Relative power spectra obtained by replacing the highest value pixels with the corresponding low-resolution values. The red graph corresponds to all overdensities replaced, the green to overdensities of 10 times the average density and and blue to overdensities of 100 times the average density. Additionally the black curve represents the result with no replacements and the cyan curve represents the relative power spectrum of the low resolution simulation.

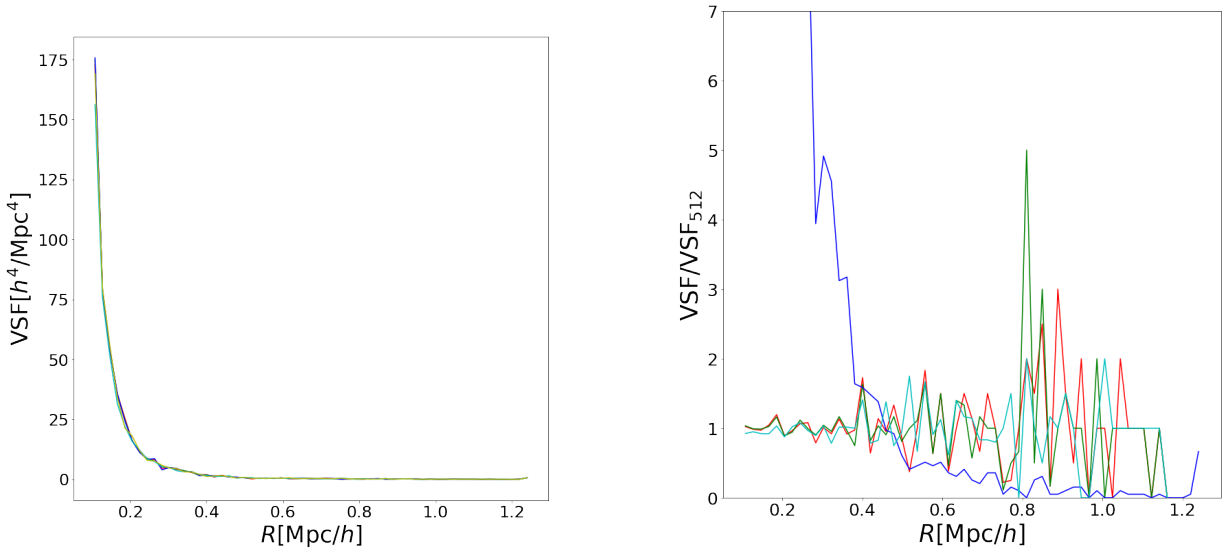

Figure 6.11: Void size functions (VSF) (left) and the corresponding fluctuation relative to the true distribution (right). The red graph corresponds to the l_1 training, the green to the l_2, the blue one to the training process with all the loss functions. The distribution for the high-resolution simulation is plotted in yellow and the one for the low resolution in cyan.

do not outperform the original input. This is surprising as the super-resolution should be particularly well suited for removing errors due to shot noise in the underdense regions of the low resolution simulation. The l_1 and l_2-loss methods perform about equally as well as the input but the method which also contains the l_∞ loss is very far off. It is difficult to give an explanation for this behavior yet, in particular when considering that visually this method does not result in a noticeably different output than the other two. One reason for such a high abundance of low radius voids might be that the l_∞-loss, which is only affected by one voxel of the output, results in features at very small scales of the order of a few voxels. This could explain the overabundance of voids at small radii but not their underabundance at larger ones.

6.4.2 GAN results

Next we investigate the results we have obtained using the GAN based approach. These are at this point far less successful than the simpler l-norm losses. If we only use the GAN loss from equation 6.17 we obtained inaccurate values for the high density voxels as the generator network tended to map them too much higher values than expected resulting in large errors due to the logarithmic scaling. For this reason we introduce an additional l_∞ norm to correct for these exceptional values such that the loss function for the generator becomes

$$\mathcal{L}_{\text{gen}} = -C(G(x)) + |\max(y_{\text{SR}}) - \max(y_{\text{r}})|. \tag{6.19}$$

This approach indeed helped eliminate the problem with divergent peaks.

In figure 6.12 we plot the loss functions for the generator and critic as a function of training epoch. To gain a better understanding of the contribution of the individual terms in these function we plot them as separate graphs. For the generator we see that the loss is mainly due to the GAN term with the l_∞ term being almost zero and not varying in any noticeable way as a function of epoch. The GAN contribution to the generator loss function as seen in eq. 6.19 is the negative of the critic term plotted in green on the right-hand side. For the critic we see that the gradient penalty is for the entire training process converged to zero ensuring that the 1-Lipschitz condition is fulfilled for the entire training process. The two other loss contribution evolve as mirror images of each other with the important difference of around 1.2 constant over all epochs after the first few which results in the red graph for the total loss. This expresses that the critic is on average capable to assign a batch from the super-resolution a lower value than one from the ground truth. This indicates that the critic functions correctly. The loss curve for the generator does not tell whether the generator works successfully or not which remains to be seen in the results.

The gradients of the loss contributions of the two networks are depicted in figure 6.13. For the generator we see two interesting features. First of all, although the loss contribution due to the l_∞-loss seems insignificant the gradient with respect to this loss is on the same order of magnitude as the one with respect to the GAN based loss. It is also interesting to notice that the gradient decreases by more than one order of magnitude which indicates that the network parameters are converging towards a small area in parameter space. For the critic we see that the gradients due to the individual losses are large but as fig. 6.13 shows they cancel each other to a very high precision which results in a total gradient 4 to 5 orders of magnitude smaller than its individual contributions. This means that the parameters of the critic network are almost entirely constant as a function of epoch. This result is rather puzzling as it indicates that although the generator parameters are improving, as the gradient with respect to them is significant, the generator is nevertheless not able to fool the critic even if the critic is not improving in response to the generator change.

In fig. 6.14 we see the same statistical measures we investigated for the other super-resolution algorithms now plotted for the GAN results. It is obvious that the GAN is performing poorly at this point for all the characteristic values. Additionally it does not improve with training epoch. An interesting feature to notice here is that for some epochs, in particular the earlier ones, the maximum and standard deviation of the super-resolved results remains at the same level as the input. A reason why these values are constant at first and then diverge rapidly remains to be found.

When looking at a slice of the super-resolved simulation in fig. 6.15 we see no significant differences between the input and the output simulation. The only improvement might be that some of the numerical artifacts in the low density regions are slightly less profound. In general we can see that we need significantly more improvements before the GAN network surpasses the l_p-norm approach at super-resolution.

Figure 6.16 shows the density distribution of the GAN results. We notice that the GAN

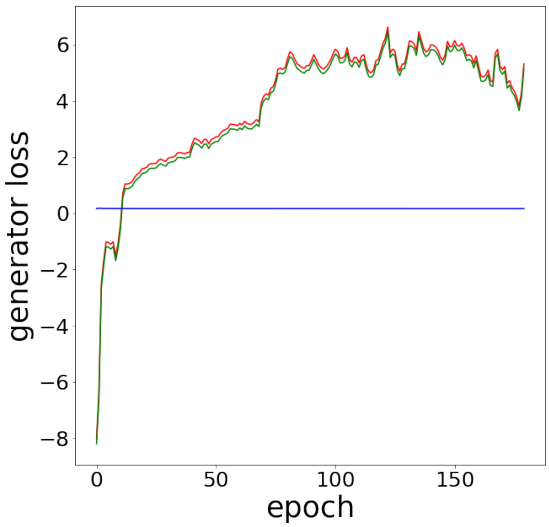

(a) Loss of the generator: the total loss corresponds to the red graph, the loss due to the GAN contribution is depicted in green and the loss due to the l_∞ contribution in blue.

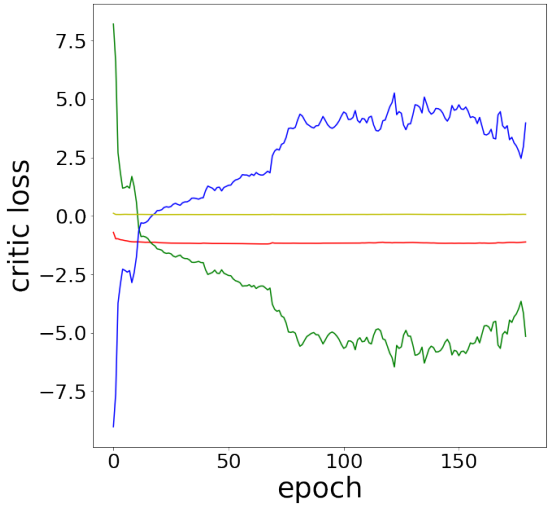

(b) Loss of the critic: the total loss corresponds to the red graph, the loss due to the output of the HR input is plotted in blue and the loss due to the SR input in green. Finally in yellow we see the loss due to the gradient penalty.

Figure 6.12: The average loss of the generators (left) and the critic (right) as a function of training epoch.

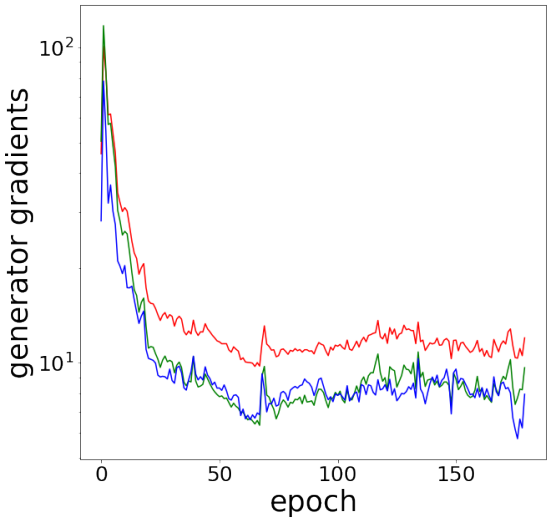

(a) Gradient of the generator: the total gradient corresponds to the red graph, the gradient due to the GAN contribution is depicted in green and the gradient due to the l_∞ contribution in blue.

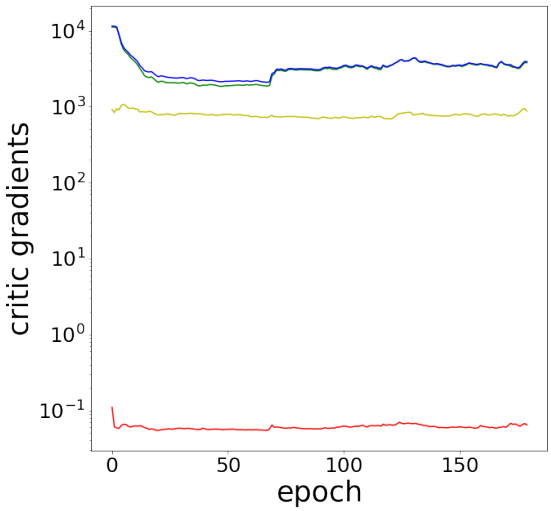

(b) Gradient of the critic: the total gradient corresponds to the red graph, the gradient due to the output of the HR input is plotted in blue and the gradient due to the SR input in green. Finally in yellow we see the gradient due to the gradient penalty.

Figure 6.13: The average total gradient of the generators as a function of training epoch for the generator (left) and the critic (right).

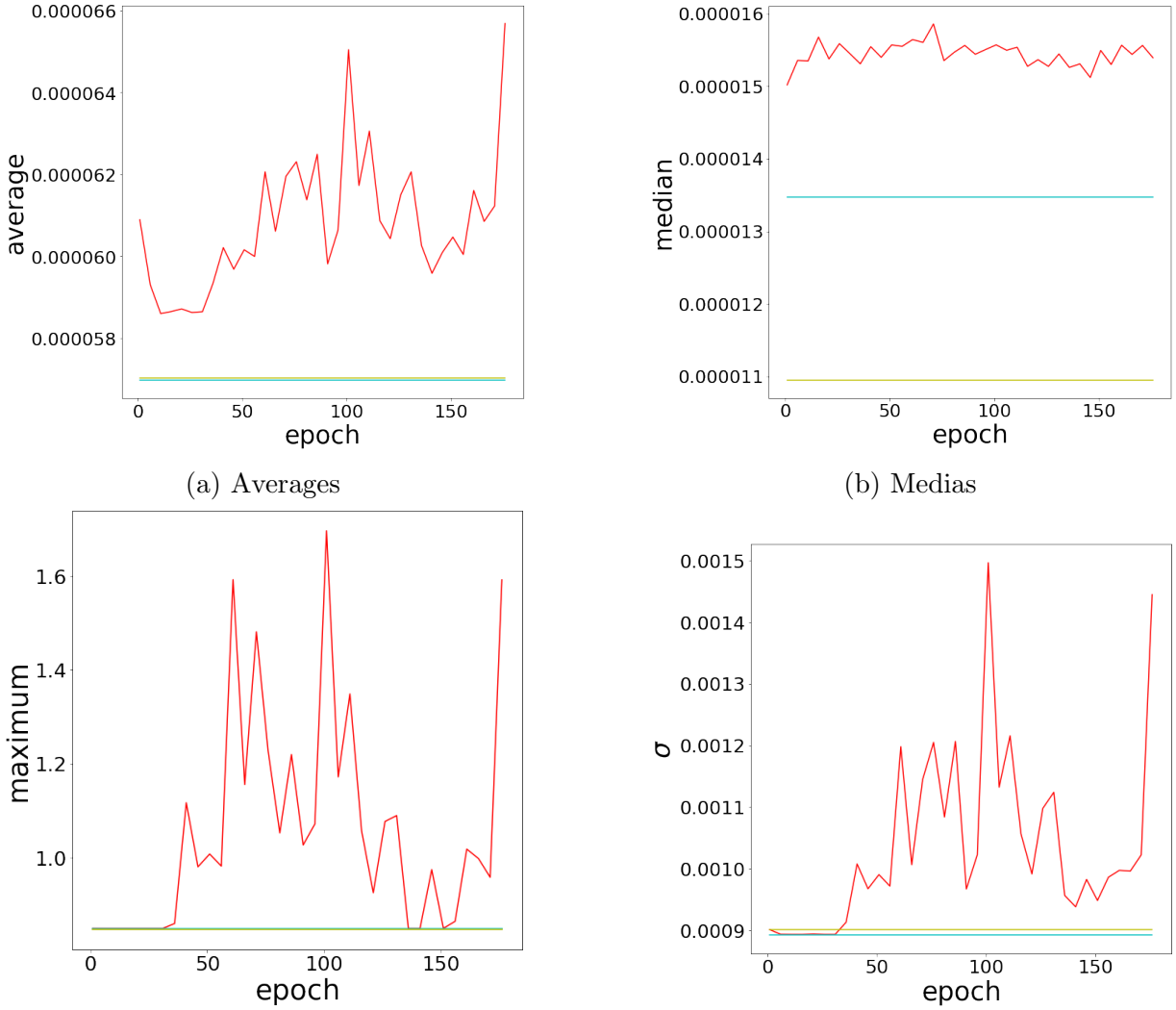

(a) Averages

(b) Medias

(c) Maxima

(d) Standard deviations

Figure 6.14: Statistical properties of the super-resolved simulation boxes as functions of the training epoch rescaled to the full dynamic range. The red graph corresponds to the GAN results. Additionally the corresponding value is plotted in cyan for the low-resolution simulation and in yellow for the high resolution simulation.

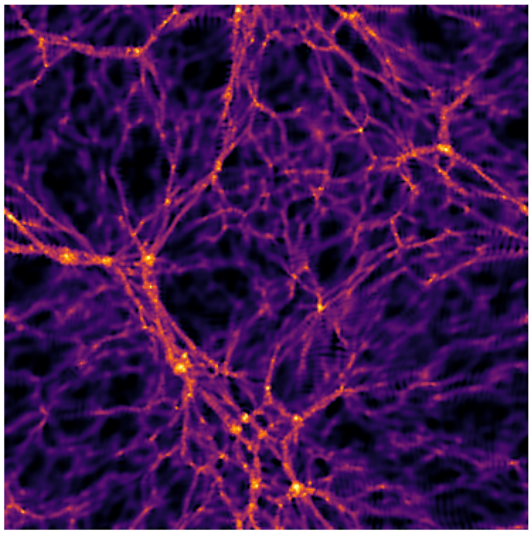

(a) Slice of the input simulation (256^3)

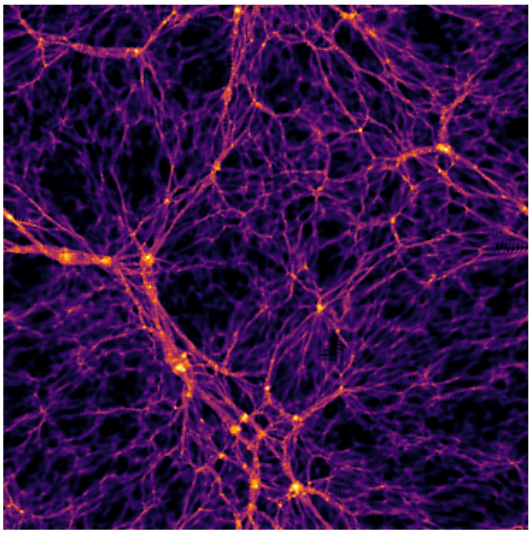

(b) Slice of the ground truth (512^3)

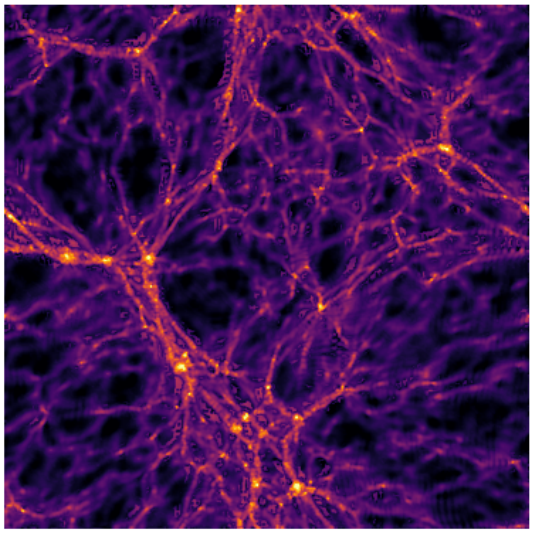

(c) Super-resolved using the gan-loss

Figure 6.15: Visualization of the super-resolved simulations together with the high resolution ground truth and the low resolution input simulation on a logarithmic color scale.

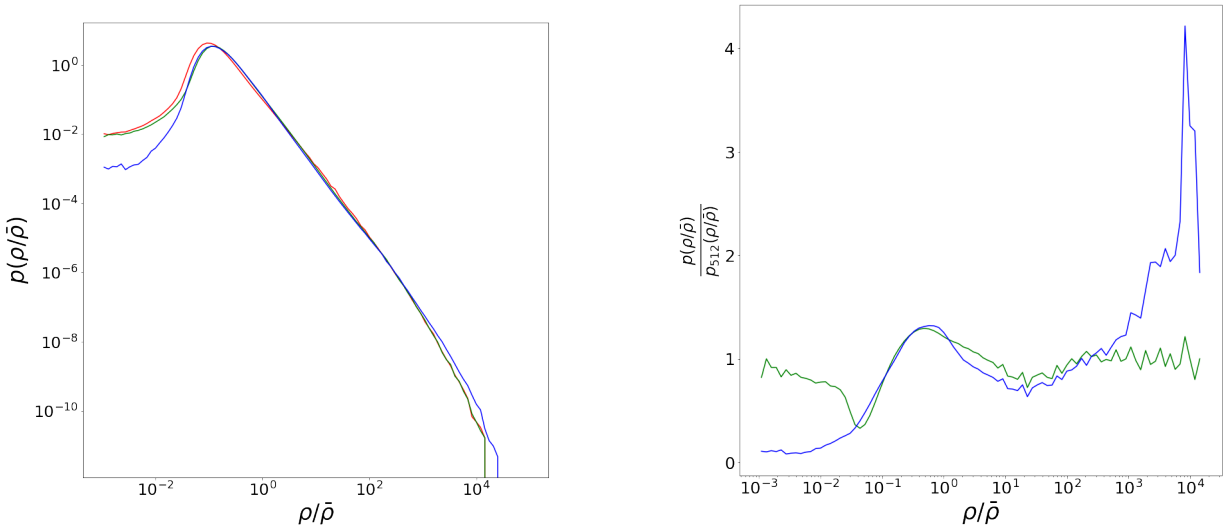

Figure 6.16: Distribution of the relative density (left) and the corresponding fluctuation relative to the true distribution (right). The blue graph corresponds to the super-resolution result, the distribution for the high-resolution simulation is plotted in red and the one for the low resolution in green.

is more successful than the other methods in conserving the highly underdense regions of the simulation. However, as we have mentioned before these are not of much significance. On the other hand there is a significantly too high abundance of high density peak as the relative plot on the right hand side shows.

Lastly in fig. 6.17 we plotted the power spectrum of the GAN super-resolution. Here we see, that the super-resolution has too much structure on all scales. In the relative plot we see that there is a relative maximum in the deviation at around $k = 0.9h/\text{Mpc}$. We do not see the suppression of amplitude at small scales which we saw in the previous methods. Instead we see that the power spectrum of the super-resolved result shows larger fluctuations on small scales than its input.

6.5 Conclusions and Outlook

The here presented results make it apparent that the methods of super-resolution we are currently using need significant improvements before they can be used to produce statistically reliable super-resolution results which can be utilized for further simulations and post processing. Using different l_p-norms we saw that the results look visually very promising but when examining their statistical properties, they are often further from the ground truth then their input. The GAN-approach on the other hand still fails to improve the input even visually.

The promising results produced by the method and the wide application of GAN for other super-resolution purposes as well as its recent development for cosmological applica-

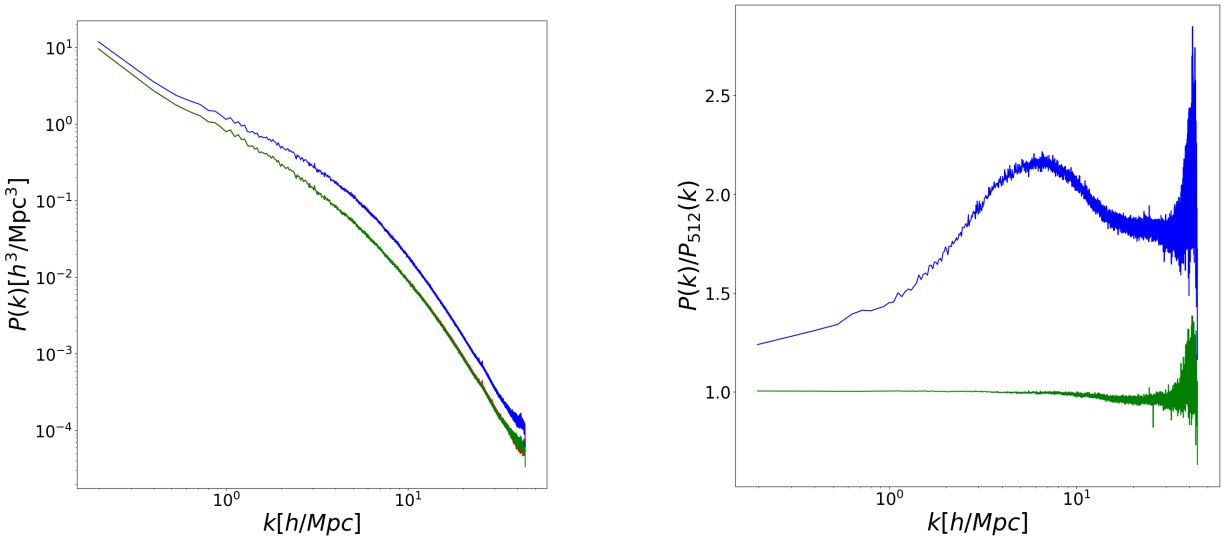

Figure 6.17: Power spectra of the simulation and its super-resolved version (left) and the corresponding fluctuation relative to the power spectrum of the ground truth (right). The blue graph corresponds to the super-resolution result. The power spectrum for the high-resolution simulation is plotted in orange and the one for the low resolution in green.

tions show that the approach works in principle. Therefore, it should be possible to obtain better results by further tuning the here presented method. In particular, through the explicit inclusion of relevant statistical properties into the loss function a higher accuracy with respect to these metrics can be achieved

An important factor is the scaling of the input. As the method with which the high dynamic range of the simulation is compressed into a small interval greatly affects how the loss functions affect different individual density scales. Therefore we will try out additional scaling functions as well as not scaling the input at all. Although the dynamic range of the simulation is high the fact that we use a residual architecture and the difference between the low and high resolution input is quite small it might still be a valid approach. Additionally, the logarithmic scaling can be introduced in the loss function instead of being used directly in the network.

Another experiment would be to build a 3D network without the need for a multi-pass approach. So far this was tried out for a GAN but did not work well, although this might have been because of problems in the code. The first step is to try to implement this approach with a simple l_p loss and once it is working move on to more complex GAN architectures.

Chapter 7

Discussion and Outlook

In this work, we presented three innovative projects, two of which explore the Lyman Continuum escape fraction in the high redshift Universe. The third one employs Artificial Neural Networks to super-resolve large-scale cosmological simulations. In the following chapter we summarize our main finding and present an outlook for the future developments of these projects.

7.1 Project 1: Lyman Continuum escape fractions of TNG50 halos with radiation transfer post-processing

Project summary

The first project presented in chapter 4 used post-processing of TNG50 galaxies [161, 145] together with the Monte Carlo radiation transfer code CRASH [32, 131, 74, 132] to determine LyC escape fractions. For the calculation of the ionizing emissivity of halos, stellar particles from the TNG simulation were retrieved and the spectral synthesis model BPASS [48] was used to model their ionizing spectra. Approximately, 10,000 halos have been post-processed with this method. These halos were sampled in the stellar mass range $M_\star = 10^6 - 10^9 M_\odot$ and in the three redshift bins $z = 6$, 8 and 10.

Main results

We have found that due to the discrete sampling of stellar populations, there is a large scatter in escape fractions for lower stellar mass halos $\lesssim 10^7 M_\odot$. For these halos the escape fraction is almost fully determined by whether it contains young and hence LyC photon producing stellar populations. This scatter decreases for higher stellar mass halos. There the escape fraction correlates more strongly with the spatial distribution of stellar populations. In particular, more diffuse halos have higher escape fractions.

We have further shown that the budget of ionizing radiation escaping into the IGM was driven by relatively small halos with stellar masses $\lesssim 10^{7.5} M_\odot$. The only exception being

halos at redshift 6 where this result could be numerically biased and more massive halos might contribute a significant amount of ionizing photons.

We have found a strong non-linear coupling between the unresolved local escape of ionizing photons and the global escape fraction of the halo. Therefore, it is likely that the quantitive trends in the escape fractions both in our work as well as in previous studies are not fully reliable. This is one of the reasons why we saw a large scatter over several orders of magnitude when comparing the average escape fraction obtained in different studies.

Outlook

Moving forward, it is necessary to improve the quantitative estimation of the escape fraction. For that purpose a more reliable sub-grid model needs to be developed. A possible approach would be to run several simulations over a large range of scales. Based on the results from these simulation, a hierarchical sub-grid model can be developed which allows to bridge the large range of scales which are relavant in galactic LyC escape.

Furthermore, it is of interest to study the correlation between features that are observable at higher redshifts and the LyC escape fraction. In particular, metal line emissions and ratios can be predicted which are described in chapter 3.5. This would allow for the verification of theoretical modelling with novel observations of the ALMA and JWST telescopes.

7.2 Project 2: Lyman Continuum escape fractions of TNG50 using physical modelling

Project summary

In this study, we used a physically motivated analytic model of the propagation of LyC photons through the galactic gas. In this model the escape fraction is evaluated based on the optical depth due to the gas and dust content below and above the galactic disc. Similarly to the previous project, we used TNG50 galaxies for our analysis. We processed all reasonably well resolved galaxies at redshifts $z = 20 - 5.2$, amounting to $\approx 500,000$ galaxies. The ionizing emissivity was obtained from the star formation rate using the model presented in [39]. In order to accurately resolve LyC producing regions and study the geometry of LyC escape, the escape fraction was evaluated for individual regions in the galaxies. This was achieved by resolving the galaxy on a grid and calculating the LyC escape for each individual grid cell.

Main results

Just as in the previous project, we have found that the bulk of LyC photons escape from lower mass galaxies with stellar masses $\lesssim 10^{7.5} M_{\odot}$.

Perhaps the most interesting result was the identification of two distinct modes of LyC escape. One mode is characterized by low gas column heights, high metallicity and low mass galaxies which have an extensive area of star formation. Here, LyC photons leak from the outer regions of the galaxy where the abundance of absorbing gas is relatively low. The other mode is characterized by high column heights, low metallicity with a wide range of galactic gas masses. LyC photons in this mode escape from small highly localized channels mostly located in the central regions of the galaxy where a large amount of star formation takes place.

Finally, based on our results we have developed a fitting model that determines the escape fraction of the galaxy based on its stellar and gas mass as well as its redshift. This model is suited for escape fraction prescriptions for galaxies in large scale studies.

Outlook

Given the relatively simple physical modelling, as well as the limited resolution of the TNG50 simulation, it is unlikely that the absolute values obtained for the escape fractions are reliable. Moving forward, we therefore plan to calibrate the model based on the LyC budget needed to successfully reionize the Universe by $z \approx 6$. With this calibration we plan to model the reionization history implied by our results.

7.3 Project 3: Super-resolving cosmological simulations

Project summary

In order to accurately capture cosmological structures over a wide range of scales, we worked on developing an artificial neural network for super-resolving small scale structures in large scale simulations. To generate these structures, we used convolutional neural networks together with a multipass approach [209], whereby structures are first super-resolved in two dimensions and subsequently turned by 90 degrees to optimize the super-resolution in the third dimension. We used Gadget 3 simulations [188] to generate the data used in the training process.

Two different approaches for the loss function of the network were tested. In the first approach we used a linear combination of p-norms evaluated on the difference between the super-resolved result and the corresponding ground-truth. In the other one we used a Wasserstein Generative Adversarial Network [9] where instead of a loss function an additional network is trained to measure the quality of the super-resolved data as compared to the ground truth.

Main results

We have found that using p-norm loss functions, we were able to generate visually promising results. However, a problem in the training process was the large dynamic range of densities in cosmological simulations. In order to decrease this range we applied a logarithmic scaling to the densities before training. However, once rescaled back to the full dynamic range the super-resolved data failed at matching the statistical properties of the ground-truth.

Outlook

Further development is needed to make the super-resolution approach viable for future studies. Namely, it is necessary to match the statistical properties of cosmological structures correctly with the super-resolution approach. One way to achieve this is through the explicit inclusion of the statistical metrics in the design of the loss function. Another approach is to use the full dynamic range of cosmological densities in the training process based on the fact that recent works (e.g.[108]) have shown that a WGAN can learn to super-resolve a large dynamic range correctly.

Bibliography

[1] *Wikimedia Commons: An example artificial neural network with a hidden layer*, 2006.

[2] *Wikimedia Commons: Wien's law of radiation*, 2006.

[3] *Wikimedia Commons: typical CNN architecture*, 2015.

[4] R.A. Alpher, H. Bethe und G. Gamow, *Physical Review* **73** (1948), 803.

[5] M.A. Alvarez, K. Finlator und M. Trenti, *The Astrophysical Journal Letters* **759** (2012), L38.

[6] J. Alves, T. Forveille, L. Pentericci und S. Shore, *Astronomy and Astrophysics* **641** (2020), 1.

[7] L. Anderson, F. Governato, M. Karcher, T. Quinn und J. Wadsley, *Monthly Notices of the Royal Astronomical Society* **468** (2017), 4077.

[8] M. Arjovsky und L. Bottou, *arXiv e-prints* (2017), arXiv:1701.04862.

[9] M. Arjovsky, S. Chintala und L. Bottou, *arXiv e-prints* (2017), arXiv:1701.07875.

[10] S. Baek, B. Semelin, P. Di Matteo, Y. Revaz und F. Combes, *Astronomy and Astrophysics* **523** (2010), A4.

[11] R. Barkana und A. Loeb, *The Astrophysical Journal* **10** (2000), 20.

[12] R. Barkana und A. Loeb, *Astrophysical Journal* **626** (2005), 1.

[13] K.S.S. Barrow, B.E. Robertson, R.S. Ellis, K. Nakajima, A. Saxena, D.P. Stark und M. Tang, *The Astrophysical Journal* **902** (2020), L39.

[14] F. Bian und X. Fan, *Monthly Notices of the Royal Astronomical Society: Letters* **493** (2020), L65.

[15] J.S. Bolton und M.G. Haehnelt, *Monthly Notices of the Royal Astronomical Society* **382** (2007), 325.

[16] R.J. Bouwens, G.D. Illingworth, P.A. Oesch, J. Caruana, B. Holwerda, R. Smit und S. Wilkins, *Astrophysical Journal* **811** (2015).

[17] R.J. Bouwens, G.D. Illingworth, P.A. Oesch, I. Labbé, M. Trenti, P. van Dokkum, M. Franx, M. Stiavelli, C.M. Carollo, D. Magee und V. Gonzalez, *Astrophysical Journal* **737** (2011), 90.

[18] R.J. Bouwens, G.D. Illingworth, R.I. Thompson und M. Franx, *The Astrophysical Journal* **624** (2005), L5.

[19] R.J. Bouwens, R. Smit, S. Schouws, M. Stefanon, R. Bowler, R. Endsley, V. Gonzalez, H. Inami, D. Stark, P. Oesch, J. Hodge, M. Aravena, E. da Cunha, P. Dayal, I. de Looze, A. Ferrara, Y. Fudamoto, L. Graziani, C. Li, T. Nanayakkara, A. Pallottini, R. Schneider, L. Sommovigo, M. Topping, P. van der Werf, H. Algera, L. Barrufet, A. Hygate, I. Labbé, D. Riechers und J. Witstok, *The Astrophysical Journal* **931** (2022), 160.

[20] T.M. Brown, J. Tumlinson, M. Geha, J.D. Simon, L.C. Vargas, D.A. VandenBerg, E.N. Kirby, J.S. Kalirai, R.J. Avila, M. Gennaro, H.C. Ferguson, R.R. Muñoz, P. Guhathakurta und A. Renzini, *The Astrophysical Journal* **796** (2014), 91.

[21] P. Busch, M.B. Eide, B. Ciardi und K. Kakiichi, *Monthly Notices of the Royal Astronomical Society* **498** (2020), 4533.

[22] C. Byrohl und D. Nelson, *arXiv e-prints* (2022), arXiv:2212.08666.

[23] D. Calzetti, *Astronomical Journal* **113** (1997), 162.

[24] R. Cen und J. Ostriker, *Astrophysical Journal* **393** (1992), 22.

[25] G. Chabrier, *Publications of the Astronomical Society of the Pacific* **115** (2003), 763.

[26] J. Chisholm, S. Gazagnes, D. Schaerer, A. Verhamme, J.R. Rigby, M. Bayliss, K. Sharon, M. Gladders und H. Dahle, *Astronomy and Astrophysics* **616** (2018).

[27] J. Chisholm, J.X. Prochaska, D. Schaerer, S. Gazagnes und A. Henry, *Monthly Notices of the Royal Astronomical Society* **498** (2020), 2554.

[28] Y. Choi, J.J. Dalcanton, B.F. Williams, E.D. Skillman, M. Fouesneau, K.D. Gordon, K.M. Sandstrom, D.R. Weisz und K.M. Gilbert, *The Astrophysical Journal* **902** (2020), 54.

[29] T.R. Choudhury und A. Ferrara, *Monthly Notices of the Royal Astronomical Society: Letters* **380** (2007), 6.

[30] B. Ciardi, J.S. Bolton, A. Maselli und L. Graziani, *Monthly Notices of the Royal Astronomical Society* **423** (2012), 558.

[31] B. Ciardi und A. Ferrara, *Space Science Reviews* **116** (2005), 625.

[32] B. Ciardi, A. Ferrara, S. Marri und G. Raimondo, *Monthly Notices of the Royal Astronomical Society* **324** (2001), 381.

[33] B. Ciardi, A. Ferrara und S.D.M. White, *Monthly Notices of the Royal Astronomical Society* **344** (2003), L7.

[34] C. Conroy und K.M. Kratter, *Astrophysical Journal* **755** (2012).

[35] J.E. Dale, B. Ercolano und I.A. Bonnell, *Monthly Notices of the Royal Astronomical Society* **430** (2013), 234.

[36] A. D'Aloisio, P.R. Sanderbeck, M. McQuinn, H. Trac und P.R. Shapiro, *Monthly Notices of the Royal Astronomical Society* **468** (2017), 4691.

[37] M. Davis, G. Efstathiou, C.S. Frenk und S.D. White, *The Astrophysical Journal* **292** (1985), 371.

[38] P. Dayal und A. Ferrara, *Physics Reports* **780** (2018), 1.

[39] P. Dayal, A. Ferrara, L. Sommovigo, R. Bouwens, P.A. Oesch, R. Smit, V. Gonzalez, S. Schouws, M. Stefanon, C. Kobayashi, J. Bremer, H.S.B. Algera, M. Aravena, R.A.A. Bowler, E. da Cunha, Y. Fudamoto, L. Graziani, J. Hodge, H. Inami, I. De Looze, A. Pallottini, D. Riechers, R. Schneider, D. Stark und R. Endsley, *Monthly Notices of the Royal Astronomical Society* **512** (2022), 989.

[40] M. Dijkstra, M. Gronke und A. Venkatesan, *Astrophysical Journal* **828** (2016), 71.

[41] M. Dijkstra, S. Wyithe, Z. Haiman, A. Mesinger und L. Pentericci, *Monthly Notices of the Royal Astronomical Society* **440** (2014), 3309.

[42] J.B. Dove, J.M. Shull und A. Ferrara, *Astrophysical Journal* **531** (2000), 846.

[43] B.T. Draine und A. Li, *The Astrophysical Journal* **657** (2007), 810.

[44] M.B. Eide, B. Ciardi, L. Graziani, P. Busch, Y. Feng und T. Di Matteo, *Monthly Notices of the Royal Astronomical Society* **498** (2020), 6083.

[45] M.B. Eide, B. Ciardi, L. Graziani, P. Busch, Y. Feng und T. Di Matteo, *Monthly Notices of the Royal Astronomical Society* **498** (2020), 6083.

[46] A. Einstein, *Annalen der Physik* **354** (1916), 769.

[47] D.J. Eisenstein und W. Hu, *Astrophysical Journal* **496** (1998), 605.

[48] J. Eldridge, E. Stanway, L. Xiao, L. McClelland, G. Taylor, M. Ng, S. Greis und J. Bray, *Publications of the Astronomical Society of Australia* **34** (2017).

[49] J.J. Eldridge, R.G. Izzard und C.A. Tout, *Monthly Notices of the Royal Astronomical Society* **384** (2008), 1109.

[50] B.G. Elmegreen, *The Astrophysical Journal* **530** (2000), 277.

[51] A.L. Faisst, *The Astrophysical Journal* **829** (2016), 99.

[52] C.A. Faucher-Giguère, *Monthly Notices of the Royal Astronomical Society* **493** (2020), 1614.

[53] C.A. Faucher-Giguère, A. Lidz, M. Zaldarriaga und L. Hernquist, *Astrophysical Journal* **703** (2009), 1416.

[54] A. Ferrara und A. Loeb, *Monthly Notices of the Royal Astronomical Society* **431** (2013), 2826.

[55] A. Ferrara, L. Vallini, A. Pallottini, S. Gallerani, S. Carniani, M. Kohandel, D. Decataldo und C. Behrens, *Monthly Notices of the Royal Astronomical Society* **489** (2019), 1.

[56] K.M. Ferrière, *Reviews of Modern Physics* **73** (2001), 1031.

[57] K. Finlator, L. Keating, B.D. Oppenheimer, R. Davé und E. Zackrisson, *Monthly Notices of the Royal Astronomical Society* **480** (2018), 2628.

[58] A. Friedmann, *Zeitschrift fur Physik* **10** (1922), 377.

[59] C.S. Froning und J.C. Green, *Astrophysics and Space Science* **320** (2009), 181.

[60] A. Fujita, C.L. Martin, M.M. Mac Low und T. Abel, *Astrophysical Journal* **599** (2003), 50.

[61] S.R. Furlanetto und S.P. Oh, *Monthly Notices of the Royal Astronomical Society* **457** (2016), 1813.

[62] S.R. Furlanetto, M. Zaldarriaga und L. Hernquist, *The Astrophysical Journal* **613** (2004), 1.

[63] E. Garaldi, R. Kannan, A. Smith, V. Springel, R. Pakmor, M. Vogelsberger und L. Hernquist, *Monthly Notices of the Royal Astronomical Society* **512** (2022), 4909.

[64] M. Gaspari, F. Brighenti, A. D'Ercole und C. Melioli, *Monthly Notices of the Royal Astronomical Society* **415** (2011), 1549.

[65] R. Ghara, T.R. Choudhury und K.K. Datta, *Monthly Notices of the Royal Astronomical Society* **447** (2015), 1806.

[66] M. Glatzle, B. Ciardi und L. Graziani, *Monthly Notices of the Royal Astronomical Society* **482** (2019), 321.

[67] M. Glatzle, L. Graziani und B. Ciardi, *Monthly Notices of the Royal Astronomical Society* **510** (2022), 1068.

[68] N.Y. Gnedin, *Astrophysical Journall* **535** (2000), L75.

[69] N.Y. Gnedin und A.A. Kaurov, *Astrophysical Journal* **793** (2014).

[70] I. Goodfellow, Y. Bengio und A. Courville: *Deep Learning*. MIT Press, 2016. `http://www.deeplearningbook.org`.

[71] I.J. Goodfellow, J. Pouget-Abadie, M. Mirza, B. Xu, D. Warde-Farley, S. Ozair, A. Courville und Y. Bengio, *arXiv e-prints* (2014), arXiv:1406.2661.

[72] Y. Götberg, S.E. De Mink, M. McQuinn, E. Zapartas, J.H. Groh und C. Norman, *Astronomy and Astrophysics* **634** (2020).

[73] L. Graziani, B. Ciardi und M. Glatzle, *Monthly Notices of the Royal Astronomical Society* **479** (2018), 4320.

[74] L. Graziani, A. Maselli und B. Ciardi, *Monthly Notices of the Royal Astronomical Society* **431** (2013), 722.

[75] L. Guaita, L. Pentericci, A. Grazian, E. Vanzella, M. Nonino, M. Giavalisco, G. Zamorani, A. Bongiorno, P. Cassata, M. Castellano, B. Garilli, E. Gawiser, V. Le Brun, O. Le Fèvre, B.C. Lemaux, D. Maccagni, E. Merlin, P. Santini, L.A. Tasca, R. Thomas, E. Zucca, S. De Barros, N.P. Hathi, R. Amorin, S. Bardelli und A. Fontana, *Astronomy and Astrophysics* **587** (2016), 1.

[76] I. Gulrajani, F. Ahmed, M. Arjovsky, V. Dumoulin und A. Courville, *arXiv e-prints* (2017), arXiv:1704.00028.

[77] J.E. Gunn und I. Gott, J. Richard, *Astrophysical Journal* **176** (1972), 1.

[78] A.H. Guth, *Physical Review D* **23** (1981), 347.

[79] F. Haardt und P. Madau, *The Astrophysical Journal* **746** (2012), 125.

[80] O. Hahn und T. Abel, *Monthly Notices of the Royal Astronomical Society* **415** (2011), 2101.

[81] S. Hassan, R. Davé, S. Mitra, K. Finlator, B. Ciardi und M.G. Santos, *Monthly Notices of the Royal Astronomical Society* **473** (2018), 227.

[82] M.W. Hattab, R.S. De Souza, B. Ciardi, J.P. Paardekooper, S. Khochfar und C.D. Vecchia, *Monthly Notices of the Royal Astronomical Society* **483** (2019), 3307.

[83] C.C. He, M. Ricotti und S. Geen, *Monthly Notices of the Royal Astronomical Society* **492** (2020), 4858.

[84] K. He, X. Zhang, S. Ren und J. Sun, *arXiv e-prints* (2016), arXiv:1603.05027.

[85] T.M. Heckman, S. Borthakur, R. Overzier, G. Kauffmann, A. Basu-Zych, C. Leitherer, K. Sembach, D.C. Martin, R.M. Rich, D. Schiminovich und M. Seibert, *The Astrophysical Journal* **730** (2011), 5.

[86] T.M. Heckman, K.R. Sembach, G.R. Meurer, C. Leitherer, D. Calzetti und C.L. Martin, *Astrophysical Journal* **558** (2001), 56.

[87] A. Henry, D.A. Berg, C. Scarlata, A. Verhamme und D. Erb, *The Astrophysical Journal* **855** (2018), 96.

[88] P.F. Hopkins, D. Kereš, J. Oñorbe, C.A. Faucher-Giguère, E. Quataert, N. Murray und J.S. Bullock, *Monthly Notices of the Royal Astronomical Society* **445** (2014), 581.

[89] P.F. Hopkins, A. Wetzel, D. Kereš, C.A. Faucher-Giguère, E. Quataert, M. Boylan-Kolchin, N. Murray, C.C. Hayward, S. Garrison-Kimmel, C. Hummels, R. Feldmann, P. Torrey, X. Ma, D. Anglés-Alcázar, K.Y. Su, M. Orr, D. Schmitz, I. Escala, R. Sanderson, M.Y. Grudić, Z. Hafen, J.H. Kim, A. Fitts, J.S. Bullock, C. Wheeler, T.K. Chan, O.D. Elbert und D. Narayanan, *Monthly Notices of the Royal Astronomical Society* **480** (2018), 800.

[90] C.S. Howard, R.E. Pudritz, W.E. Harris und R.S. Klessen, *Monthly Notices of the Royal Astronomical Society* **475** (2018), 3121.

[91] E. Hubble, *Proceedings of the National Academy of Science* **15** (1929), 168.

[92] A. Hutter, P. Dayal, G. Yepes, S. Gottlöber, L. Legrand und G. Ucci, *Monthly Notices of the Royal Astronomical Society* **503** (2021), 3698.

[93] I.T. Iliev, G. Mellema, K. Ahn, P.R. Shapiro, Y. Mao und U.L. Pen, *Monthly Notices of the Royal Astronomical Society* **439** (2014), 725.

[94] I.T. Iliev, G. Mellema, P.R. Shapiro und U.L. Pen, *Monthly Notices of the Royal Astronomical Society* **376** (2007), 534.

[95] A.K. Inoue, I. Iwata und J.M. Deharveng, *Monthly Notices of the Royal Astronomical Society: Letters* **371** (2006), L1.

[96] A.K. Inoue, I. Iwata, J.M. Deharveng, V. Buat und D. Burgarella, *Astronomy and Astrophysics* **435** (2005), 471.

[97] J. Japelj, E. Vanzella, F. Fontanot, S. Cristiani, G.B. Caminha, P. Tozzi, I. Balestra, P. Rosati und M. Meneghetti, *Monthly Notices of the Royal Astronomical Society* **468** (2017), 389.

[98] J.H. Jeans, *Philosophical Transactions of the Royal Society of London Series A* **199** (1902), 1.

[99] L. Jiang, Y. Ning, X. Fan, L.C. Ho, B. Luo, F. Wang, J. Wu, X.B. Wu, J. Yang und Z.Y. Zheng, *Nature Astronomy* **6** (2022), 850.

[100] R. Kannan, E. Garaldi, A. Smith, R. Pakmor, V. Springel, M. Vogelsberger und L. Hernquist, *Monthly Notices of the Royal Astronomical Society* **511** (2022), 4005.

[101] R. Kannan, M. Vogelsberger, F. Marinacci, R. McKinnon, R. Pakmor und V. Springel, *Monthly Notices of the Royal Astronomical Society* **485** (2019), 117.

[102] H. Katz, D. Crossed D Signurovčíková, T. Kimm, J. Rosdahl, J. Blaizot, M.G. Haehnelt, J. Devriendt, A. Slyz, R. Ellis und N. Laporte, *Monthly Notices of the Royal Astronomical Society* **498** (2020), 164.

[103] H. Katz, T. Garel, J. Rosdahl, V. Mauerhofer, T. Kimm, J. Blaizot, L. Michel-Dansac, J. Devriendt, A. Slyz und M. Haehnelt. *MgII in the JWST Era: a Probe of Lyman Continuum Escape?*, 2022.

[104] J.G. Kim, W.T. Kim und E.C. Ostriker, *The Astrophysical Journal* **883** (2019), 102.

[105] T. Kimm, J. Blaizot, T. Garel, L. Michel-Dansac, H. Katz, J. Rosdahl, A. Verhamme und M. Haehnelt, *Monthly Notices of the Royal Astronomical Society* **486** (2019), 2215.

[106] T. Kimm und R. Cen, *Astrophysical Journal* **788** (2014).

[107] T. Kitayama, N. Yoshida, H. Susa und M. Umemura, *Astrophysical Journal* **613** (2004), 631.

[108] D. Kodi Ramanah, T. Charnock, F. Villaescusa-Navarro und B.D. Wandelt, *Monthly Notices of the Royal Astronomical Society* **495** (2020), 4227.

[109] E. Komatsu, K.M. Smith, J. Dunkley, C.L. Bennett, B. Gold, G. Hinshaw, N. Jarosik, D. Larson, M.R. Nolta, L. Page, D.N. Spergel, M. Halpern, R.S. Hill, A. Kogut, M. Limon, S.S. Meyer, N. Odegard, G.S. Tucker, J.L. Weiland, E. Wollack und E.L. Wright, *Astrophysical Journal, Supplement* **192** (2011), 18.

[110] I. Kostyuk, D. Nelson, B. Ciardi, M. Glatzle und A. Pillepich, *Monthly Notices of the Royal Astronomical Society* **521** (2023), 3077.

[111] P. Kroupa, *Science* **295** (2002), 82.

[112] M. Kuhlen und C.A. Faucher-Giguère, *Monthly Notices of the Royal Astronomical Society* **423** (2012), 862.

[113] Y. LeCun, B. Boser, J.S. Denker, D. Henderson, R.E. Howard, W. Hubbard und L.D. Jackel, *Neural computation* **1** (1989), 541.

[114] G. Ledrew, *Journal of the RAS of Canada* **95** (2001), 32.

[115] R. Leike und T. Enßlin, *Entropy* **19** (2017), 402.

[116] E. Leitet, N. Bergvall, N. Piskunov und B.G. Andersson, *Astronomy and Astrophysics* **532** (2011), A107.

[117] C.D. Levermore, *Journal of Quantitiative Spectroscopy and Radiative Transfer* **31** (1984), 149.

[118] J.S. Lewis, P. Ocvirk, D. Aubert, J.G. Sorce, P.R. Shapiro, N. Deparis, T. Dawoodbhoy, R. Teyssier, G. Yepes, S. Gottlöber, K. Ahn, I.T. Iliev und J. Chardin, *Monthly Notices of the Royal Astronomical Society* **496** (2020), 4342.

[119] J.S.W. Lewis, P. Ocvirk, Y. Dubois, D. Aubert, J. Chardin, N. Gillet und É. Thélie, *arXiv e-prints* (2022), arXiv:2204.03949.

[120] Y. Li, Y. Ni, R.A.C. Croft, T. Di Matteo, S. Bird und Y. Feng, *Proceedings of the National Academy of Science* **118** (2021), e2022038118.

[121] A. Loeb und R. Barkana, *Annual Review of Astronomy and Astrophysics* **39** (2001), 19.

[122] D. Lynden-Bell, *Monthly Notices of the Royal Astronomical Society* **136** (1967), 101.

[123] Q.B. Ma, S. Fiaschi, B. Ciardi, P. Busch und M.B. Eide, *Monthly Notices of the Royal Astronomical Society* **513** (2022), 1513.

[124] X. Ma, P.F. Hopkins, D. Kasen, E. Quataert, C.A. Faucher-Giguère, D. Kereš, N. Murray und A. Strom, *Monthly Notices of the Royal Astronomical Society* **459** (2016), 3614.

[125] X. Ma, E. Quataert, A. Wetzel, P.F. Hopkins, C.A. Faucher-Giguère und D. Kereš, *Monthly Notices of the Royal Astronomical Society* **498** (2020), 2001.

[126] P. Madau und T. Fragos, *Astrophysical Journal* **840** (2017), 39.

[127] P. Madau und F. Haardt, *Astrophysical Journal Letters* **813** (2015), L8.

[128] P. Madau, F. Haardt und M.J. Rees, *Astrophysical Journal* **514** (1999), 648.

[129] F. Marinacci, M. Vogelsberger, R. Pakmor, P. Torrey, V. Springel, L. Hernquist, D. Nelson, R. Weinberger, A. Pillepich, J. Naiman und S. Genel, *Monthly Notices of the Royal Astronomical Society* **480** (2018), 5113.

[130] S. Mascia, L. Pentericci, A. Calabro', T. Treu, P. Santini, L. Yang, L. Napolitano, G. Roberts-Borsani, P. Bergamini, C. Grillo, P. Rosati, B. Vulcani, M. Castellano, K. Boyett, A. Fontana, K. Glazebrook, A. Henry, C. Mason, E. Merlin, T. Morishita, T. Nanayakkara, D. Paris, N. Roy, H. Williams, X. Wang, G. Brammer, M. Bradac, W. Chen, P.L. Kelly, A.M. Koekemoer, M. Trenti und R.A. Windhorst, *arXiv e-prints* (2023), arXiv:2301.02816.

[131] A. Maselli, B. Ciardi und A. Kanekar, *Monthly Notices of the Royal Astronomical Society* **393** (2009), 171.

[132] A. Maselli, A. Ferrara und B. Ciardi, *Monthly Notices of the Royal Astronomical Society* **345** (2003), 379.

[133] C.A. Mason, R.P. Naidu, S. Tacchella und J. Leja, *Monthly Notices of the Royal Astronomical Society* **489** (2019), 2669.

[134] J. Matthee, D. Sobral, P. Best, A.A. Khostovan, I. Oteo, R. Bouwens und H. Röttgering, *Monthly Notices of the Royal Astronomical Society* **465** (2017), 3637.

[135] A. Meiksin und P. Madau, *Astrophysical Journal* **412** (1993), 34.

[136] A. Mesinger, S. Furlanetto und R. Cen, *Monthly Notices of the Royal Astronomical Society* **411** (2011), 955.

[137] U. Meštrić, E.V. Ryan-Weber, J. Cooke, R. Bassett, L.J. Prichard und M. Rafelski, *Monthly Notices of the Royal Astronomical Society* **508** (2021), 4443.

[138] T. Mitchell, (1997).

[139] H.W. Moos, W.C. Cash, L.L. Cowie, A.F. Davidsen, A.K. Dupree, P.D. Feldman, S.D. Friedman, J.C. Green, R.F. Green, C. Gry, J.B. Hutchings, E.B. Jenkins, J.L. Linsky, R.F. Malina, A.G. Michalitsianos, B.D. Savage, J.M. Shull, O.H.W. Siegmund, T.P. Snow, G. Sonneborn, A. Vidal-Madjar, A.J. Willis, B.E. Woodgate, D.G. York, T.B. Ake, B.G. Andersson, J.P. Andrews, R.H. Barkhouser, L. Bianchi, W.P. Blair, K.R. Brownsberger, A.N. Cha, P. Chayer, S.J. Conard, A.W. Fullerton, G.A. Gaines, R. Grange, M.A. Gummin, G. Hebrard, G.A. Kriss, J.W. Kruk, D. Mark, D.K. McCarthy, C.L. Morbey, R. Murowinski, E.M. Murphy, W.R. Oegerle, R.G. Ohl, C. Oliveira, S.N. Osterman, D.J. Sahnow, M. Saisse, K.R. Sembach, H.A. Weaver, B.Y. Welsh, E. Wilkinson und W. Zheng, *Astrophysical Journal, Letters* **538** (2000), L1.

[140] R.P. Naidu, J. Matthee, P.A. Oesch, C. Conroy, D. Sobral, G. Pezzulli, M. Hayes, D. Erb, R. Amorín, M. Gronke, D. Schaerer, S. Tacchella, J. Kerutt, A. Paulino-Afonso, J. Calhau, M. Llerena und H. Röttgering. *The Synchrony of Production & Escape: Half the Bright Lyα Emitters at $z \approx 2$ have Lyman Continuum Escape Fractions* $\approx 50\%$ (2021).

[141] R.P. Naidu, S. Tacchella, C.A. Mason, S. Bose, P.A. Oesch und C. Conroy, *Astrophysical Journal* **892** (2020), 109.

[142] J.P. Naiman, A. Pillepich, V. Springel, E. Ramirez-Ruiz, P. Torrey, M. Vogelsberger, R. Pakmor, D. Nelson, F. Marinacci, L. Hernquist, R. Weinberger und S. Genel, *Monthly Notices of the Royal Astronomical Society* **477** (2018), 1206.

[143] K. Nakajima, R.S. Ellis, B.E. Robertson, M. Tang und D.P. Stark, *The Astrophysical Journal* **889** (2020), 161.

[144] K. Nakajima und M. Ouchi, *Monthly Notices of the Royal Astronomical Society* **442** (2014), 900.

[145] D. Nelson, A. Pillepich, V. Springel, R. Weinberger, L. Hernquist, R. Pakmor, S. Genel, P. Torrey, M. Vogelsberger, G. Kauffmann, F. Marinacci und J. Naiman, *Monthly Notices of the Royal Astronomical Society* **475** (2018), 624.

[146] D. Nelson, V. Springel, A. Pillepich, V. Rodriguez-Gomez, P. Torrey, S. Genel, M. Vogelsberger, R. Pakmor, F. Marinacci, R. Weinberger, L. Kelley, M. Lovell, B. Diemer und L. Hernquist, *Computational Astrophysics and Cosmology* **6** (2019), 2.

[147] D. Nelson, M. Vogelsberger, S. Genel, D. Sijacki, D. Kereš, V. Springel und L. Hernquist, *Monthly Notices of the Royal Astronomical Society* **429** (2013), 3353.

[148] Y. Ni, Y. Li, P. Lachance, R.A.C. Croft, T. Di Matteo, S. Bird und Y. Feng, *Monthly Notices of the Royal Astronomical Society* **507** (2021), 1021.

[149] P. Ocvirk, D. Aubert, J.G. Sorce, P.R. Shapiro, N. Deparis, T. Dawoodbhoy, J. Lewis, R. Teyssier, G. Yepes, S. Gottlöber, K. Ahn, I.T. Iliev und Y. Hoffman, *Monthly Notices of the Royal Astronomical Society* **496** (2020), 4087.

[150] P. Ocvirk, N. Gillet, P.R. Shapiro, D. Aubert, I.T. Iliev, R. Teyssier, G. Yepes, J.H. Choi, D. Sullivan, A. Knebe, S. Gottlöber, A. D'Aloisio, H. Park, Y. Hoffman und T. Stranex, *Monthly Notices of the Royal Astronomical Society* **463** (2016), 1462.

[151] P. Ocvirk, J.S. Lewis, N. Gillet, J. Chardin, D. Aubert, N. Deparis und E. Thélie, *Monthly Notices of the Royal Astronomical Society* **507** (2021), 6108.

[152] J.P. Paardekooper, S. Khochfar und C.D. Vecchia, *Monthly Notices of the Royal Astronomical Society* **451** (2015), 2544.

[153] R. Pakmor, A. Bauer und V. Springel, *Monthly Notices of the Royal Astronomical Society* **418** (2011), 1392.

[154] S. Parsa, J.S. Dunlop und R.J. McLure, *Monthly Notices of the Royal Astronomical Society* **474** (2018), 2904.

[155] A.H. Pawlik, A. Rahmati, J. Schaye, M. Jeon und C.D. Vecchia, *Monthly Notices of the Royal Astronomical Society* **466** (2017), 960.

[156] P.J.E. Peebles und J.T. Yu, *Astrophysical Journal* **162** (1970), 815.

[157] A.A. Penzias und R.W. Wilson, *Astrophysical Journal* **142** (1965), 419.

[158] H.B. Perets und L. Šubr, *Astrophysical Journal* **751** (2012), 133.

[159] A. Pillepich, D. Nelson, L. Hernquist, V. Springel, R. Pakmor, P. Torrey, R. Weinberger, S. Genel, J.P. Naiman, F. Marinacci und M. Vogelsberger, *Monthly Notices of the Royal Astronomical Society* **475** (2018), 648.

[160] A. Pillepich, D. Nelson, V. Springel, R. Pakmor, P. Torrey, R. Weinberger, M. Vogelsberger, F. Marinacci, S. Genel, A. van der Wel und L. Hernquist, *Monthly Notices of the Royal Astronomical Society* **490** (2019), 3196.

[161] A. Pillepich, V. Springel, D. Nelson, S. Genel, J. Naiman, R. Pakmor, L. Hernquist, P. Torrey, M. Vogelsberger, R. Weinberger und F. Marinacci, *Monthly Notices of the Royal Astronomical Society* **473** (2018), 4077.

[162] Planck Collaboration, *Astronomy and Astrophysics* **594** (2016), A1.

[163] W.H. Press und P. Schechter, *Astrophysical Journal* **187** (1974), 425.

[164] L.C. Price, H. Trac und R. Cen. *Reconstructing the redshift evolution of escaped ionizing flux from early galaxies with Planck and HST observations* (2016).

[165] E. Puchwein, F. Haardt, M.G. Haehnelt und P. Madau, *Monthly Notices of the Royal Astronomical Society* **485** (2019), 47.

[166] Y. Qin, S.J. Mutch, G.B. Poole, C. Liu, P.W. Angel, A.R. Duffy, P.M. Geil, A. Mesinger und J.S.B. Wyithe, *Monthly Notices of the Royal Astronomical Society* **472** (2017), 2009.

[167] M. Raičević, T. Theuns und C. Lacey, *Monthly Notices of the Royal Astronomical Society* **410** (2011), 775.

[168] A.O. Razoumov und J. Sommer-Larsen, *Astrophysical Journal* **710** (2010), 1239.

[169] A. Rémy-Ruyer, S.C. Madden, F. Galliano, M. Galametz, T.T. Takeuchi, R.S. Asano, S. Zhukovska, V. Lebouteiller, D. Cormier, A. Jones, M. Bocchio, M. Baes, G.J. Bendo, M. Boquien, A. Boselli, I. Delooze, V. Doublier-Pritchard, T. Hughes, O. Karczewski und L. Spinoglio, *Astronomy and Astrophysics* **563** (2014).

[170] J. Richard, R. Pelló, D. Schaerer, J.F. Le Borgne und J.P. Kneib, *Astronomy and Astrophysics* **456** (2006), 861.

[171] M. Ricotti und N.Y. Gnedin, *The Astrophysical Journal* **629** (2005), 259.

[172] M. Ricotti und J.M. Shull, *Astrophysical Journal* **542** (2000), 548.

[173] A.G. Riess, A.V. Filippenko, P. Challis, A. Clocchiatti, A. Diercks, P.M. Garnavich, R.L. Gilliland, C.J. Hogan, S. Jha, R.P. Kirshner, B. Leibundgut, M.M. Phillips, D. Reiss, B.P. Schmidt, R.A. Schommer, R.C. Smith, J. Spyromilio, C. Stubbs, N.B. Suntzeff und J. Tonry, *Astronomical Journal* **116** (1998), 1009.

[174] B.E. Robertson, S.R. Furlanetto, E. Schneider, S. Charlot, R.S. Ellis, D.P. Stark, R.J. McLure, J.S. Dunlop, A. Koekemoer, M.A. Schenker, M. Ouchi, Y. Ono, E. Curtis-Lake, A.B. Rogers, R.A. Bowler und M. Cirasuolo, *Astrophysical Journal* **768** (2013).

[175] J. Rosdahl, J. Blaizot, D. Aubert, T. Stranex und R. Teyssier, *Monthly Notices of the Royal Astronomical Society* **436** (2013), 2188.

[176] J. Rosdahl, J. Blaizot, H. Katz, T. Kimm, T. Garel, M. Haehnelt, L.C. Keating, S. Martin-Alvarez, L. Michel-Dansac und P. Ocvirk. *LyC escape from SPHINX galaxies in the Epoch of Reionization*, 2022.

[177] J. Rosdahl, H. Katz, J. Blaizot, T. Kimm, L. Michel-Dansac, T. Garel, M. Haehnelt, P. Ocvirk und R. Teyssier, *Monthly Notices of the Royal Astronomical Society* **479** (2018), 994.

[178] A.D. Sakharov, *Soviet Journal of Experimental and Theoretical Physics Letters* **5** (1967), 24.

[179] E.E. Salpeter, *Astrophysical Journal* **121** (1955), 161.

[180] M.G. Santos, L. Ferramacho, M.B. Silva, A. Amblard und A. Cooray, *Monthly Notices of the Royal Astronomical Society* **406** (2010), 2421.

[181] M. Sharma, T. Theuns, C. Frenk, R. Bower, R. Crain, M. Schaller und J. Schaye, *Monthly Notices of the Royal Astronomical Society: Letters* **458** (2016), L94.

[182] R.K. Sheth, H.J. Mo und G. Tormen, *Monthly Notices of the Royal Astronomical Society* **323** (2001), 1.

[183] B. Siana, H.I. Teplitz, J. Colbert, H.C. Ferguson, M. Dickinson, T.M. Brown, C.J. Conselice, D.F. de Mello, J.P. Gardner, M. Giavalisco und F. Menanteau, *The Astrophysical Journal* **668** (2007), 62.

[184] M. Sipp, P. LaChance, R. Croft, Y. Ni und T. Di Matteo, *arXiv e-prints* (2022), arXiv:2210.12907.

[185] A. Smith, R. Kannan, E. Garaldi, M. Vogelsberger, R. Pakmor, V. Springel und L. Hernquist, *Monthly Notices of the Royal Astronomical Society* **512** (2022), 3243.

[186] G.F. Smoot, C.L. Bennett, A. Kogut, E.L. Wright, J. Aymon, N.W. Boggess, E.S. Cheng, G. de Amici, S. Gulkis, M.G. Hauser, G. Hinshaw, P.D. Jackson, M. Janssen, E. Kaita, T. Kelsall, P. Keegstra, C. Lineweaver, K. Loewenstein, P. Lubin, J. Mather, S.S. Meyer, S.H. Moseley, T. Murdock, L. Rokke, R.F. Silverberg, L. Tenorio, R. Weiss und D.T. Wilkinson, *Astrophysical Journal, Letters* **396** (1992), L1.

[187] D.N. Spergel, L. Verde, H.V. Peiris, E. Komatsu, M.R. Nolta, C.L. Bennett, M. Halpern, G. Hinshaw, N. Jarosik, A. Kogut, M. Limon, S.S. Meyer, L. Page, G.S. Tucker, J.L. Weiland, E. Wollack und E.L. Wright, *Astrophysical Journal, Supplement* **148** (2003), 175.

[188] V. Springel, *Monthly Notices of the Royal Astronomical Society* **364** (2005), 1105.

[189] V. Springel, *Monthly Notices of the Royal Astronomical Society* **401** (2010), 791.

[190] V. Springel und L. Hernquist, *Monthly Notices of the Royal Astronomical Society* **339** (2003), 289.

[191] V. Springel, R. Pakmor, A. Pillepich, R. Weinberger, D. Nelson, L. Hernquist, M. Vogelsberger, S. Genel, P. Torrey, F. Marinacci und J. Naiman, *Monthly Notices of the Royal Astronomical Society* **475** (2018), 676.

[192] V. Springel, S.D. White, A. Jenkins, C.S. Frenk, N. Yoshida, L. Gao, J. Navarro, R. Thacker, D. Croton, J. Helly et al. , *nature* **435** (2005), 629.

[193] V. Springel, S.D. White, G. Tormen und G. Kauffmann, *Monthly Notices of the Royal Astronomical Society* **328** (2001), 726.

[194] E. Stanway und J. Eldridge, *Monthly Notices of the Royal Astronomical Society* **479** (2018), 75.

[195] D.P. Stark, R.S. Ellis, J. Richard, J. Kneib, G.P. Smith und M.R. Santos, *The Astrophysical Journal* **663** (2007), 10.

[196] R.A. Sunyaev und Y.B. Zeldovich, *Astrophysics and Space Science* **7** (1970), 3.

[197] T.M. Tauris und E.P.J. van den Heuvel. In *Compact stellar X-ray sources*, Band 39 (2006), Seiten 623–665.

[198] R. Teyssier, *Astronomy and Astrophysics* **385** (2002), 337.

[199] R.M. Thomas, S. Zaroubi, B. Ciardi, A.H. Pawlik, P. Labropoulos, V. Jelić, G. Bernardi, M.A. Brentjens, A.G. de Bruyn, G.J.A. Harker, L.V.E. Koopmans, G. Mellema, V.N. Pandey, J. Schaye und S. Yatawatta, *Monthly Notices of the Royal Astronomical Society* **393** (2009), 32.

[200] M. Trebitsch, M. Volonteri und Y. Dubois, *Monthly Notices of the Royal Astronomical Society* **494** (2020), 3453.

[201] M. Trebitsch, M. Volonteri, Y. Dubois und P. Madau, *Monthly Notices of the Royal Astronomical Society* **478** (2018), 5607.

[202] E. Vanzella, M. Nonino, G. Cupani, M. Castellano, E. Sani, M. Mignoli, F. Calura, M. Meneghetti, R. Gilli, A. Comastri, A. Mercurio, G.B. Caminha, K. Caputi, P. Rosati, C. Grillo, S. Cristiani, I. Balestra, A. Fontana und M. Giavalisco, *Monthly Notices of the Royal Astronomical Society: Letters* **476** (2018), L15.

[203] C.D. Vecchia, S. Khochfar und J. Schaye, *Proceedings of the International Astronomical Union* **8** (2012), 17–20.

[204] F. Villaescusa-Navarro, C. Hahn, E. Massara, A. Banerjee, A.M. Delgado, D.K. Ramanah, T. Charnock, E. Giusarma, Y. Li, E. Allys, A. Brochard, C. Uhlemann, C.T. Chiang, S. He, A. Pisani, A. Obuljen, Y. Feng, E. Castorina, G. Contardo, C.D. Kreisch, A. Nicola, J. Alsing, R. Scoccimarro, L. Verde, M. Viel, S. Ho, S. Mallat, B. Wandelt und D.N. Spergel, *Astrophysical Journal, Supplement* **250** (2020), 2.

[205] E. Visbal, G.L. Bryan und Z. Haiman, *The Astrophysical Journal* **897** (2020), 95.

[206] Z. Wang, J. Chen und S.C.H. Hoi, *arXiv e-prints* (2019), arXiv:1902.06068.

[207] R. Weinberger, V. Springel, L. Hernquist, A. Pillepich, F. Marinacci, R. Pakmor, D. Nelson, S. Genel, M. Vogelsberger, J. Naiman und P. Torrey, *Monthly Notices of the Royal Astronomical Society* **465** (2017), 3291.

[208] J.C. Weingartner und B.T. Draine, *The Astrophysical Journal* **548** (2001), 296.

[209] M. Werhahn, Y. Xie, M. Chu und N. Thuerey, *arXiv e-prints* (2019), arXiv:1906.01689.

[210] J.H. Wise und T. Abel, *Monthly Notices of the Royal Astronomical Society* **414** (2011), 3458.

[211] J.H. Wise, T. Abel, M.J. Turk, M.L. Norman und B.D. Smith, *Monthly Notices of the Royal Astronomical Society* **427** (2012), 311.

[212] J.H. Wise, V.G. Demchenko, M.T. Halicek, M.L. Norman, M.J. Turk, T. Abel und B.D. Smith, *Monthly Notices of the Royal Astronomical Society* **442** (2014), 2560.

[213] K. Wood und A. Loeb, *Astrophysical Journal* **545** (2000), 86.

[214] Y. Xie, E. Franz, M. Chu und N. Thuerey, *arXiv e-prints* (2018), arXiv:1801.09710.

[215] H. Xu, J.H. Wise, M.L. Norman, K. Ahn und B.W. O'Shea, *The Astrophysical Journal* **833** (2016), 84.

[216] X. Xu, A. Henry, T. Heckman, J. Chisholm, G. Worseck, M. Gronke, A. Jaskot, S.R. McCandliss, S.R. Flury, M. Giavalisco, Z. Ji, R.O. Amorín, D.A. Berg, S. Borthakur, N. Bouche, C. Carr, D.K. Erb, H. Ferguson, T. Garel, M. Hayes, K. Makan, R. Marques-Chaves, M. Rutkowski, G. Östlin, M. Rafelski, A. Saldana-Lopez, C. Scarlata, D. Schaerer, M. Trebitsch, C. Tremonti, A. Verhamme und B. Wang. *Tracing Lyman-alpha and Lyman Continuum Escape in Galaxies with Mg II Emission*, 2022.

[217] H. Yajima, M. Umemura, M. Mori und T. Nakamoto, *Monthly Notices of the Royal Astronomical Society* **398** (2009), 715.

[218] J.Y.C. Yeh, A. Smith, R. Kannan, E. Garaldi, M. Vogelsberger, J. Borrow, R. Pakmor, V. Springel und L. Hernquist, *arXiv e-prints* (2022), arXiv:2205.02238.

[219] T. Yoo, T. Kimm und J. Rosdahl, *arXiv:2001.05508 [astro-ph]* (2020).

[220] L. Yue, H. Shen, J. Li, Q. Yuan, H. Zhang und L. Zhang, *Signal Processing* **128** (2016), 389.

[221] F. Zwicky, *Astrophysical Journal* **86** (1937), 217.

Acknowledgements

Firstly, I would like to express my heartfelt gratitude to my supervisors Benedetta Ciardi and Torsten Enßlin for their unwavering support and exceptional guidance throughout my PhD journey. Without their valuable insights and mentorship, I would not have been able to overcome the challenges that came my way.

I am also deeply appreciative of my collaborators Dylan Nelson, Andrea Ferrara and Annalisa Pillepich, whose invaluable contributions, insightful discussions, and constructive criticism have been instrumental in shaping my research.

I would like to extend my sincere thanks to Enrico and Aniket for their stimulating conversations on reionization during group meetings and over Friday night beers.

My stay at the institute was made all the more enjoyable by the wonderful friends I made. Special thanks to Miha, who not only provided me with assistance on software but also enriched my life with fun discussions on physics and the stock market over WAW beers and bike rides. I am grateful to Vlas, Linda, Michael, Chris and especially Matteo for sharing many memorable moments with me, including hikes, bike trips, board games, and get-togethers that made my time in Munich unforgettable. I am also indebted to Lilya for our mutual encouragement to practice and run the Munich marathon, and to Simon, Hitesh, Geza, and all the others for the enjoyable MPA board game nights.

Finally, I am immensely grateful for the unwavering love and support of my family. My father Andriy, who engaged me in discussions about science and the world, and strongly encouraged me to publish my work. My mother Olga, who has always been there for me. My brother Vitaliy and sister Olesya, who shared many happy moments with me. Lastly, I extend my thanks to my grandma, aunts, and cousins for the many cherished memories we have shared, despite the dark times our homeland is facing.